

University of Alberta

**Metal-enrichment in microbial carbonates: the role of carboxylated
biomacromolecules**

by

Daniel Alejandro Petrash

A thesis submitted to the Faculty of Graduate Studies and Research
in partial fulfillment of the requirements for the degree of

Master of Sciences

Department of Earth and Atmospheric Sciences

©Daniel A. Petrash
Fall 2010
Edmonton, Alberta

Permission is hereby granted to the University of Alberta Libraries to reproduce single copies of this thesis and to lend or sell such copies for private, scholarly or scientific research purposes only. Where the thesis is converted to, or otherwise made available in digital form, the University of Alberta will advise potential users of the thesis of these terms.

The author reserves all other publication and other rights in association with the copyright in the thesis and, except as herein before provided, neither the thesis nor any substantial portion thereof may be printed or otherwise reproduced in any material form whatsoever without the author's prior written permission.

Examining Committee

Kurt O. Konhauser, Earth and Atmospheric Sciences

Murray K. Gingras, Earth and Atmospheric Sciences

Brian Lanoil, Biological Sciences

DEDICATION

I dedicate this work to my mother

ABSTRACT

Carboxylated macromolecules such as alginate and glycoproteins are abundant components of modern shallow marine sediments where they are secreted by bacteria and marine infauna. Both organic compounds are proton and metal reactive; hence, they have the potential to facilitate metal sorption and biomineralization reactions. In this study, lab experiments were coupled to field-based sampling to assess the role that these compounds play in microbial mats, with particular emphasis on the hypersaline lagoons of Los Roques, Venezuela.

Here I applied a surface complexation approach to model proton and Cd adsorption behaviour of both uronic acid-rich alginate and mucin. Measured total site concentrations, available for metal adsorption, demonstrate that these compounds have the potential to induce metal partitioning in early diagenetic microenvironments. Field results from Venezuela are consistent with Mg- and trace metal- enrichment that follows a likely correlation with the degradation states of microbial biomass trapped during accretion of modern microbialites.

ACKNOWLEDGEMENTS

On both a professional and a personal level I sincerely thank my supervisor Dr. Kurt Konhauser for his guidance, support and friendship. I am very appreciative of Dr. Murray Gingras for his significant contribution and support to my research. My gratitude also extends to Dr. Karlis Muehlenbachs for providing key support during the analytical stage of this work.

Thanks to all fellow students and friends from the Geomicrobiology Research Group, especially to Stefan Lalonde who read initial, rough (very rough at times!) drafts of some of the chapters before finalization, and always offered me his help and willingness to review and improve the quality of this manuscript.

I am very grateful to my mother for her inspiration and continued support of all my endeavours. Finally, I would like to sincerely thank my beloved Gabriela Gonzalez for her *epistemological solutions* and for her invaluable scientific assistance and encouragement.

Financial support was provided by NSERC grants awarded to Dr. K.O. Konhauser and Dr. M.K. Gingras.

TABLE OF CONTENTS

CHAPTER I

Introduction.....	1
1.1 Preamble	1
1.2 Exopolymers (EPS) in marine aquatic environments	5
1.2.1. Primary composition and functions.....	5
1.2.2. Degradation of EPS in marine environments.....	7
1.3 Purpose of research	7
1.3.1 Specific objectives.....	9
1.3.2 Structure of the study	9
1.4. References.....	14

CHAPTER II

Assessing the importance of organic matrix materials in biofilm chemical reactivity: proton and cadmium adsorption onto purified alginate..... 19

2.1. Introduction.....	19
2.2. Material and methods.....	21
2.2.1. Materials and Preparation.....	21
2.2.2. Potentiometric Titrations.....	21
2.2.3. Cadmium adsorption	22
2.2.4. Surface Complexation Modelling	23
2.2.5. FTIR	24
2.3. Results and discussion	24
2.3.1. Characterization of functional group identities and proton reactivity.....	24
2.3.2. Cd adsorption by alginate.....	26
2.4. Conclusions	28
2.5. References.....	35

CHAPTER III

Assessing the importance of organic matrices: mucin glycoproteins..... 39

3.1 Introduction.....	39
3.2 Methods.....	40
3.2.1. FTIR spectra.....	40
3.2.2 Acid-base titration.....	41
3.2.3. Cadmium complexation	42

3.3 Results and Discussion	43
3.3.1. FTIR spectra.....	43
3.3.2 Potentiometric titrations	45
3.3.3. Cd adsorption	45
3.3.4. PGM as an analog in bioturbation studies.....	46
3.4. Conclusions.....	48
3.5. References.....	54
CHAPTER IV	
Controls on accretion of modern gypsum microbialites	57
4.1. Introduction.....	57
4.2 Geological context	60
4.2.1. Archipiélago Los Roques National Park, Venezuela.....	60
4.2.2. Laguna Pirata.....	61
4.3 Methods.....	62
4.3.1. Collection of microbialites specimens and in situ analysis.....	62
4.3.2. Aqueous geochemistry	63
4.3.3 Petrological and geochemical analysis.....	64
4.4 Results.....	67
4.4.1 Lagoon water chemistry	67
4.4.2 Geobiology of the microbial mats.....	68
4.4.3 Biofilm mineral relationships.....	70
4.4.4 Mesostructural features	72
4.4.5 Microtextural and mineralogical features	73
4.4.6 Carbon and oxygen stable isotopes composition	75
4.4.7 Trace elements composition of carbonate cements.....	78
4.5 Discussion.....	79
4.5.1 Microbial involvement (?) in gypsum accumulation	79
4.5.2 Microbially-mediated replacement of gypsum	81
4.5.3. Mg and $\delta^{13}\text{C}$ enrichment in cements	84
4.5.4 Distribution of trace metals.....	84
4.5.5 The role of polysaccharides in stabilization (cementation).....	84
4.5.6 Implications for the Precambrian	86
4.6 Conclusions.....	87
4.7 References.....	115

CHAPTER V	
Summary and conclusions.....	125
5.1 To the experimental component.....	126
5.2 To the field component	126

LIST OF TABLES

Table 1-1. Composition of EPS and range of component concentrations.....	12
Table 1-2 Composition of EPS from agar-grown biofilm of <i>Pseudomonas aeruginosa</i>	13
Table 2-1. Best-fit model parameters for alginate titration data.	29
Table 2-2 Best-fit log Cd-carboxyl stability constants for metal adsorption experiments	30
Table 2-3. pK _a values attributed to carboxyl functional groups and log Cd-carboxyl.....	31
Table 3-1. Absorption frequencies and interpreted compounds on mucin and comparison with Terebellid mucous	49
Table 3. 2. Titration data modeling, acidity constants and site concentrations.	50
Table 4-1. Chemical features of the lagoon water.	93
Table 4-2. Stable C and O isotopes values (V-PDB) and Mg oxide content (weight %) from Los Roques microbialites.	94
Table 4-3. Comparison of the cements and mat authigenic carbonates trace concentrations.....	95

LIST OF FIGURES

Figure 2-1. FTIR spectra (% transmittance) of alginic acid sodium salt.	32
Figure 2-2. Potentiometric titration data for three titrations of alginate in 0.01M NaNO ₃	33
Figure 2-3. Cd sorption data (Alginite).....	34
Figure 3-1. FTIR spectra of PGM vs Terebellid worms mucus secretions.....	51
Figure 3-2. Potentiometric titration data for three titrations of mucin in 0.1 M NaNO ₃	52
Figure 3-3 Average best-fit discrete site model obtained by least squares optimization of titration data as implemented in FITEQL 4.0.....	53
Figure 3-4. Cd sorption data (PGM).	54
Figure 4-1. Location of the study area.	95
Figure 4-2. Schematic hydrological model of Laguna Pirata.....	96
Figure 4-3. General macroscopic features of the microbial influenced sedimentation in Pirata lagoon	97
Figure 4-4. Macroscopic and microsensing data from the bacterial mat associated with accreting thrombolitic structures	98
Figure 4-5 Logarithmic plot showing the enrichment/ depletion factors of certain trace elements in Laguna Pirata surface water	99
Figure 4-6. Delicate microbial features from the biofilm associated to Laguna Pirata's microbialites.....	100
Figure 4-7. TEM images showing the ultrastructure of microbes observed in Laguna Pirata's mats	101
Figure 4-8. Microtextural features in sediments from the thrombolite-constructing mat.	103
Figure 4-9. Cryo-SEM showing authigenic carbonate held by the photosynthetic mat	104
Figure 4-10. Biological SEM of the mat supporting gypsum crystals.....	105
Figure 4-11. Replacement of gypsum by carbonates	107

Figure 4-12. BSE and X-ray map of the basal part of the specimen.....	109
Figure 4-13. BSE and X-ray map of the different zones of the thrombolite specimen.....	110
Figure 4-14. Carbon and oxygen stable isotopes and major element distribution in one of the specimens collected.....	111
Figure 4-15. Logarithmic plot showing relevant metal-enrichment/depletion trends between carbonates phases under examination.	112
Figure 4-16. Summary of relevant vertical enrichment trends within the specimen under examination.....	113
Figure 4-17. Paragenetic diagram and relevant metabolic pathways determining mineral associations within thrombolites.....	114

LIST OF ABBREVIATIONS

ACC: Amorphous Calcium Carbonate

BSR: Bacterial Sulfate Reduction

BSO: Bacterial Sulfide Oxidation

EPS: Exopolymeric substances; also Extracellular Polymeric Substances

HMC: High-Magnesium Calcite

ICP-MS: Inductively Coupled Mass Spectrometry

LMC: Low-Magnesium Calcite

PGM: Type III- Porcine Gastric Mucin

SCM: Surface Complexation Model

SEM: Scanning Electron Microscopy

SOB: Sulfide-Oxidizing Bacteria

SRB: Sulfate-Reducing Bacteria

TEM: Transmission Electron Microscopy

CHAPTER I

Introduction

1.1 Preamble

Bacterial biofilms are heterogeneous systems consisting of bacterial cells embedded in a gel-like matrix of extracellular polymeric substances (EPS), salts and water (Körstgens et al, 2001). EPS in general are comprised of high molecular weight organic compounds (polysaccharides, lipids and proteins; Table 1-1), which contain ionisable functional groups such as carboxyl, phosphoryl, amino, thiol and hydroxyl groups that enable EPS to sequester metals (Beveridge, 1980; Konhauser, 2007). Carboxylic acids comprise most of the ionisable reactive sites in the exopolymers secreted by algae, gram-positive microbes grown with phosphate limitation, and some gram-negative microbial polysaccharides (Fazio et al., 1982). At the pH conditions prevailing in a typical marine environment, carboxylic acids will always remain deprotonated, making them efficient metal-binding sites (Visscher et al., 1998). On the contrary, thiol and amino groups, with pK_a values ranging from 7.0 to 9.0, will be subject to periodic changes in protonation states, and thus these functional groups will not always be able to bind metals in a typical marine diagenetic setting (Visscher et al., 1998).

Microbial mats are thick biofilms comprised mostly of EPS, authigenic and trapped minerals, and microbial cells (Konhauser, 2007). They are small-scale ecosystems which harbour flexible benthic communities of microorganisms, usually dominated by phototrophic bacteria (Jørgensen et al., 1983), which arrange themselves as vertically stratified communities in response to steep vertical gradients of light intensity and redox conditions that change markedly during the diel cycle (Des Marais, 2003). This stratification causes gradients of oxygen and sulfide maintained by the metabolic activities of the microbes comprising the mat (van Gemerden, 1993), shaping the chemical environment and providing diel-cycling microenvironments that are separated on a scale of a few millimetres (Revsbech et al., 1983). Microbial mats can be found in a variety of different habitats, ranging from marine intertidal flats, hypersaline and alkaline environments, to hot springs, dry temperate deserts, and the cold dry environment of Antarctica (Stal, 2000). Many of these habitats, often referred to as extreme environments, are characterized by highly selective conditions which exclude most if not all competing organism and grazers.

Mg carbonates, ranging from high-Mg calcites (HMC, $\text{MgCO}_3 > 4$ mol percent) to penecontemporaneous dolomite ($\text{MgCO}_3 \sim 48$ mol percent), form in association with microbial mats in hypersaline shallow marine environments (Vasconcelos and McKenzie, 1997; Wright, 1999; Bontognali, et al., 2010) Although microbial EPS has been regarded as a facilitator of the early diagenetic reaction leading to Mg carbonates, the mechanisms responsible are poorly understood. Crystallization experiments using carboxyl rich compounds are known to produce calcite with as most 15 mol% MgCO_3 (Raz et al., 2000), however the partial degradation of carboxyl- rich EPS matrices seems to be a prerequisite for higher Mg contents in microbial carbonates (Weber, 1970; Raz et al., 2000; Weiner et al., 2003). Preferential binding of divalent metals by EPS may be a key factor. The high carboxyl content of EPS, often in the form of alginate-like biopolymers (Körstgens et al, 2001), makes EPS an efficient template for the precipitation of Mg carbonates, usually as amorphous carbonate phases (ACC) (Kawagushi and Decho 2002; Wang et al, 2009). However, several kinetic and physicochemical constraints hamper the formation of HMC in modern marine environments, and more crystalline carbonate polymorphs, such as calcite or aragonite, often replace the ACC intermediate early during diagenesis (Raz et al., 2000) .

Therefore, with a few exceptions, microbial carbonates and microbial carbonate sedimentary features such as microbialites (Burne and Moore, 1987), stromatolites (Andres et al., 2006), thrombolites (Kennard and James, 1986), and beachrocks (Neumeier, 1999), have a mole fractions of MgCO_3 that rarely exceed 15 mole percent (cf. Bricker, 1971).

For stabilization and subsequent growth of amorphous carbonate precursors as Mg-rich crystalline carbonates a number of kinetic factors must be overcome. The process is thought to be ruled by three intimately-related aspects of carbonate chemistry which control crystal growth:

1. The high enthalpy of hydration of Mg^{2+} (Lippmann, 1973), which limit its availability for mineral nucleation reactions. Mg ions only partially dehydrate when approaching a growing nucleus; once the partially dehydrated magnesium ions attach to the surface of the critical nucleus (Sibley et al., 1994), the strongly bound residual hydration sphere inhibits further surface precipitates from forming HMCs (Lippmann, 1973, Folk, 1974; Berner, 1975). Magnesium also forms complexes with sulfate, and with Cl^- in brines (Machel and Mountjoy, 1986), further limiting the amount of free Mg ions available in natural waters.
2. Relatively low alkalinity or low concentrations of dissolved CO_3^{2-} relative to HCO_3^- prevent Mg incorporation into growing carbonate crystals (Wright, 1999). Under such conditions there is insufficient free energy for available CO_3^{2-} to overcome Mg^{2+} hydration energy barriers at the surfaces of growing crystallites (Lippmann, 1973; Machel and Mountjoy, 1986).
3. The presence of dissolved $[\text{SO}_4^{2-}]$, which is thought to be an inhibitor of the dolomitization reaction of pre-existing carbonate phases (Baker and Kastner, 1981; Kastner, 1984) (But see Hardie, 1987; Brady et al., 1996 for discussion).

Although much of the recent literature has focused on the role of sulfate reduction (e.g., Vasconcelos and McKenzie, 1997) and sulfide oxidation (e.g., Moreira et al., 2004) in promoting supersaturated conditions for dolomite and HMC to precipitate, little attention has been directed to their role in the degradation of EPS and production of organic templates promoting mineral nucleation (e.g., Kwak et al., 2005). This is important because calcium and magnesium behaviour (i.e., mobility, bioavailability) in natural pore water systems depends on the distribution and nature of their association with carboxylated

ligands (Sutherland, 2001) and the selectivity of Ca^{2+} , and other cations, binding to bacterial EPS (Geddie and Sutherland, 1994; Lee et al, 1996) may have an impact on the concentration of other metal ions in the aquatic system. For instance, bacterial alginates, present in many marine EPS (Table 1-2), show cation selectivity (for Ca^{2+} in particular) in the formation of cation-stabilized cross-linkages and bridges (Decho, 1999; Davies et al., 2003); the affinity of EPS for binding Ca ions is thought to initially inhibit carbonate precipitation within EPS matrices (Decho et al., 2005), but in areas where concentrations of Ca and Mg ions have been increased in association to heterotrophy of organic matter these ions may co-precipitate as Mg-calcite (Arp et al., 1999; Dupraz and Visscher, 2005; Decho et al., 2005).

The small number of experiments leading to synthetic dolomite under near-surface conditions have consistently shown that precipitation occur as aggregates of crystallites (50–100 nm) embedded in zones of a EPS network partially degraded by heterotrophic bacteria (Vasconcelos and McKenzie, 1997; van Lith et al 2003; Benzerara et al., 2006; Sánchez-Román et al., 2009). To explain this recurring observation, it has been proposed that decaying EPS transforms into a highly organized template structure favouring the co-precipitation of calcium and magnesium (Raz et al., 2000; Jin-Han and Aizenberg, 2003; Kwak et al., 2005; Wang et al., 2009). Nonetheless, the molecular process linked to the stabilization of ACC as high-Mg calcites (HMC) remains elusive.

Because differences in the order of affinity of metallic ions towards EPS depends on the variability of molecular weights, composition, and degradation states of primary EPS compounds (Decho et al, 2005), new work examining divalent metal mobility in microbially-influenced pore water and sediment systems is needed in order to provide new insight into minor and trace element incorporation into carbonate cements. However, many parameters that control chemical equilibrium in natural microbial carbonate-forming systems cannot be easily reproduced or accurately quantified in the lab, mostly due to difficulties associated with isolating EPS compounds from their inorganic constituents without effecting EPS properties (Comte et al., 2006). Detailed sedimentological and chemostratigraphic analysis of modern microbialites, coupled with laboratory experiments employing simple organic compounds as EPS analogs, may offer some insight into processes of cation selection and Mg carbonate cementation in microbial carbonates.

1.2 Extracellular Polymeric Substances (EPS) in marine aquatic environments

In this next section, I briefly consider the major properties that render EPS reactive towards metals in solution, and the potential for bacteria to control the incorporation of metals into authigenic carbonate cements through a selective degradation of EPS matrices. I will not attempt to cover this large topic in a detailed treatment and those wishing to pursue the topic further are referred to Konhauser (2007, and references therein).

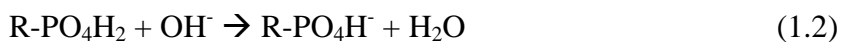
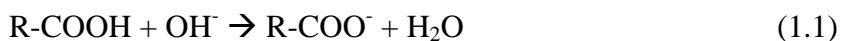
1.2.1. Primary composition and functions

1.2.1.1 Their polyelectrolyte nature

Despite being built up from very similar building blocks (the carbohydrate ring structure), polysaccharides in EPS often have diverse structural and functional properties. The specific composition of EPS, and therefore its acidic moieties, is taxonomically and environmentally regulated (Perry et al., 2005). It can vary (Table 1-1) depending on the microorganism, their growth stage, and various environmental stimuli such as nutrient abundance, toxicity of metal ions in solution or periodic desiccation (Decho 1990; Bergamaschi et al., 1999; Perry et al., 2005). However, as shown in Table 1-2, compositional constraints from *Pseudomonas aeruginosa*, a model organism with which many biofilm investigations have been carried out (Flemming and Wingender, 2001), demonstrate that alginate-like polymers can be considered one of the main compounds comprising EPS (e.g., Fazio et al., 1982; Conti 1994; Wingender et al., 2001).

In general, most microbial polysaccharides are either homopolysaccharides composed of a single sugar unit, or heteropolysaccharides, in which regular repeat units of 2–8 monosaccharides are formed. Bacterial polymers are mainly found to contain polysaccharides and glycoproteins together with uronic acids of which D-glucuronic acid is most common (Fazio et al., 1982; Flemming and Wingender, 2001; Sutherland, 2001; Guibaud et al., 2008). The polysaccharides may be either neutral or polyanionic, and as previously discussed, the later owe most of their charge under natural marine conditions to carboxyl-rich moieties such as uronic acid (Flemming and Wingender, 2001). Polysaccharides and other organic compounds in EPS contain functional groups that release protons (H^+) into solution over the pH range of marine pore waters. For instance, numerous studies with microbial biomass have demonstrated that carboxyl groups account for the pH

buffering capacity of biomass from pH 2-6 (reaction 1.1), phosphate groups from pH 5-8 (reaction 1. 2), amino groups at pH >8 (reaction 1.3), while thiol and hydroxyl groups deprotonate at pH values above 10 (reaction 1.4 and 1.5, respectively) (see Konhauser, 2007 for details).



The ionization potential of functional groups provides an electrical charge which facilitates chemical reactions with dissolved ions, and ultimately, the sorption of metal cations to organic compounds in natural and contaminated environments (see Konhauser et al, 2007, for details).

1.2.1.1 Functions

EPS networks provide a number of benefits to the biofilm, including protection from UV irradiation, desiccation, and buffering from extremes in environmental conditions. EPS additionally serve as the interface between the microbes themselves and their external milieu, where essential metals can be adsorbed in close proximity to the cells, while toxic metals are prevented from directly interacting with the cell proper (see Konhauser 2007 for a comprehensive review). EPS are mainly responsible for the structural and functional integrity of biofilms and are considered key components that determine the physicochemical properties of biofilms (Flemming and Wingender, 2001). In marine sediments, microbially-derived uronic acids and their monomers interact with other organic components and metal ions in solution, driving a variety of processes, such as humic acid production, detoxification of toxic chemicals, removal of metal ions, production of macroaggregates (i.e. peloids) and adsorption of dissolved metals in the cationic form in seawater (Chave and Suess, 1970; Decho 1990; Frye and Thomas 1993; Khodse et al., 2008).

The adhesive properties of uronic acid-rich EPS are believed to play a critical role in initial phases of colonization and microbial adhesion (Mopper et al., 1995; Leppard, 1997; D'Souza et al., 2003) and are important in sediment stabilization (Braissant et al., 2009). In evaporative settings, the gelling properties of alginates (the generic name for heteropolymeric chains made of uronic acids) help in preventing dehydration of cells, and their abundance in EPS is a key factor regulating ionic diffusion in biofilms (Fazio et al., 1982). The polyelectrolyte nature of EPS constituents and their association with metabolically diverse microbial populations inhabiting biofilm systems facilitate a continuum of dissolution and precipitation reactions that are critical determinates of the fate of metals in marine environments (Konhauser 2007, and references therein).

1.2.2. Degradation of EPS in marine environments

In sediments EPS likely exists as a 'continuum' of compounds of different molecular weights, composition and degradation states (Braissant et al., 2009). Degradation of EPS consists of a multistep process of sequential degradation that leads to a mixture of components ranging from highly labile to relatively refractory (Braissant et al., 2009). The heteropolymeric fraction can be degraded by hydrolytic and fermentative processes to their monomeric units which can then be rapidly consumed as an energy source by microbial respiration (Decho, 1990; Khodse et al., 2008). The initial hydrolysis of EPS is rapid and possibly selective, with preferential respiration of uronic monomers by heterotrophs (Sutherland, 2001; Braissant et al., 2009); this process has the potential to affect the concentration of certain metals in the pore water system, creating zones within the gel-like matrix that are near-saturated or even over-saturated in bioactive metals such as Zn, Cd, Co, Ca, Cu, Mn, Ca, Mg, Fe and Ni, enabling minerals (mostly carbonates, but also iron hydroxides and sulfates) to precipitate if pH and Eh conditions are favourable (Konhauser, 2007; Braissant et al., 2009).

1.3 Purpose of research

Carboxylated polysaccharides are major components in the carbohydrate fraction of algae (Haug et al., 1974), fungi (Mowl and Gadd, 1984), bacterial EPS (Kennedy & Sutherland, 1987; Flemming and Wingender, 2001) and animal mucous (Bavington et al., 2004; Bansil and Turner, 2006). However, the specific contribution to metal binding from

carboxyl groups in these important compounds has yet to be studied in an experimental framework where their adsorption capacities can be quantified and compared with the many types of other reactive components comprising biofilm materials (*e.g.*, other functional groups, bacterial cell walls or other biomass, or authigenic minerals). This study aims to explore the role of carboxylated macromolecules in promoting the incorporation of divalent metals other than Ca into microbial carbonates.

The experimental part of this research is devoted to examining proton and Cd complexation behaviour of alginate and mucin glycoproteins, as such compounds may have strong control over the incorporation of divalent metals, including Mg, into authigenic carbonates growing in EPS matrices at shallow marine environments. These biomacromolecules are studied by using two commercially-available, and well characterized, products: (1) purified alginate, extracted from brown algae, as an analogue to alginate in natural EPS; and Type III porcine gastric mucin (PGM) as an analogue to mucin. Cd is used herein as a model divalent metal for the following reasons:

1. Cd remains soluble over the pH range of most marine environments, and unlike Ca and Mg, its use in laboratory settings is not complicated by carbonate complexation and precipitation.
2. To facilitate comparison with other adsorption studies involving fulvic/humic acids or bacteria that use Cd as a model divalent metal.
3. Its relevance to near-shore ocean and estuary waters, where Cd concentrations may be elevated.

In order to bridge the gap between the experimental studies and natural conditions promoting the incorporation of divalent metals into microbially-influenced carbonate sediments, the second part of this study focuses on fluxes of cations in sediment-pore waters of modern domal microbialites. Microbialites represent accumulations of minerals that grow as coincidental by-products of processes occurring within microbial mats (Kamber et al., 2004). The paragenetic history and textural relations of mineral within microbialites should reflect their accretionary history, and carbonates cements growing within a polysaccharide-rich organic matrix undergoing degradation should have geochemical signatures resulting from equilibration with the carbonate-oversaturated

microenvironments developed after selective degradation of heteropolymeric EPS compounds. In other words, within microbialites the metal affinities of the major compounds of EPS and their subsequent degradation can act to increase the availability of minor and trace metals in the pore waters that can therefore be incorporated into carbonate cements, if pH and Eh conditions are favourable. Such complex process, however, cannot be easily reproduced in the lab, but can be explored through a detailed mineralogical and geochemical investigation of modern subaqueous gypsum-rich microbialites. In this study, gypsum rich thrombolites growing in a hypersaline lagoon at the Archipelago Los Roques, Venezuela were studied with the aim of understanding their mechanisms of accretion and calcification, especially with regards to correlations between their trace element content and microbial metabolic zones favouring EPS production or degradation.

1.3.1 Specific objectives

This work explores the importance of carboxylated biomacromolecules in promoting the incorporation of metals into microbial carbonates in marine hypersaline environments. Accordingly, the aims of the present study are:

- 1) To evaluate the metal reactivity of two major biologically-produced carboxylated macromolecules present in shallow marine sediments: alginate, produced by a number of microbes comprising biofilms, and mucin glycoproteins, excreted by epithelial cells of marine meiofauna.
- 2) To evaluate the textures and biogeochemical signatures associated to the calcification of modern gypsum-dominated deposits growing in a polysaccharide-rich matrix undergoing microbial degradation.

1.3.2 Structure of this study

With the exception of the first and last chapters, each of the chapters are designed to be a self-contained research paper with results placed in the context provided by previous studies in that subject area. As previously discussed, of central importance is the extent to which carboxylated compounds determine the metal complexation behaviour of EPS, and

the role of natural EPS degradative processes that may influence the incorporation of metals into the crystal lattices of carbonates cements growing a microbially modified EPS matrix (e.g., Braissant et al., 2007). Accordingly, **Chapter II** examines the proton- and metal-reactivity of alginate, a common EPS glycoprotein commercially available in the form of a brown algae extract. Alginate is a straight-chain, polyuronic acid extensively secreted by algae and several species of bacteria, including *Pseudomonas sp.* and *Azotobacter sp.* (Sutherland 1995). All alginates, whether bacterial or algal, are composed by α -L-guluronate (G) and β -D-mannuronate (M) units linked through 1 \rightarrow 4 glycosidic bonds to form a biopolymer that occur as an irregular series of block structures (Dragget et al., 2005). The purified alginate extract is herein explored in order to obtain thermodynamic parameters describing its Cd adsorption behaviour and compare these parameters with those describing Cd adsorption to biofilm cultures, isolated EPS and bacterial cell walls, and humic/fulvic substances, ranging from alginate-dominated to alginate-free, in order to determine the role of alginates in determining the affinity of EPS for various divalent metals.

In the same line of the previous chapter, **Chapter III** evaluates the suitability of the commercially-available Type III Porcine Gastric Mucin (PGM) as an experimental surrogate for mucin glycoproteins. Mucin-type glycoproteins are secreted by diverse eukaryotic organisms present in marine modern environments, from protists (Guibaud et al, 2008) to more complex animals such as burrowing worms (Lalonde et al, 2010). Structurally, mucins are complex glycoconjugates that typically have a central tandem repeat domain composed of serine or threonine interspersed with cysteine-rich domains. Hundreds of O-glycosides are covalently attached to serine or threonine residues in the protein backbone (Bansil and Turner 2006). The availability of glycoproteins, in general, may be a factor influencing the accumulation of Mg and other divalent metals (Wang et al., 2009) and results from Chapter III permit a direct comparison between difficult-to-obtain natural mucins and readily-available PGM in terms of the quantity, acidity, and composition of metal-reactive organic ligands, and their affinity for dissolved metals such as Cd.

The flux of cations from surrounding waters into microbial cements is to some degree controlled by metabolic and adsorptive reactions promoted by the associated

microbial communities (Kamber et al., 2004). The degradation of EPS entrained during microbialite accretion (e.g., Klok et al, 1984), and its role in determining the composition of sediments, may be revealed through the chemical signatures of the associated carbonate cements. The essential elements of this working hypothesis, as explored in **Chapter IV**, are: (1) complexation within EPS matrices may greatly affect trace element uptake by associated microbial carbonates; (2) the previous mechanism regulates the metal content of the organic nucleation templates (e.g., heteropolysaccharides such as alginate) within the structure, and thereby may discriminate against ambient elemental ratios; (3) degradation of EPS trapped during accretion produce complex Eh and pH gradients within the structure, influencing internal diffusion pathways and cation fluxes towards active sites of mineralisation (e.g., Kamber et al, 2004). From this study of modern gypsum-rich microbialites, it is suggested that biosignatures, resulting from the degradation states of the microbial biomass trapped during accretion, might be preserved in ancient analogues.

Finally, **Chapter V** places results and major discussion points in a more general context in the form of a summary and concluding chapter that attempts to draw together the disparate lines of evidences presented into a working model that describes the timing and nature of metal enrichment in microbial carbonates, with the ultimate goal of identifying possible biosignatures, previously cryptic, in analogue Precambrian deposits.

Component	Content in EPS
Polysaccharides	40–95%
Protein	<1–60%
Nucleic acids	<1–10%
Lipids	<1–40%

Table 1-1. Composition of EPS and range of component concentration (After Flemming and Wingender, 2001).

Component	Maximum proportion found in EPS
Total carbohydrates	76.20%
Uronic acids (alginate)	85.00%
Proteins	45.50%

Table 1-2. Composition of EPS from agar-grown biofilm of *Pseudomonas aeruginosa*. Data related to 10^9 cells (after Wingender et al., 2001)

1.4. References

- Andres MS, Sumner DY, Reid RP, Swart PK. 2006. Isotopic fingerprints of microbial respiration in aragonite from Bahamian stromatolites. *Geology* 34:973-976.
- Arp G, Reimer A, Reitner J. 1999. Calcification in cyanobacterial biofilms of alkaline salt lakes. *European Journal of Phycology* 34:393-403.
- Bansil R, Turner B. 2006. Mucin structure, aggregation, physiological functions and biomedical applications. *Current Opinion in Colloid & Interface Science* 11:164-170.
- Baker PA, Kastner M. 1981. Constraints on the formation of sedimentary dolomite. *Science* 213: 214-216.
- Benzerara K, Menguy N, López-García P, Yoon T, Kazmierczak J, Tyliszczak T, Guyot F, Brown GE. 2006. Nanoscale detection of organic signatures in carbonate microbialites. *Proceedings of the National Academy of Sciences of the United States of America*, 103: 9440-5.
- Bavington CD, Lever R, Mulloy B, Grundy MM, Page CP, Richardson NV, McKenzie, JD. 2004. Anti-adhesive glycoproteins in echinoderm mucus secretions: *Comp. Biochem. Physiol. Bull.* 139:607–617.
- Berner RA. 1975. The role of magnesium in the crystal growth of calcite and aragonite from seawater. *Geochim. Cosmochim. Acta* 39:489-604.
- Bergamaschi B, Walters JS and Hedges JI. 1999. Distributions of uronic acids and O-methyl sugars in sinking and sedimentary particles in two coastal marine environments. *Geochim. Cosmochim. Acta* 63: 413–425.
- Bontognali TR, Vasconcelos C, Warthmann RJ, Dupraz C, Strohmenger CJ, McKenzie J.A. 2010. Dolomite formation within microbial mats in the costal sabkha of Abu Dhabi (UAE). *Sedimentary Geology* 57: 824-844
- Brady, P, Krumhansl J, Papenguth, H. 1996. Surface complexation clues to dolomite growth. *Geochim. Cosmochim. Acta* 60:727-731
- Braissant O, Decho AW, Przekop KM, Kimberley L, Gallagher G, Dupraz C, and Visscher PT. 2009. Characteristics and turnover of exopolymeric substances in a hypersaline microbial mat. *FEMS Microbiol. Ecol.* 67:293–307.
- Bricker DP. 1971. *Carbonate Cements*: Baltimore, Johns Hopkins University, *Studies in Geology* 19, 376 p.
- Burne RV, Moore LS. 1987, *Microbialites: Organosedimentary deposits of benthic microbial communities*. *PALAIOS* 2, 241–254.

- Chave KE, Suess KE. 1970. Calcium carbonate saturation in sea-water: effects of dissolved organic matter. *Limnol. Oceanogr.* 15: 633-637.
- Comte S, Guibaud G, Baudu M. 2006. Relations between extraction protocols for activated sludge extracellular polymeric substances (EPS) and complexation properties of Pb and Cd with EPS Part II. Consequences of EPS extraction methods on Pb²⁺ and Cd²⁺ complexation. *Enzyme and Microbial Technol* 38:246-252.
- Conti E, Flaibani, A, O'Regan M, Sutherland IW. 1994 Alginate from *Pseudomonas fluorescens* and *P. putida*: production and properties. *Microbiology*, 140:1125-1132.
- Davis TA, Volesky B, Mucci 2003. A review of biochemistry of heavy metal biosorption by brown algae. *Water Research* 37:4311-4330.
- Decho AW. 1990. Microbial exopolymer secretions in ocean environments: Their role(s) in food webs and marine processes. *Oceanogr. Mar. Biol. Ann. Rev.* 28:73-153.
- Decho AW. 1999. Imaging of an alginate polymer gel using atomic force microscopy. *Carbohydrate Research* 315: 330-333.
- Decho A, Visscher P, Reid R. 2005. Production and cycling of natural microbial exopolymers (EPS) within a marine stromatolite. *Palaeogeography, Palaeoclimatology, Palaeoecology* 219:71-86.
- Des Marais DJ. 2003. Biogeochemistry of hypersaline microbial mats illustrates the dynamics of modern microbial ecosystems and the early evolution of the biosphere. *The Biological Bulletin* 204: 160-167.
- Dragget KI, Smidsrød O, and Skjåk-Braek G. 2005. Alginates from algae. *In* Steinbüchel A., Rhee SK, editors. *Polysaccharides and Polyamides in the Food Industry: Properties, Production and Patents*. Wiley-VCH, Weinheim. P. 1-30.
- D'Souza F, Garg A, Bhosle NB. 2003. Biogeochemical characteristics of sedimenting particles in Dona Paula Bay, India. *Estuarine Coastal Shelf Science* 58:311-320.
- Fazio SA, Uhlinger DJ, Parker JH and White DC. 1982. Estimations of uronic acids as quantitative measures of extracellular and cell wall polysaccharide polymers from environmental samples. *Appl. Environ. Microbiol.* 43:1151-1159.
- Flemming HC and Wingender J. 2001 Relevance of microbial extracellular polymeric substances (EPS's): Part I. Structural and ecological aspects. *Water Sci. Technol.* 43:1-8.
- Frye G, Thomas M. 1993. Adsorption of organic compounds on carbonate minerals 2. Extraction of carboxylic acids from recent and ancient carbonates. *Chem. Geol.* 109:215-226.

- Folk RL. 1974. The natural history of crystalline calcium carbonate: effect of magnesium content and salinity. *J. Sediment Petrol.* 44:40-53.
- Guibaud G, Bordas F, Saaid A, D'abzac P, Van Hullebusch E. 2008. Effect of pH on cadmium and lead binding by extracellular polymeric substances (EPS) extracted from environmental bacterial strains. *Colloids and surfaces. B: Biointerfaces.* 63:48-54.
- Haug A, Larsen B, Smidsrød O. 1974 Uronic acid sequence in alginate from different sources. *Carbohydr. Res.* 32: 217–225.
- Jin-Han Y, Aizenberg J. 2003. Effect of Magnesium Ions on Oriented Growth of Calcite on Carboxylic Acid Functionalized Self-Assembled Monolayer. *J. Am. Chem. Soc.* 125:402-403.
- Jørgensen BB, Revsbech NP, Cohen Y. 1983. Photosynthesis and structure of benthic microbial mats: microelectrode and SEM studies of four cyanobacterial communities. *Limnol Oceanogr* 28: 1075-1093.
- Hardie LA. 1987. Dolomitization: a critical view of some current views. *J. Sediment Petrol.* 57:166-183.
- Kastner M. 1984. Control of dolomite formation. *Nature* 311, 410–411.
- Kennard JM, James NP. 1986. Thrombolites and Stromatolites, Two Distinct Types of Microbial Structures *PALAIOS* 1: 492-503.
- Kennedy AFD, Sutherland IW. 1987. Analysis of bacterial exopolysaccharides. *Biotechnol. Appl. Biochem.* 9:12-19.
- Khodse VB, Fernandes L, Gopalkrishna VV, Bhosle NB, Fernandes V, Matondkar SGP, Bhushan R. 2007. Distribution and seasonal variation of concentrations of particulate carbohydrates and uronic acids in the northern Indian Ocean. *Marine Chemistry* 103: 327–346.
- Klok J, Cox H, Baas M, Schuyl PJW, de Leeuw JW, Schenck PA. 1984. Carbohydrates in recent marine sediments. II. Occurrence and fate of carbohydrates in a recent stromatolitic deposit: Solar Lake, Sinai *Organic Geochemistry* 7:101-109.
- Konhauser KO. 2007. *Introduction to Geomicrobiology.* Blackwell Publishing. 433 p.
- Körstgens V, Flemming HC, Wingender J, Borchard W. Influence of calcium ions on the mechanical properties of a model biofilm of mucoid *Pseudomonas aeruginosa*. *Water Science and Technology* 43:49-57.
- Kwak S, DiMasi E, Han Y, Aizenberg J, Kuzmenko I. 2005. Orientation and Mg Incorporation of Calcite Grown on Functionalized Self-Assembled Monolayers: A Synchrotron X-ray Study. *Crystal Growth & Design* 5:2139-2145.

- Lalonde SV, Dafoe L, Pemberton SG, Gingras MK, Konhauser KO. 2010. Investigating the geochemical impact of burrowing animals: Proton and cadmium adsorption onto the mucus-lining of Terebellid polychaete worms. *Chemical Geology* 271:44-51
- Lee JW, Ashby RD, Day DF. 1996. Role of acetylation on metal induced precipitation of alginates. *Carbohydrate Polymers* 29: 337-345.
- Leppard GG. 1997. Colloidal organic fibrils of acid polysaccharides in surface waters: electron-optical characteristics, activities and chemical estimates of abundance. *Colloids and Surface A: Physicochemical Engineering Aspects* 120:1–15.
- Lippmann F. 1973. *Sedimentary carbonate minerals*: New York, Springer-Verlag, 228 p.
- Machel HG, Mountjoy EW. 1986. Chemistry and environments of dolomitization - a reappraisal. *Earth Science Reviews* 23:175-222.
- Mopper KJ, Zhou KS, Ramana U, Passow Dam HG and Drapeau DT. 1995. The role of surface-active carbohydrates in the flocculation of a diatom bloom in a mesocosm, *Deep-Sea Research* 42:47–73.
- Moreira NF, Walter LM, Vasconcelos C, McKenzie JA, Mccall PJ. 2004. Role of sulfide oxidation in dolomitization: sediment and pore-water geochemistry of a modern hypersaline lagoon system. *Geology* 32:701-704.
- Mowl JL, Gadd GM. 1984. Cadmium Uptake by *Aureobasidium pullulans*. *Journal of General Microbiology* 130: 279-284.
- Neumeier U. 1999. Experimental modeling of beachrock cementation under microbial influence. *Sed. Geol.* 126:35–46.
- Perry T, Klepac-Ceraj V, Zhang XV, McNamara CJ, Polz MF, Martin ST, Berke N, Mitchell R. 2005, Binding of Harvested Bacterial Exopolymers to the Surface of Calcite. *Environmental Science and Technology* 39:8770-8775.
- Raz S, Weiner S, Addadi L. 2000. Formation of high-magnesian calcites via an amorphous precursor phase: possible biological implications. *Advanced Materials* 12: 38-42.
- Revsbech, NP, Jørgensen BB, Blackburn TH. 1983. Microelectrode studies of the photosynthesis and O₂, H₂S, and pH profiles of a microbial mat. *Limnol. Oceanogr.* 28: 1062–1074.
- Sanchez-Roman M, McKenzie JA, de Luca Rebello WA, Rivadeneyra, MA, Vasconcelos C. 2009. Presence of sulfate does not inhibit low-temperature dolomite precipitation. *Earth and Planetary Science Letters*, 285:131-139.
- Sibley DF, Nordeng SH, Borkowski ML. 1994, Dolomitization kinetics in hydrothermal bombs and natural settings. *J. Sed. Research* 64:630–637.

- Stal LJ. 2000. Cyanobacterial mats and stromatolites. In: BA Whitton and M Potts, Eds. *The Ecology of Cyanobacteria: Their Diversity in Time and Space*. Kluwer Academic Publishers, Dordrecht, pp. 61-120
- Sutherland IW. 1995. Polysaccharide lyases. *FEMS Microbiology Reviews* 16:323-347.
- Sutherland IW. 2001. Exopolysaccharides in biofilms, flocs and related structures. *Water Science and Technology* 43:77-86.
- van Gemerden H. 1993. Microbial mats: a joint venture. *Marine Geology*. 113:3–25.
- van Lith Y, Warthmann R, Vasconcelos C, McKenzie JA. 2003. Sulphate-reducing bacteria induce low- temperature dolomite and high Mg-calcite formation. *Geobiology* 1:71–79.
- Vasconcelos C, Mckenzie JA. 1997. Microbial mediation of modern dolomite precipitation and diagenesis under anoxic conditions (Lagoa Vermelha, Rio de Janeiro, Brazil). *J. Sed. Res.* 67:378–390.
- Visscher PT, Reid RP, Bebout BM, Hoefft SE, Macintyre IG, Thompson Jr. J. 1998. Formation of lithified micritic laminae in modern marine stromatolites (Bahamas): the role of sulfur cycling. *Amer. Mineral.* 83: 1482–1491.
- Wang D, Wallace AF, De Yoreo JJ, Dove PM. 2009. Carboxylated molecules regulate magnesium content of amorphous calcium carbonates during calcification. *Proceedings of the National Academy of Sciences* 106:21511-21516.
- Weber J, Woodhead P. 1970. Carbon and oxygen isotope fractionation in the skeletal carbonate of reef-building corals. *Chemical Geology* 6:93–117.
- Weiner S, Dove PM. 2003. An overview of biomineralization processes and the problem of the vital effect. *Rev Mineral Geochem* 54:1–29.
- Wingender J, Strathmann M, Rode A, Leis A and Flemming HC. 2001. Isolation and biochemical characterization of extracellular polymeric substances from *P. aeruginosa*. In: R. Doyle, ed., *Methods in Enzymology*. Academic Press, San Diego, CA 473 p.
- Wright DT. 1999. The role of sulphate-reducing bacteria and cyanobacteria in dolomite formation in distal ephemeral lakes of the Coorong region, South Australia. *Sed. Geol.*, 126:147–157.
- Zorn ME, Muehlenbachs K, Gingras MK, Konhauser KO, Pemberton SG, Evoy R. 2007. Stable isotopic analysis reveals evidence for groundwater-sediment-animal interactions in a marginal-marine setting. *Palaios* 22:546–553.

CHAPTER II

Assessing the importance of organic matrix materials in biofilm chemical reactivity: proton and cadmium adsorption onto purified alginate¹

2.1. Introduction

Microbial biofilms are complex communities comprised of a heterogeneous population of microorganisms, organic matrix materials, and associated authigenic minerals. Structural integrity within the microbial aggregate is established by means of biopolymers secreted by the microbes inhabiting the biofilm, the so-called extracellular polymeric substances (EPS), which account for 50 to 90% of biofilm organic matter (Flemming and Wingender 2001). Bacteria, algae, and fungi are all known to produce EPS, and although the composition of EPS is diverse, they typically consist of repeated chains of modified polysaccharides and their monomeric units, including carboxyl-rich uronic acids, with proteins, lipids, and nucleic acids typically present as relatively minor components (Hunt, 1986; Gadd, 1993; Flemming and Wingender, 2001; Sutherland 2001).

¹*A version of this chapter has been accepted for publication: Petrash DA, Lalonde SV, Raudsepp M, Konhauser KO. 2010. Geomicrobiology Journal. In press.*

Reliable thermodynamic parameters describing the adsorptive properties of EPS biopolymers are required to understand the role of EPS in a variety of geochemical processes, such as in the bioaccumulation of metals (e.g., Bhaskar and Bhosle, 2006), mineral precipitation (e.g., Konhauser et al., 1994), and the use of microbial biomass in contaminated site bioremediation (e.g., Doshi et al., 2008) and wastewater treatment processes (e.g., Guibaud et al., 2006). Several studies have previously examined metal adsorption to bacteria, algae and fungi, with and without EPS, and they rather consistently show that removal of EPS can reduce metal binding capacity (Galun et al., 1983; Majidi et al., 1990; Lui and Fang, 2002; Phoenix et al., 2002). However, due to spatial heterogeneities that arise during differentiation or stratification of regions within a single biofilm, the presence of authigenic and/or detrital mineral components, and the difficulties associated with isolating individual biofilm components (cells, EPS, minerals) in natural samples, the importance of individual EPS components towards overall EPS chemical reactivity is poorly understood.

Accordingly, in this work, I focused on the biopolymer alginate as an effort to better understand the geochemical role of uronic acids as major polysaccharide constituents from EPS (Fazio, 1987; Sutherland, 2001). While EPS composition varies significantly between microorganisms and for a single species, according to factors such as growth rate, nutrient availability, and other stimuli (Christensen and Charaklis, 1990), the common EPS component alginate is the most abundant marine biopolymer and the second most abundant biopolymer on Earth (Melvik and Dornish, 2004). Alginate is a straight-chain, hydrophilic, polyuronic acid extensively secreted by brown algae and several species of bacteria, including *Pseudomonas sp.* and *Azotobacter sp.* (Sutherland 1995) All alginates, whether bacterial or algal, are composed by α -L-guluronate (G) and β -D-mannuronate (M) units linked through 1 \rightarrow 4 glycosidic bonds (Draget et al., 2005). The uronic acids occur as an irregular series of block structures including G-blocks (-G-G-G-G), M-blocks (-M-M-M-M), and M-G-blocks (-M-G-M-G) to form high molecular weight macromolecules ($>10^4$ Da) (Davies et al., 2003, Draget et al., 2005). The only difference between bacterial and algal alginates is that the mannuronic residues of the former are partially acetylated (Sutherland, 1990; Conti, 1994; Saude and Hunter, 2001; Draget et al., 2005), with only minor effect on metal binding (Lee et al., 1996); thus we consider the commercially-

available alginate obtained from the brown algae *Macrocystis pyrifera* as a suitable experimental surrogate that may help to understand metal binding properties of alginates in general.

Recent studies focused on microbial surface reactivity have employed surface complexation modelling (SCM) to quantify, within a thermodynamic framework, the proton buffering and cadmium sorption capacity of diverse biomass, and to link metal sorption behaviour to the reactivity of specific surface functional groups at the cell-water interface (Borrok et al., 2004; Borrok et al., 2005; Daughney and Fein, 1998; Daughney et al., 2001; Yee and Fein, 2001; Haas, 2004). Accordingly, in this study we employ potentiometric titrations and Cd metal sorption assays to develop a surface complexation model permitting direct comparison of the adsorptive properties of purified alginate with data obtained from other EPS studies.

2.2. Material and methods

2.2.1. Materials and Preparation

All glassware was acid-washed in ~10% v/v HCl for 12 hours followed by three rinses, a 12 hour soak, and three more rinses with 18.2 MΩ water. All solutions were prepared gravimetrically and employed within 2 days of preparation. The purified alginate employed in this study, extracted from *Macrocystis pyrifera* (Sigma-Aldrich Canada, Oakville, ON), is a well characterized compound with a MW distribution of 80 to 120 kDa, and a mannuronic/ guluronic acid ratio of ~1.56 (Sigma-Aldrich Canada, Oakville, ON).

2.2.2. Potentiometric Titrations

For alkalimetric titration, 0.1 g of alginic acid sodium salt was dissolved into 40 ml of electrolyte solution (0.01 M NaNO₃) and acidified with 2M HNO₃ to a pH of ~3. A double-junction glass pH electrode (Orion ROSS ultra, filled with 3M KCl) was calibrated using commercial pH buffers (Thermo Fisher Scientific, Nepean, ON; pH 2, 4, 7, 10, 12). The pH electrode was mounted into flasks containing the prepared alkalimetric titration solutions along with a magnetic stir bar; titrant dispenser, thermocouple, and N₂ gas line

with diffusion stone bubbler. Solutions were adjusted to pH ~3 with 2M HCl, sealed with parafilm, and purged with N₂ for 30 minutes prior to, and throughout, titrations, to maintain a CO₂-free atmosphere in the flask.

Titrations were performed alkalimetrically from pH ~3 to 11 using a QC-Titrate autotitrator (Man-Tech Associates Inc., Guelph, Ontario) variably delivering CO₂-free 0.01 M NaOH for 0.1 pH increments with an average equilibration time between additions of ~30 s. Each addition of base occurred only after a pH electrode stability of 0.1 mV/s was attained for a typical total titration time of ~50 min. The proton buffering capacity of the dissolved alginate as a function of pH was determined by least-squares optimization as implemented in FITEQL (Herbelin and Westall, 1999) and all reported charge excess values are relative to the titration starting point (pH ≈ 3.4).

2.2.3. Cadmium adsorption

Cadmium adsorption behaviour of alginate was resolved using a dialysis separation technique, which allowed for the separation of free Cd²⁺ ions in solution from large organic molecules (10⁴-10⁵), with or without complexed Cd, by selective diffusion through a semi-permeable cellulose membrane. Sterilized dialysis tubing (10 mm diameter Spectra-Por cellulose membranes, 12 – 14 kDa cut-off, Cole-Parmer Canada Inc, Montreal, QC) was soaked for 30 min, rinsed three times with 18.2 MΩ water, and filled with ~ 1.1 mL of the electrolyte solution containing ~5 ppm of Cd and adjusted to a pH of 6.0, whereas the pH of the external solution was adjusted to values between 3 and 10 using either 0.1 – 1 M NaOH and HNO₃.

Filled dialysis bags were sealed with 12 mm polypropylene clips and then immersed in 50 ml polypropylene centrifuge tubes containing 40 ml of 0.01 M NaNO₃ electrolyte solution with ~5 ppm Cd and ~1 g/L alginate. By this approach the high molecular weight alginate macromolecules were excluded from the dialysis bag interior while Cd²⁺ and other inorganic ions freely diffused through the membrane until chemical equilibrium was reached. The experimental solutions were left to equilibrate in an incubator at 25°C with constant rotary shaking (40 rpm) for a period of 24 hours, sufficient to achieve metal ion equilibrium between the diffusate and the retentate solutions (Truitt and Weber, 1981). pH values of the retentate were recorded before and after the equilibration period, with the final

pH value assumed to represent equilibrium between the diffusate and retentate. After the equilibration period the contents of the dialysis bags were collected, immediately diluted with 18.2 MΩ water, and acidified with concentrated trace-metal HNO₃.

Cadmium concentrations were determined by using a Perkin Elmer Elan6000 quadruple ICP-MS with a Cd detection limit of 4.2x10⁻⁶ ppm. The concentration of metal adsorbed to biomass in each vessel was calculated by subtracting the concentration of metal that remained in solution from the original Cd concentration in each experiment.

2.2.4. Surface Complexation Modelling

Surface complexation modeling was used to evaluate functional group acidity constants (pK_a), ligand concentrations, and the nature of the metal-organic ligand complexes in alginate solutions. The computer program FITEQL (Herbalin and Westall, 1999), was used to fit thermodynamic parameters (site concentrations and acidity constants) of a discrete-site non-electrostatic surface complexation model to the potentiometric titration data. The charge balance in each titration step was calculated by the following charge balance equation:

$$[C_a - C_b] = [-Q] + [H^+] - [OH^-] \quad (1)$$

Where [C_a - C_b] is the concentration of acid added minus the concentration of base added; [H⁺] and [OH⁻] are the concentrations of protons and hydroxyl ions, respectively, and [-Q] is the negative charge excess owing to deprotonation of alginate in solution, normalized per gram of biomass.

The functional group acidity constant, also called the proton stability constant, (K_a) is determined from the following equation:

$$K_a = [R-A^-] [a_{H^+}] \cdot ([R-AH^0])^{-1} \quad (2)$$

Where R is the root organic molecule, AH⁰ is the protonated functional group, A⁻ is the deprotonated functional group and a_{H⁺} is the proton activity. The pK_a value (pK_a = -log K_a) is the pH at which [R-A⁻] and [R-AH⁰] are present at equivalent concentrations.

The computer program FITEQL was also used to model the Cd adsorption behaviour. Cd activities were determined from concentration data using coefficients calculated by the Davies equation. Adsorption of Cd by a deprotonated functional groups can be generalized by the equation:



Where $\text{R-A}(\text{Cd})^+$ is the Cd-organic complex. The equilibrium constant (K_{CdL}), reported as $\log K_{\text{CdL}}$ in Table 2.3, is given by following equation:

$$K_{\text{CdL}} = \frac{[\text{R-A}(\text{Cd})^+]}{[\text{R-A}^-] [a_{\text{Cd}^{2+}}]} \quad (4)$$

All the reported model parameters are the average of the triplicate experiments with one standard deviation uncertainty calculated as per Johnson et al. (2007) but reported as plus/minus the larger of the positive and negative uncertainties.

2.2.5. FTIR

FTIR spectroscopy was used to elucidate functional group identities in alginic acid sodium salt. The sample was placed on a salt plate (KCl) and focused using a Nic-Plan IR microscope attached to a Nicolet Magna-IR spectrometer 750. Spectra (from 500 to 4000 cm^{-1}) were acquired in absorbance mode and then converted into transmittance. Background spectra of water and of the glass slide were collected prior to measurement of biomass samples for baseline correction and normalization.

2.3. Results and discussion

2.3.1. Characterization of functional group identities and proton reactivity

The relatively simple and well-characterized structure of the alginate monomers mannuronic acid and guluronic acid facilitates the identification of proton-reactive functional groups. On the basis of compositional constraints and proton reactivity over the pH 4-10 range (i.e., excluding hydroxyl protonation/deprotonation reactions), alginate reactivity should be limited to a single carboxyl group per alginate monomer. In the

purified alginate there is an absence of other organic functional groups, typically considered proton-reactive in other biomasses (e.g., Beveridge and Murray, 1980). The FTIR spectrum of our alginate, shows striking similarities with the spectra of *Pseudomonas* EPS obtained by Freitas et al. (2009), with similar bands around 3200 cm^{-1} , $1600\text{--}1404\text{ cm}^{-1}$, and $990\text{--}1300\text{ cm}^{-1}$, representing OH, C=O, and C-O bonds, respectively (Fig. 2.1). In algal-derived alginate, however, there is an absence of the small band at 1732 cm^{-1} owing to the presence of acetyl in bacterial EPS (Freitas et al. 2009). As expected, bands around $1160\text{--}1070\text{ cm}^{-1}$, $1655\text{--}1645\text{ cm}^{-1}$ and $1450\text{--}1380\text{ cm}^{-1}$, representative of phosphoryl, amino I and amino II functional groups, respectively (Won et al., 2005; Eboigbodin and Biggs, 2008; Ueshima et al., 2008), are absent.

Potentiometric titration data of purified alginate similarly indicate that its acid-base behaviour can be accounted for by a single dominant carboxyl functional group. In the excess charge plot (Fig. 2.2), the slope at any given point can be interpreted as the instantaneous buffering capacity at that pH, and excess charge is equivalent to the cumulative surface concentration of deprotonated organic functional groups. For alginate, excess charge increases significantly in the pH 4-6 range, while from circumneutral to alkaline pH, a plateau is observed, indicating an absence of functional groups that are proton-reactive over this range. The excess charge data is best fit by a one-site model with an experimental apparent pK_{a1} value of 3.98 ± 0.01 ($V(Y) = 4.03$; (values less than 20 generally indicate good fit, but see Herbelin and Westall (1999) for discussion of the model variance function $V(Y)$)(Table 2.1). This result is in agreement with: (1) known carboxyl acidity constants (Smith and Martell, 1982), (2) a previously reported value for alginate (4.0; Fourest and Volesky, 1996), and (3) the alginate monomers guluronate and mannuronate (3.38 and 3.65, respectively; Haug et al., 1966).

With respect to functional group site concentrations, the excess charge data indicates that proton reactivity over the pH 4 to 10 range is 1.728 ± 0.027 mmol of protons per dry gram (Table 2.1), as obtained from discrete site modeling using FITEQL (discussed above). The total proton reactivity of purified alginate reported here is comparable to the concentration of carboxyl sites determined by titration for alginate elsewhere (1.78 mmol/g; Fatin-Rouge et al., 2006; 1.96 mmol/g; Jodra and Mijangos, 2003), but is lower than discrete site concentrations reported for various natural organic matter (4–24 mmol/g;

Smith and Kramer 1999)(see Table 2.3). This concentration is comparable to the average bacterial cell surface site concentration (0.32 mmol/wet g, or approximately 2.56 mmol/dry g, based on an average of 36 bacteria and consortia and a wet/dry weight ratio of 8; Borrok et al. 2005), but is restricted in proton reactivity to the pH range 3.5 - 5.5, in contrast to bacterial cells where the surface organic functional groups display a range of acidity constants corresponding to a variety of surface moieties (i.e., phosphoryl, sulfahydryl, amino, phenol, hydroxyl).

2.3.2. Cd adsorption by alginate

Parameters for the adsorption model were derived from the average carboxyl site density, its acidity constant and experimental Cd adsorption data. The resulting Cd sorption isotherm (Fig. 2.3) was modeled under the assumption that sorption occurs solely to the carboxyl site identified by FTIR and titration. Hydroxyl groups are also present in alginate but they only become negatively charged at $\text{pH} > 10$ (Davies et al. 2003) and therefore do not play a role in metal binding over the experimental pH range. For the modeling of Cd adsorption data, a pH range of 3-8 was selected, as appreciable loss of Cd, presumably as the result Cd hydroxide precipitation, was apparent in blank experiments at pH values > 8 (Fig. 2.3).

The Cd sorption isotherm (Fig. 2.3) strongly resembles the excess charge curve obtained from the proton titrations, highlighting the dependence of Cd adsorption on the availability of deprotonated carboxyl functional groups as a function of pH. At low pH, when competition between the metal adsorbate and protons for functional groups is high, very little metal is bound. With increasing pH, progressive deprotonation of carboxyl functional groups provides free ligands for metal sorption; by $\text{pH} \sim 5.5$, close to 90% of Cd complexation by carboxyl functional groups was achieved. Conversely, pH values in our sorption experiments were not low enough to completely prevent metal adsorption, as the lowest pH experiments were conducted within a pH unit of the apparent carboxyl pK_a (Fig. 2.3); the capacity of alginate to form complexes under acid conditions has been previously described by Simsek–Ege et al. (2003).

The fit (solid line) of the FITEQL non-electrostatic Cd adsorption model is also shown in Figure 2.3. The average $\log K_{\text{CdL}}$, -0.52 ± 0.22 (Table 2.2), is compared with

values obtained for other reactive biomass in Table 2.3. The log K_{CdL} value determined here for alginate carboxyl groups is lower than values previously reported for various bacterial EPS matrices, ranging from 1.00 to 2.14 (Guibaud et al., 2008), and is also lower than the average log K_{CdL} of bacterial cell surfaces (Borrok et al., 2005). A primary assumption in most studies of bacterial surface complexation is that carboxyl functional groups are responsible for the majority of metal adsorption at low pH. However, X-ray adsorption spectroscopy of Cd adsorbed to the surfaces of *Bacillus subtilis* at low pH has demonstrated that Cd was bound primarily to phosphoryl functional groups (Boyanov et al., 2003). Importantly, this means that studies which attribute all metal adsorption under acidic conditions to carboxyl ligands may in fact be overestimating the role of the carboxyl ligand in metal sorption. In such cases, the term $[R-A(Cd)^+]$ in the calculation of K_{CdL} may actually comprise two or more functional groups (e.g., carboxyl and phosphoryl). In this study, this is excluded based on alginate compositional constraints, thereby allowing us to better assess the inherent reactivity of carboxyl groups towards Cd. In this regard, it is not surprising that previous studies employing more heterogeneous materials obtained higher K_{CdL} values.

Alternatively, the difference in carboxyl log K_{CdL} between alginate and other similarly-characterized biomass (Table 2.3) may be due to bidentate coordination of divalent metals by adjacent residues in alginate (Fourest and Volesky, 1997; Davies et al., 2003). According to Davies et al. (2003), regions of the alginate polymer rich in guluronic acid (G-blocks), which display a higher selectivity for divalent metal ions, provide a multidentate environment for complexation, while in regions rich in mannuronic acid (M-blocks), complexation is thought to be predominantly unidentate.

Detailed vibrational spectroscopy of alginate (i.e. Fourest and Volesky, 1996; Filipiuk et al., 2004), provides some physical evidence for these assumptions. However, Papageorgiou et al. (2010) recently proposed the reverse scenario for G-block and M-block metal complexation environments, and additionally, the nature of the coordination between divalent metal ions and heteropolymeric sequences (e.g., MGM and GMG blocks) is unexplored. Surface complexation models evaluating monodentate vs. bidentate complexation for M-blocks only, G-blocks only, and both M- and G-blocks simultaneously, provided neither increase in model goodness-of-fit (as indicated by the $V(Y)$ parameter),

nor $\log K_{\text{CdL}}$ values more comparable to previously reported Cd-carboxyl stability constants (data not shown). It is also important to note that molecular structure beyond the functional group may influence functional group pK_a and $\log K_{\text{CdL}}$, and in this respect comparison with data obtained from microbial biomass possessing carboxyl moieties attached to a wide variety of macromolecular backbones entail some difficulties. Future studies aimed at better resolving the coordination environment of alginate-sorbed Cd may be able to distinguish between these competing scenarios.

2.4. Conclusions

By assessing the total functional group site concentration and acidity constant of purified alginate, and by investigating its cadmium adsorption behaviour, this work quantifies the potential role of alginate in metal sorption reactions involving EPS matrices. The commercially available alginate employed here has an apparent acidity constant (pK_a) of 3.98 ± 0.01 and an overall proton adsorptive capacity is 1.73 ± 0.02 mol/kg, lower than values reported for some natural organic matter, but comparable to bacterial cell surfaces; these values are attributed entirely to carboxyl functional groups based on alginate polymer composition. Finally, the cadmium-carboxyl stability constant determined here ($\log K_{\text{CdL}} = -0.52 \pm 0.22$) is lower than those obtained for carboxyl functional groups on more heterogeneous materials such as natural EPS and bacterial surfaces. Together, these results place important constraints on uronic acid contributions to overall EPS reactivity.

Titration number	pK_a	Site concentration (mmol/ g)	V (Y)
1	3.981	1.709	4.08
2	3.968	1.759	4.07
3	3.981	1.720	2.33
Average	3.98 ± 0.01	1.728 ± 0.02	

Table 2-1. Best-fit model parameters for alginate potentiometric titration data. See text for calculation of uncertainties and description of the goodness-of-fit parameter V(Y).

Adsorption Experiment	Log K_{CaL}	V (Y)
A	-0.684	0.66
B	-0.576	0.570
C	-0.362	1.15
Average	-0.52 ± 0.22	

Table 2-2 Best-fit log Cd-carboxyl stability constants for metal adsorption experiments. See text for calculation of uncertainties and description of the goodness-of-fit parameter V(Y).

Organic material or microbial species	Average pK _{a1}	Average cadmium stability constant (log K) attributed to pK _{a1}	Reference
<i>Bacillus subtilis</i> (bacteria)	4.82 ± 0.14	3.4	Fein et al. 1997
Mixtures of gram-negative and positive bacteria	5.0 ± 0.2	3.60 ± 0.32	Yee and Fein 2001, 2003
<i>Pseudokirchneriella subcapitata</i> (algae)	3.9 ± 0.3	4.1 ± 0.5	Kaulbach et al. 2005
<i>Fescue rubra</i> (grass roots)	4.2 ± 0.1	3.5 ± 0.4	Ginn et al. 2008
<i>Geobacillus stearothermophilus</i> (thermophilic bacteria)	3.73 ± 0.04	2.20 ± 0.16	Hetzer et al. 2006
<i>Geobacillus thermocatenulatus</i> (thermophilic bacteria)	3.84 ± 0.03	1.30 ± 0.22	Hetzer et al. 2006
EPS from 7 environmental bacterial strains		-1.72 ± 0.37	Guibaud et al., 2008
EPS from activated sludge		-2.16 ± 0.4	Guibaud et al., 2006
Purified alginate	3.98 ± 0.01	-0.52 ± 0.22	this study

Table 2-3. pK_a values attributed to carboxyl functional groups and log Cd-carboxyl stability constants for various organic materials and microbial cell surfaces and comparison with alginate (this study).

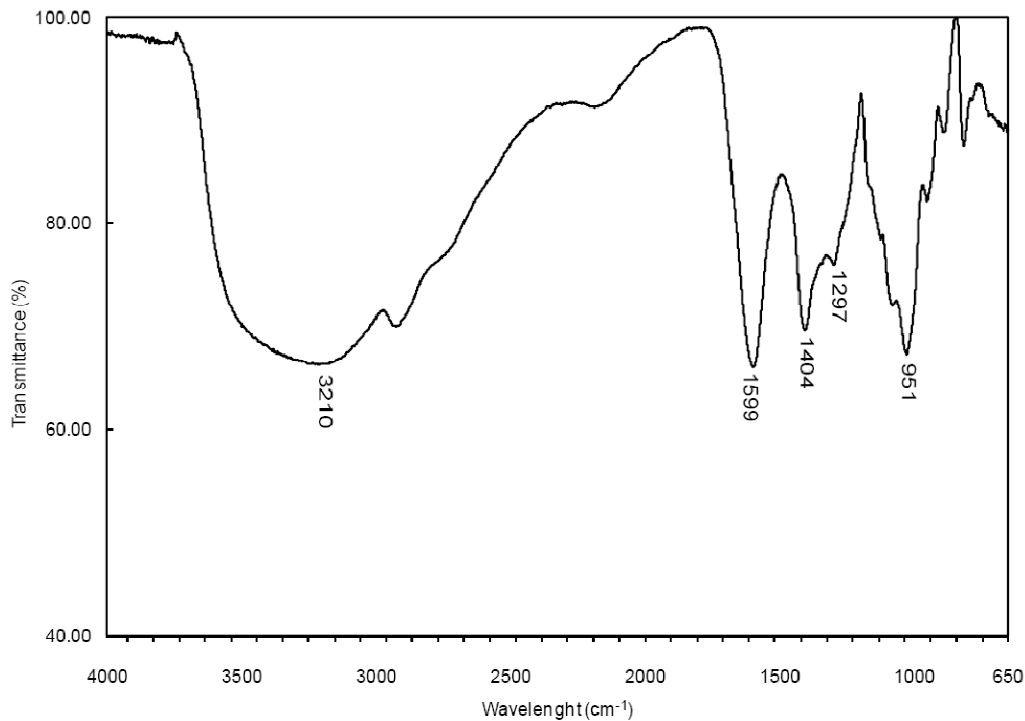


Figure 2-1. FTIR spectra (percent transmittance) of alginic acid sodium salt. The labelled transmittance peaks have been interpreted as 3210: O-H; 1599: C=O stretching; 1404: COO⁻ vibrating; 1026: C-OH stretching and 951: O-H deformation.

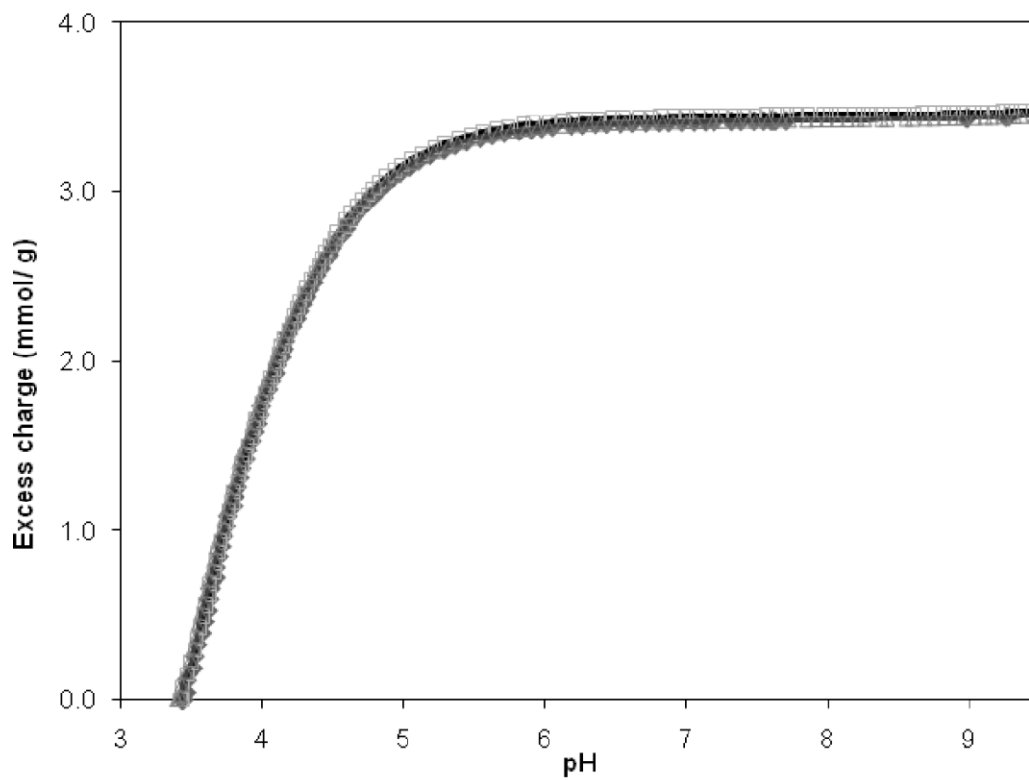


Figure 2-2. Potentiometric titration data for three titrations of alginate in 0.01M NaNO₃ (points). Single-site surface complexation model fits are also displayed for each titration (solid lines).

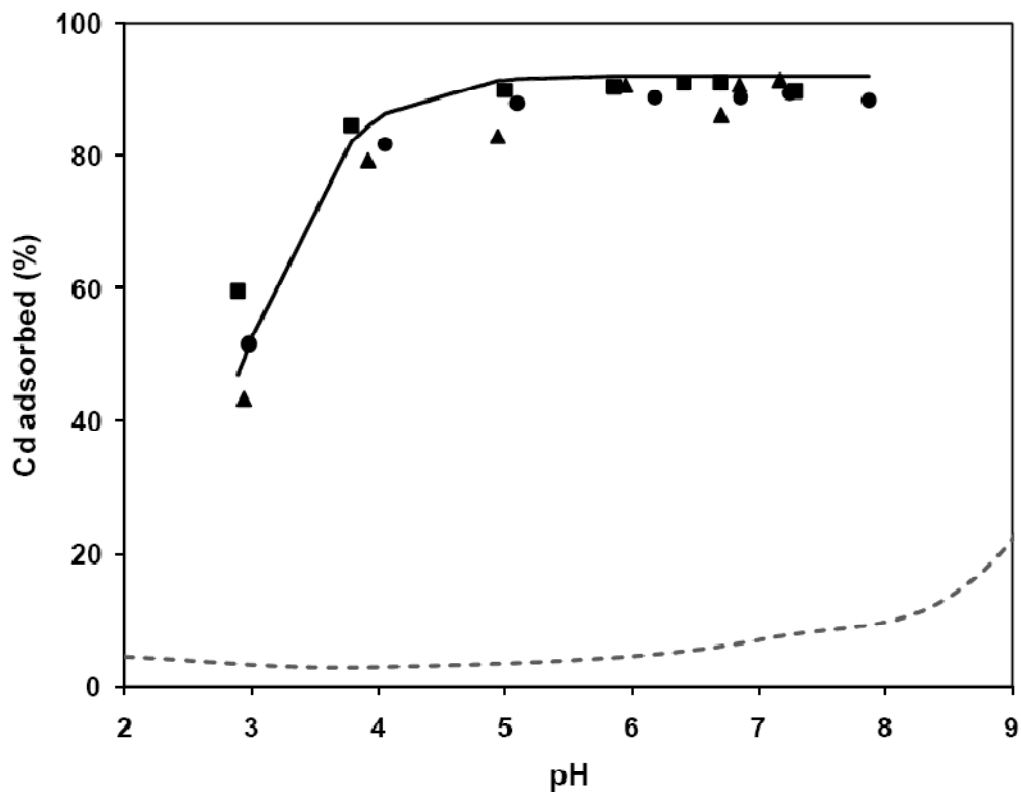


Figure 2-3. Cd adsorption data (in triplicate as circles, squares, and triangles) and the average best-fit surface complexation model (solid line). The dashed curve represents an alginate-free filtered blank. Only data in the pH 3-8 range was employed for Cd adsorption modelling, as some Cd loss, likely due Cd hydroxide precipitation, was observed in blank experiments at more alkaline pH values.

2.5. References

- Bavington CD, Lever R, Mulloy B, Grundy MM, Page CP, Richardson NV, McKenzie, JD. 2004. Anti-adhesive glycoproteins in echinoderm mucus secretions: Comp. Biochem. Physiol. Bull. 139:607–617
- Beveridge TJ, Murray RGE. 1980. Sites of metal deposition in the cell wall of *Bacillus subtilis*. Journal of Bacteriology 141:876–887
- Bhaskar PV, Bhosle NB. 2006. Bacterial extracellular polymeric substance (EPS): A carrier of heavy metals in the marine food-chain. Environment International 32:191-198.
- Borrok D, Fein JB, Kulpa CF. 2004. Proton and Cd adsorption onto natural bacterial consortia: Testing universal adsorption behaviour. Geochimica et Cosmochimica Acta 68:3231–3238.
- Borrok D, Turner BF, Fein JB. 2005. A universal surface complexation framework for modeling proton binding onto bacterial surfaces in geologic settings. American Journal of Science 305:826-853.
- Boyanov MI, Kelly SD, Kemner KM, Bunker BA, Fein JB, Fowle DA. 2003. Adsorption of cadmium to *Bacillus subtilis* bacterial cell walls: A pH-dependent X-ray absorption fine structure spectroscopy study. Geochim. Cosmochim. Acta 67:3299-3311.
- Christensen BE, Charaklis WG. 1990. Physical and Chemical Properties of Biofilms. In: Charaklis WG, Marshall KC, editors. Biofilms. Wiley, New York,. P. 93-130.
- Conti E, Flaibani A, O'Regan M, Sutherland I. 1994. Alginate from *Pseudomonas fluorescens* and *Pseudomonas putida*: production and properties. Microbiology 140:1128–1132.
- Daughney CJ, Fein JB. 1998. The effect of ionic strength on the adsorption of H^+ , Cd^{2+} , Pb^{2+} and Cu^{2+} by *Bacillus subtilis* and *Bacillus licheniformis*: A surface complexation model, J. Colloid Interface Sci. 198:53–77.
- Daughney CJ, Fowle DA, Fortin D. 2001. The effect of growth phase on proton and metal adsorption by *Bacillus subtilis*. Geochimica et Cosmochimica Acta 65:1025–1035.
- Davis TA, Volesky B, Mucci 2003. A review of biochemistry of heavy metal biosorption by brown algae. Water Research 37:4311–4330.
- Davis TA, Kalis EJ, Pinheiro JP, Town RM, van Leeuwen HP. 2008. Cd(II) speciation in alginate gels. Environ Sci. Technol. 42:7242-7247.
- Dragget KI, Smidsrød O, and Skjåk-Braek G. 2005. Alginates from algae. In Steinbüchel A., Rhee SK, editors. Polysaccharides and Polyamides in the Food Industry: Properties, Production and Patents. Wiley-VCH, Weinheim. P. 1-30.

- Doshi H, Ray A, Kothari IL. 2008. Bioaccumulation of heavy metals by green algae. *Current Microbiology* 56:46-255.
- Eboigbodin KE, Biggs CA. 2008. Characterization of the extracellular polymeric substances produced by *Escherichia coli* using infrared spectroscopic, proteomic, and aggregation studies. *Biomacromolecules* 9:686–695.
- Fatin-Rouge N, Dupont A, Vidonne A, Dejeu J, Fievet P, Foissy A. 2006. Removal of some divalent cations from water by membrane-filtration assisted with alginate. *Water Research* 40:1303–1309.
- Filipiuk D, Fuks L, Majdan M. 2004. Transition metal complexes with uronic acids. *Journal of Molecular Structure* 744–747: 705–709.
- Flemming HC, Wingender J. 2001. Relevance of microbial extracellular polymeric substances (EPSs) – Part I: Structural and ecological aspects. *Water Science and Technology* 43:1-8.
- Fourest E, Volesky B. 1996. Contribution of sulfonate groups and alginate to heavy metal biosorption by the dry mass of *Sargassum fluitans*. *Environmental Science and Technology* 30:277-282.
- Fourest E, Volesky B. 1997. Alginate properties and heavy metal biosorption by marine algae. *Applied Biochemistry and Biotechnology* 67:215–226.
- Freitas F, Alves VD, Pais J, Costa N, Oliveira C, Mafra L, Hilliou L, Oliveira R, Rei MAM. 2009. Characterization of an extracellular polysaccharide produced by a *Pseudomonas* strain grown on glycerol. *Bioresource Technology* 100:859-865.
- Gadd GM. 1993. Interaction of fungi with toxic metals. *New Phytologist* 124:25-60.
- Galun M, Keller p, Malki D. 1983. Removal of uranium (VI) from solution by fungal biomass wall-related biopolymers. *Science* 219:285-286.
- Ginn BR, Szymanowski JS, and Fein J.B. 2008 Metal and proton binding onto the roots of *Fescue rubra*. *Chemical Geology* 253:120-135.
- Guibaud G, Van Hullebusch E, Bordas F. 2006. Lead and cadmium biosorption by extracellular polymeric substances (EPS) extracted from activated sludges: pH-sorption edge tests and mathematical equilibrium modelling. *Chemosphere* 64:1955-1962.
- Guibaud G, Bordas F, Saaid A, D'abzac P, Van Hullebusch E. 2008. Effect of pH on cadmium and lead binding by extracellular polymeric substances (EPS) extracted from environmental bacterial strains. *Colloids and Surfaces B: Biointerfaces* 63:48-54.
- Haas JR. 2004. Effects of cultivation conditions on acid–base titration properties of *Shewanella putrefaciens*. *Chemical Geology* 209:67–81.

- Haug A, Larsen B, Smidsrød O. 1966. A study on the constitution of alginic acid by partial acid hydrolysis. *Acta Chem. Scand.* 20:183–190.
- Hetzer A, Daughney CJ, Morgan HW. 2006. Cadmium ion biosorption by the thermophilic bacteria *Geobacillus stearothermophilus* and *G. thermocatenulatus*. *Applied and Environmental Microbiology* 72:4020-4027.
- Herbelin AL, Westall JC. 1999. FITEQL 4.0: a computer program for determination of chemical equilibrium constants from experimental data. Report 99-01. Department of Chemistry, Oregon State University, Corvallis.
- Hunt S. 1986. Diversity of biopolymer structure and its potential for ion-binding applications. In: Ecches, H, Hunt S, editors. *Immobilization of Ions by Bio-Sorption*. Ellis Harwood, Chichester.
- Jodra Y, Mijangos F. 2003. Cooperative biosorption of copper on calcium alginate enclosing iminodiacetic type resin. *Environmental Science and Technology* 37:4362-4367.
- Johnson KJ, Szymanowski JES, Borrok D, Huynh TQ, and Fein JB. 2007. Proton and metal adsorption onto bacterial consortia: Stability constants for metal – bacterial surface complexes. *Chemical Geology* 239:13-26.
- Kaulbach ES, Szymanowski JES, Fein JB. 2005. Surface complexation modeling of proton and Cd adsorption onto an algal cell wall. *Environmental Science and Technology* 39:4060-4065.
- Konhauser KO, Fyfe WS, Schultze-Lam S, and Beveridge TJ. 1994. Iron phosphate precipitation by epilithic microbial biofilms in Arctic Canada. *Can. J. Earth Sci.* 31:1320-1324.
- Körstgens V, Flemming HC, Wingender J, Borchard W. 2001. Influence of calcium ions on the mechanical properties of a model biofilm of mucoid *Pseudomonas aeruginosa*. *Water Science and Technology* 43:49-57.
- Lee JW, Ashby RD, Day DF. 1996. Role of acetylation on metal induced precipitation of alginates. *Carbohydrate Polymers* 29: 337-345.
- Lui H, Fang HHP. 2002. Characterization of electrostatic binding sites of extracellular polymers by linear programming analysis of titration data. *Biotechnology and Bioengineering* 80:806-811.
- Majidi V, Laude DA, Holcombe JA. 1990. Investigation of the metal-algae binding site with ¹¹³Cd nuclear magnetic resonance. *Environmental Science and Technology* 24:1309-1312.

- Melvik JE, Dornish M. 2004. Alginate as a carrier for cell immobilisation. *In* Nedovic V, Willaert R, eds. *Fundamentals of cell immobilisation biotechnology Volume 1*. Springer-Verlag New York. P. 43.
- Papageorgiou SK, Kouvelos EP, Favvas EP, Sapalidis AA, Romanos GE, Katsaros FK. 2010. Metal-carboxylate interactions in metal-alginate complexes studied with FTIR spectroscopy. *Carbohydrate Research* 345:469–473.
- Phoenix VR, Martinez RE, Konhauser KO, Ferris FG. 2002. Characterization and Implications of the Cell Surface Reactivity of *Calothrix* sp. Strain KC97 *Applied and Environmental Microbiology* 68:4827–4834 .
- Simsek-Ege FA, Bond GM, Stringer J. 2003. Polyelectrolyte complex formation between alginate and chitosan as a function of pH. *Journal of Applied Polymer Science* 88: 346–351
- Smith RM, Martell, AE. 1982. *Critical Stability Constants V*. Plenum Press, New York.
- Smith DS, Kramer JR. 1999. Multi-site proton interactions with natural organic matter. *Environment International* 25:307–314.
- Sutherland IW. 1995. Polysaccharide lyases. *FEMS Microbiology Reviews* 16:323-347.
- Sutherland IW. 2001. Exopolysaccharides in biofilms, flocs and related structures. *Water Science and Technology* 43:77-86.
- Saude N, Hunter GA. 2002. Production and molecular weight characteristics of alginate from free and immobilized-cell cultures of *Azotobacter vinelandii*. *Process Biochemistry* 37: 895–900.
- Truitt RE, Weber JH. 1981. Determination of complexing capacity of fulvic acid for copper (II) and cadmium (II) by dialysis titration. *Analytical Chemistry* 53:337-342.
- Ueshima M, Ginn BR, Haack EA, Szymanowski JES, Fein JB. 2008. Cd adsorption onto *Pseudomonas putida* in the presence and absence of extracellular polymeric substances. *Geochim. Cosmochim. Acta* 72:5885-5895.
- Yee N, Fein J. 2001. Cd adsorption onto bacterial surfaces: A universal adsorption edge? *Geochim. Cosmochim. Acta* 65:2037-2042.
- Won SW, Choi SB and Yun YS. 2005. Interaction between protonated waste biomass of *Corynebacterium glutamicum* and anionic dye Reactive Red 4, *Colloids and Surfaces A: Physicochemical and Engineering Aspects* 262:175–180.

CHAPTER III

Assessing the importance of organic matrices: mucin glycoproteins²

3.1 Introduction

In many bioturbated sediment-water systems, mucous secretions occur as either a gel layer directly attached to the burrow wall surface or as a colloidal suspension within the sediment pore waters or the overlying water column (Bonar, 1972; Har-El R and Tanzer, 1993; Storch, 1988; Davis and Viney, 1998). Mucous secretions have many important roles for the survival of infaunal species, including protection against predation, assimilation of nutrients, and stabilization of burrow walls (e.g., Bonar, 1972; Kristensen and Kostka, 2005). These secretions also serve as organic substrates facilitating bacterial colonization and the establishment of complex burrow wall microenvironments, a factor that has been linked to distinctive biomineralization processes occurring within burrow walls (Aller, 1982; Kristensen, 1983; Furukawa, 2001). Mucin, a compound comprising a network of proteins, polysaccharides and water, is the most important macromolecular component of mucus gels. Polyelectrolyte functional groups within the structure of this glycoprotein

² A version of this chapter has been submitted for publication: Petrash DA, Lalonde SV, Konhauser KO. 2010. *Biomacromolecules*. Manuscript ID: bm-2010-00945g

deprotonate under typical physicochemical conditions of marine pore water systems, conferring a net negative surface charge that can react with dissolved metal cations (Marriott and Gregory, 1990; Bansil and Turner, 2006). Therefore, these organic substances have the potential to affect elemental cycling and mineral nucleation at the burrow-seawater interface much as bacterial communities do within the sediment matrix. To date, only one study has attempted to ascertain the metal binding capacity of natural worm mucus. On the basis of FTIR data, Bavington et al. (2004) demonstrated that significant homology in the composition of mucous secretions appear to exist across marine metazoa, while chemical titration and metal adsorption analyses of the mucous secretions of the Terebellid polychaete (Lalonde et al. 2010) showed that it possesses a high density (per unit mass) of organic functional groups that are strongly metal-reactive.

Mucin has been difficult to characterize owing to its large molecular weight, polydispersity, gel-forming tendencies, and the high degree of glycosylation of its oligosaccharides (Bansil et al., 1995; Bansil and Turner, 2006). The separation of the mucin glycoprotein from the mucous material of burrowing animals (and associated mineral components) is fraught with difficulty because current separation procedures (i.e., high-speed centrifugation, ultrasonication, acid and base treatments) are known to perturb the mucin macromolecular structure, introduce impurities, and decrease the molecular weight of mucins (Davis and Viney, 1998). Furthermore, in natural environments, the gel-forming biomolecule is often intimately associated to active microbial consortia and crystallite-sized mineral phases. In this regard, examining natural mucous secretions make the identification of a suitable commercial analogue highly desirable. Type III porcine gastric mucin (PGM) represents a strong candidate among other likely analogues because of its well-characterized composition, wide commercial availability, and its similarity (inferred by FTIR spectra) with marine animal mucous secretions (e.g., Bavington et al., 2004).

3.2 Methods

3.2.1. FTIR spectra

Type III porcine mucin (Sigma-Aldrich Canada, Oakville, ON) was analyzed by Fourier Transform Infrared Spectroscopy (FTIR) in order to determine the bond types and

identities of its organic functional groups. A dry sample was placed on a salt plate (KCl) and then examined using a Nic-Plan IR microscope attached to a Nicolet Magna-IR spectrometer 750. Spectra were acquired from 600 to 4000 cm^{-1} in absorbance mode and converted to transmittance.

3.2.2 Acid-base titration

For alkalimetric titration, solutions of Type III crude porcine gastric mucin were prepared gravimetrically to concentrations of approximately 3.0 and 1.0 dry g/L in 0.01M NaNO_3 and acidified with 2M of trace metal grade HNO_3 to a pH of ~ 3.0 . A pH electrode (Orion ROSS ultra), filled with 3M KCl, was calibrated using commercial pH buffers and mounted into flasks containing the titrate solutions along with a magnetic stir bar, titrant dispenser, thermometer, and an Ar gas line. Both the titrate and titrant were stored in closed containers and bubbled for 30 min with Ar gas to expel CO_2 from the system prior to, and throughout, titrations. Alkalimetric titrations were conducted using a PC-Titrate auto-titrator (Mandel Scientific, Guelph, Ontario) programmed to deliver aliquots of 0.01 ± 0.0001 M NaOH (commercial titrant, Thermo Fisher Scientific, Waltham, MA).

Titrations were performed in triplicate from pH 3 to 11 in increments of approximately 0.1 pH units per addition; the suspension was allowed to equilibrate after each base addition prior to the addition of the next aliquot of base, with equilibrium operationally defined as a drift of 0.5 mV/s or less. Each titration lasted approximately 1 hour, with sample temperature remaining approximately constant (23 ± 1 °C) throughout all titrations.

Titration data were modelled using the least-squares optimization as implemented in FITEQL 4.0 (Herbelin and Westall, 1999) in order to obtain site concentrations and acidity constants for the proton-active functional groups present in the mucin. A non-electrostatic model was chosen as only one ionic strength was explored (0.01 M), and previous studies have demonstrated that electrostatic surface field effects on protonation are minimal for bacterial surfaces (Borrok and Fein, 2005) and humic/fulvic acids (Borrok and Fein, 2004). FITEQL employs a least-squares optimization during fitting to iteratively minimize a variance function, $V(Y)$, between the experimental data and the model; a variance of less

than 20 is considered a good fit to the experimental data (the FITEQL variance function is additionally discussed by Herbelin and Westall (1999)).

The charge balance in each titration step was calculated by the following charge balance equation:

$$[C_a - C_b] = [-Q] + [H^+] - [OH^-] \quad (3.1)$$

where $[C_a - C_b]$ is the concentration of acid added minus the concentration of base added; $[H^+]$ and $[OH^-]$ are the concentrations of proton and hydroxyl ions, respectively, and $[-Q]$ is the negative charge excess owing to deprotonation of alginate in solution, normalized per gram of biomass. For titration data modeling, site concentrations and acidity constants (expressed here as pK_a , equivalent to $-\log K_a$) were iteratively adjusted by FITEQL to fit charge excess vs. pH data for a pre-determined number of discrete sites (1-3).

3.2.3. Cadmium complexation

Cadmium adsorption behaviour of mucin was examined using a dialysis separation technique that facilitates separation of free Cd ions from mucin macromolecules and its Cd complexes by selective diffusion through a semi-permeable cellulose membrane (10 mm diameter Spectra-Por cellulose membranes, 12-14 kDa cut-off, Cole-Parmer Canada Inc, Montreal, QC). The dialysis membranes were soaked for 30 min and washed 3 times with 18.2 M Ω water in order to remove organic surfactants from the membranes. Solutions of 0.01 M NaNO₃ with a concentration of ~5mg/L of Cd (from a 1000 ppm commercial standard solution, Thermo Fisher Scientific, Waltham, MA) were prepared in triplicate. The dialysis tubes were then filled with ~ 1.1 mL of the Cd solution, previously adjusted to a pH of 6.0 with metal trace grade HNO₃, and sealed with 12 mm polypropylene clips.

Two average biomass ratios were experimentally tested, 1.48 and 4.15 g mucin/L, with each conducted in triplicate. Once the solutions were mixed by magnetic stirring (achieving a gel consistency), 40 ml aliquots were added into 50 ml polypropylene centrifuge tubes and then the pH of the Cd-organic solution in each individual tube was adjusted to values between 3 and 10, in increments of one pH units, followed by immersion of the filled bags within the centrifuge tubes.

The experiments were left to equilibrate in an incubator at 25°C at constant shaking (40 rpm) for a period of 24 hours, as metal ion equilibrium between the diffusate and the retentate solutions should be reached in less than 24 hr (Truitt and Weber, 1981). Cadmium remains largely in the form of Cd²⁺ over most of the pH range of natural marine pore waters. In the adsorption experiments, Cd ion adsorbed to mucin reactive sites are retained entirely outside the cellulose membrane, as the membrane cut-off, 1.2 to 1.4 x 10⁴ Da, is much lower than the average molecular molar mass (1.6 x 10⁶ Da) of the commercial porcine mucin product (Davies and Viney, 1998). Thus, once equilibrium was reached, the total concentration of Cd²⁺ inside the bag was considered to be equal to free Cd²⁺ in the system, and the contents of the dialysis bags were collected, immediately diluted with 18.2 MΩ water, and acidified with concentrated trace-metal HNO₃.

Cd concentrations were analyzed by atomic absorption spectroscopy (Perkin Elmer 3000) to determine the proportion of free Cd²⁺ at the various experiment pH values. Cd activities were determined from concentration data using coefficients calculated by the Davies equation. Equilibration with respect to free Cd²⁺ is assumed to occur across the membrane such that Cd concentrations in the mucin-free compartment reflect equilibrium between mucin-bound and free Cd²⁺. For the following reactions (for ligands L₁ to L₃):



Best-fit equilibrium constants for Cd²⁺-mucin complexes were found by least-squares optimization as implemented in the computer software FITEQL 4.0. Cd-ligand stability constants are defined as:

$$K_{CdL} = [R-L_n (Cd)^{+1}] \cdot ([R-L_n^-] [a_{Cd^{2+}}])^{-1} \quad (3.3)$$

The values reported are averages from triplicate experiments.

3.3 Results and Discussion

3.3.1. FTIR spectra

The FTIR spectra of porcine gastric mucin (Figure 3.1A) is broadly consistent with spectra previously reported for Terebellid polychaete mucous secretions (Figure 3.1B;

Lalonde et al., 2010), as well as other natural mucin-type glycoproteins in general (see Bavington et al., 2004, Fig. 3.3). On the basis of the known mucin compositional constraints (Bansil and Turner, 2006), the spectral bands around 2850 cm^{-1} , $1550\text{-}1450\text{ cm}^{-1}$, and $1240\text{-}1050\text{ cm}^{-1}$, are interpreted as bonds associated to glycosaminoglycans (See Table 3.1). Bands around 1538 cm^{-1} , and 1640-cm^{-1} , are representative of amino II, and amino I functional groups, respectively; various C-H stretching modes are present at 2850 and 2919 cm^{-1} .

The striking similarities in the spectral response of PGM and Terebellid mucous (Table 3.1, Fig. 3.1) arise from the common organic functional groups comprising mucin-type glycoproteins, a deeply-branching and compositionally conserved constituent of animal epithelial secretions (Bavington et al., 2004; Lang et al., 2007). Carbohydrates, primarily *N*-acetylgalactosamine, *N*-acetylglucosamine, galactose, sialic acid (*N*-acetylneuraminic acid), with trace amounts of mannose and sulfate, comprise approximately 80% of mucin's molecular mass (Bansil and Turner, 2006). The oligosaccharides are arranged in *O*-linked chains containing 5 to 30 monomeric units and are attached to the protein core by *O*-glycosidic bonds to the hydroxyl side chains of amino acids serine and threonine, which are exposed by the protein core (Davis and Viney, 1998; Bansil and Turner, 2006).

The protein core, making up approximately 20% of the average molecular mass (200–500 kDa), possesses two distinct regions (Bansil and Turner, 2006). One is a central glycosylated region comprised of repeating units (up to 60%) of the amino acids serine, threonine, and proline. At the amino and carboxyl terminals, regions are more representative of globular proteins, and are high (> 10%) in cysteine; it is this region that is believed to confer viscoelasticity of mucin oligomers by extensive disulfide bonding between cysteines (Gum et al., 1992). While the composition of mucin appears relatively conserved among different animals, and secretions produced by dissimilar species share many common features (Bavington et al., 2004; Stabili et al., 2009) there may be heterogeneities related to specialized roles that mucus performs in marine invertebrates (Storch, 1988, Mastrodonato et al., 2006). At least in terms of available functional groups, the similarity in the FTIR spectra of both PGM and Terebellid worm secretions indicate

that the former is an appropriate experimental surrogate for examining the sorptive properties of marine invertebrate mucin glycoproteins.

3.3.2 Potentiometric titrations

Figure 3.2A shows all titration data plotted in terms of millimoles of deprotonated sites (or charge excess) per unit of mucin dry mass (see supplementary online data). The slope at any given point can be interpreted as the instantaneous buffering capacity at that pH; PGM displayed a significant buffering capacity over the entire pH range of this study (4–10). The excess charge data was best fit by a three-site model, with apparent pK_a ($-\log K_a$) values of 4.82 ± 0.03 , 7.08 ± 0.12 and 9.30 ± 0.01 . The model site distributions are shown at Figure 3.2B, and based on the functional group acidity constants, as well as the concentrations of functional group, their compositional data, and FTIR spectra, it appears that the three sites most likely correspond to carboxyl, phosphoryl, and thiol and/or amine organic functional groups, respectively.

Functional group site concentrations between pH 4 to 10 total $17.27 \pm 1.05 \text{ mmol g}^{-1}$ (dry) (FITEQL modeling, Table 3.2). The total proton reactivity of PGM reported here is elevated relative to other naturally occurring biomass, i.e., fulvic substances (averaging 7.74 mmol/g ; Milne et al., 2001) and Terebellid mucous secretions ($11.26 \pm 1.79 \text{ mmol}\cdot\text{g}^{-1}$; Lalonde et al., 2010). The extended fibrous structure of mucin, approximately 400 nm in length at pH 5-7 (Hong et al., 2005), may provide proton access to sites that would otherwise be inaccessible in other, more condensed natural organic macromolecules. Importantly, PGM has a buffering capacity that is evenly distributed over the pH range of most marine pore water systems. At seawater pH, nearly two thirds of its total ligands will be deprotonated and available to participate in metal cation adsorption reactions.

3.3.3. Cd adsorption

Dialysis-assisted Cd sorption experiments permit a direct comparison of the affinity of PGM functional group sites for dissolved Cd^{2+} relative to other biosorbents. We evaluated metal-ligands stability constants using Cd for several reasons: (1) to facilitate comparison with the work of Lalonde et al. (2010) evaluating metal adsorption involving worm mucous secretions; (2) Cd remains soluble over the pH range of interest; and (3)

relevance to near-shore ocean and estuary waters where Cd concentrations may be elevated and worms are known to thrive.

For sites 1 and 2, Cd stability constants were modeled using the average PGM site concentrations and their acidity constants (Table 3.2), combined with experimental Cd adsorption data (see online supplementary material). For the experimental pH range and the two metal/mucin ratios (~1.5 and 4.2 g/L) examined in this study, simple monodentate surface complexation of free Cd²⁺ by deprotonated surface sites adequately described Cd²⁺ adsorption behaviour. The best-fit was achieved when two sites participated in Cd adsorption (Fig. 3.3A). The Cd-ligand stability constants (as -log K_{Cd} values) determined for these ligands are 2.54 ± 0.11 and 3.89 ± 0.30, comparable to those previously reported for corresponding sites in the Terebellid worm mucous secretions (-log K_{Cd} values of 2.19 and 3.86; Lalonde et al., 2010). In experiments with a high mucin/metal ratio (~4.2 g/L; Fig. 3.3A), nearly complete removal of Cd from solution occurs at a pH above 6, and a plateau in the adsorption edge is observed.

A decrease in the mucin/metal ratio leads to a depressed adsorption edge, and Cd adsorption to more than one functional group is required to fit the data (Fig. 3B); as site one becomes saturated and metal complexation reaction occurs with both site 1 and site 2. This is illustrated graphically in Figure 3.3C, where the relative roles of sites 1 and 2 in Cd sorption are calculated from Table 3.2 model parameters. The role of site 3 in metal sorption by PGM could not be resolved, partially due to the use of Cd and its precipitation as Cd(OH)_{2(s)} at alkaline pH. With regards to this site, given that thiol functional groups are inherent to the cysteine-rich domains of mucin substances and present in PGM (as indicated by previous compositional constraints, FTIR, and potentiometric titration), it is likely that thiols confer an unusually high affinity for Cd in the alkaline pH range as observed in Terebellid mucus (Lalonde et al., 2010).

3.3.4. PGM as an analog in bioturbation studies

Burrow walls serve as a locus for intense chemical activity, as evidenced by steep gradients in pH, dissolved O₂, and other geochemical parameters in their vicinity (Furukawa, 2001; Zhu, 2006). The polyanionic nature of the mucin glycoproteins composing animal mucus can strongly influence the speciation and mobility of dissolved

metals in contact with burrow wall linings (Lalonde et al., 2010). In turn, this is expected to influence biomineralization processes in bioturbated environments (e.g. Over, 1988; Zorn et al., 2007). A threefold mechanism by which mucin would induce biomineralization in bioturbated sediments is envisioned as follows: First, adsorption of divalent metals (i.e. Ca^{2+} , Mg^{2+} , Fe^{2+} , etc) in their ionic will form complexes with mucin organic ligands, to create an gel-like matrix near-saturated or even over-saturated in bioactive metals, where a symbiotic microbial consortia will flourish. Second, heterotrophic members of such a consortium will partially degrade the glycoprotein-rich mucin substrate, establishing pH gradients around and across the burrow wall (e.g., Zhu, 2006), likely with strong effects on the speciation and adsorption of metal cations, as well as the solubility of mineral phases. Third, more complete degradation of organic functional groups by heterotrophic members of the burrow wall microbial consortia may result in divalent metal release, and perhaps re-precipitation, in the wall microenvironment. Interestingly, several proteins and other organic macromolecules are known to have specificity for certain metals over others. It is thought that the molecular arrangement of glycoproteins may confer them unique abilities to promote and stabilize the formation of calcites (e.g., Aizemberg et al., 1996). For instance, a region rich in aspartic-acid in the biomolecular structure of a glycoprotein secreted by bivalves is known to preferentially bind Mg^{+2} (Gotliv et al., 2005). In a similar context, a histidine-rich glycoprotein (HRG) has been investigated previously for its relative metal affinity, showing affinity in the order $\text{Zn}^{2+} > \text{Ni}^{2+} > \text{Cd}^{2+}$ (Guthans and Morgan, 1982), but otherwise, the general affinity sequence of glycoproteins for dissolved metals is largely unknown at present.

The separation of the mucin glycoprotein from the mucous material of burrowing animals (and associated mineral components) is fraught with difficulty because current separation procedures (i.e., high-speed centrifugation, ultrasonication, acid and base treatments) are known to perturb the mucin macromolecular structure, introduce impurities, and decrease the molecular weight of mucins (Davis and Viney, 1998). Mucin has been difficult to characterize owing to its large molecular weight, polydispersity, gel-forming tendencies, and the high degree of glycosylation of its oligosaccharides (Bansil et al., 1995; Bansil and Turner, 2006). Furthermore, in natural environments, the gel-forming biomolecule is often intimately associated to active microbial consortia and crystallite-sized

mineral phases. We demonstrate here that commercially-available PGM is highly similar to mucous secretions isolated from Terebellid polychaete burrows in terms of functional group identities, site concentrations, acidity constants, and Cd metal stability constants, and should thus be considered a simple and well-suited analog for laboratory study of chemical and biomineralization reactions occurring in the mucus matrix of animal burrow walls.

3.4. Conclusions

It has been demonstrate here that commercially-available PGM is highly similar to mucous secretions isolated from Terebellid polychaete burrows in terms of functional group identities, site concentrations, acidity constants, and Cd metal stability constants, and should thus be considered a simple and well-suited analog for laboratory study of chemical and biomineralization reactions occurring in the mucus matrix of animal burrow walls. Considering the influence that mucous substances likely exert over chemical reactivity, mass transfer, and biomineralization at the bioturbated sediment-water interface, the identification of a suitable analog for the study of difficult-to-isolate infaunal animal mucus is highly desirable. We conclude that PGM represents one such analog that is readily available, inexpensive, well characterized, easy to employ, and well-matched in terms of composition and surface chemical reactivity to naturally occurring infaunal animal mucus secretions.

Peak Absorption Frequency (cm ⁻¹)		Peak assignment
PGM	Terebellid mucus	
1055-1076	1070	C-O stretching of complex sugars, S=O stretching
-	1180	S=O stretching
1237	1230	Acetyl C-O-C
1451	1448	CH ₂ scissoring
1538	1543	N-H bending (amide II)
1640	1656	N-acetyl C=O stretching (amide I)
2850,2919	2851,2926	C-H stretching

Table 3-1. FTIR peak absorption frequencies and tentative peak assignments of PGM and comparison with Terebellid mucus.

Site	Average pK_a	Average C (mmol/dry g)	log K_{cal}
1	4.82 ± 0.02	5.73 ± 0.23	2.54 ± 0.11
2	7.08 ± 0.12	4.67 ± 0.40	3.89 ± 0.30
3	9.30 ± 0.01	6.89 ± 0.43	-

Table 3-2. Titration data modeling, acidity constants and site concentrations (expressed here as pK_a , equivalent to $-\log K_a$) and calculate log K values for Cd complexation sites at mucin biomass. Experimental method constraints not allowed to evaluate the log K of site 3 (see text for explanation).

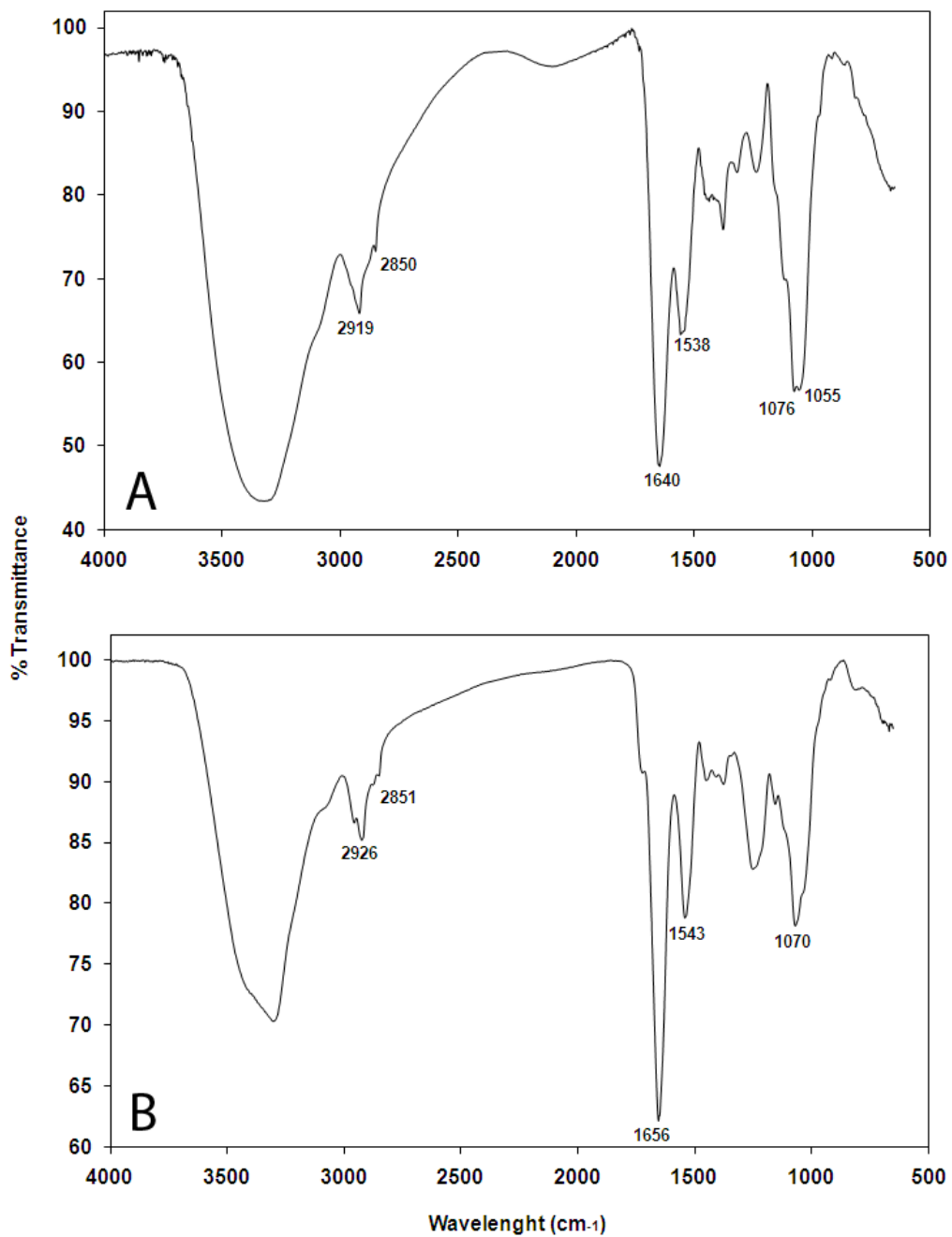


Figure 3-1. FTIR spectra of (A) Type III PGM (this study), and (B) the *Tereballid* worms mucous secretion (Lalonde *et al.*, 2010).

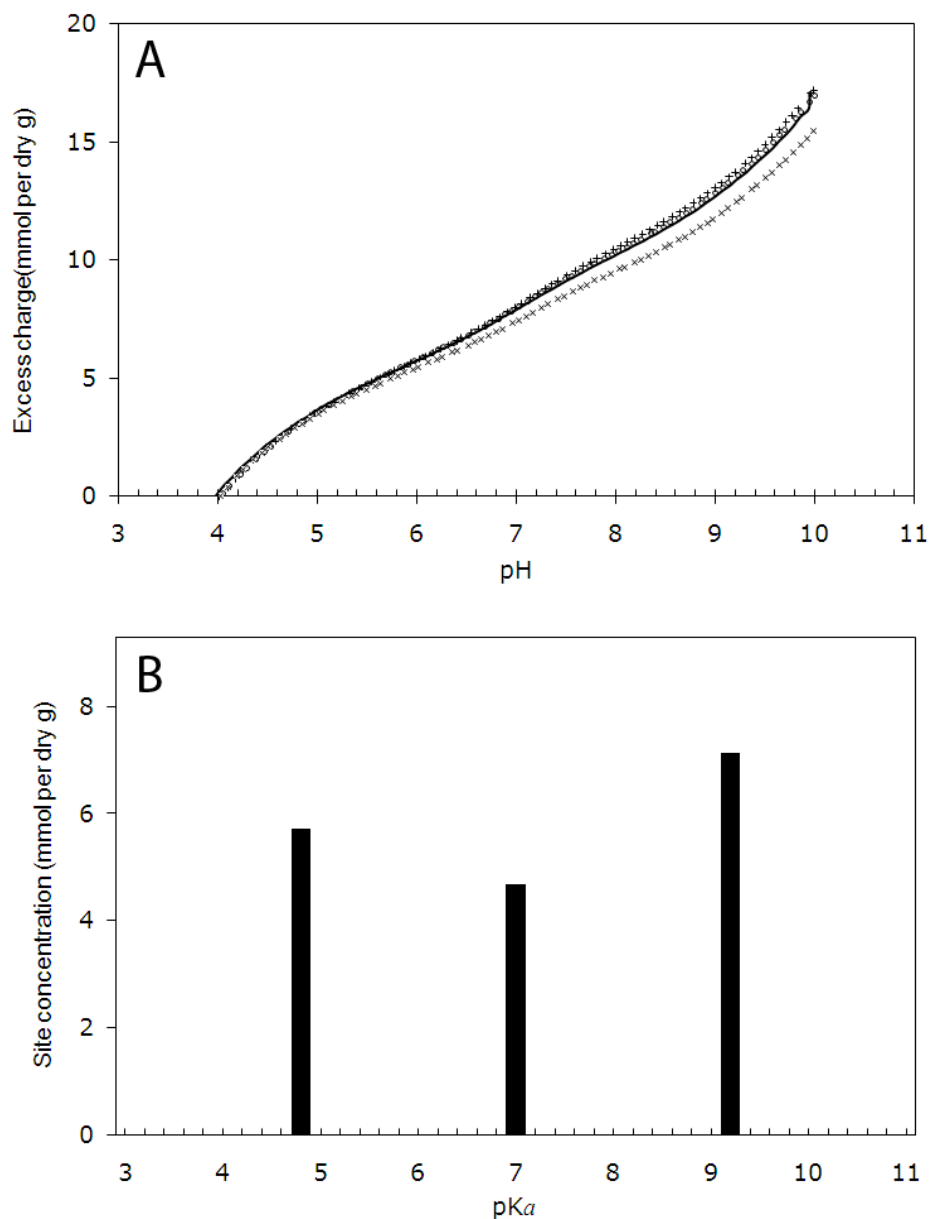


Figure 3-2 (A) Potentiometric titration data (points) for three titrations of PGM in 0.1 M NaNO₃. Also displayed is a solid line representing the best-fit 3-site surface protonation model. (B) Average best-fit discrete site model obtained by least-squares optimization of titration data as implemented in FITEQL 4.0 (Westall, 1982). The model represents the set of functional groups, in terms of concentration (y-axis) and acidity constant (x-axis) that best describes the charge excess data. The acidity constant is represented as pK_a (-log K_a), which is approximately equivalent to the pH at which an equal amount (50%) of sites are in protonated and deprotonated forms.

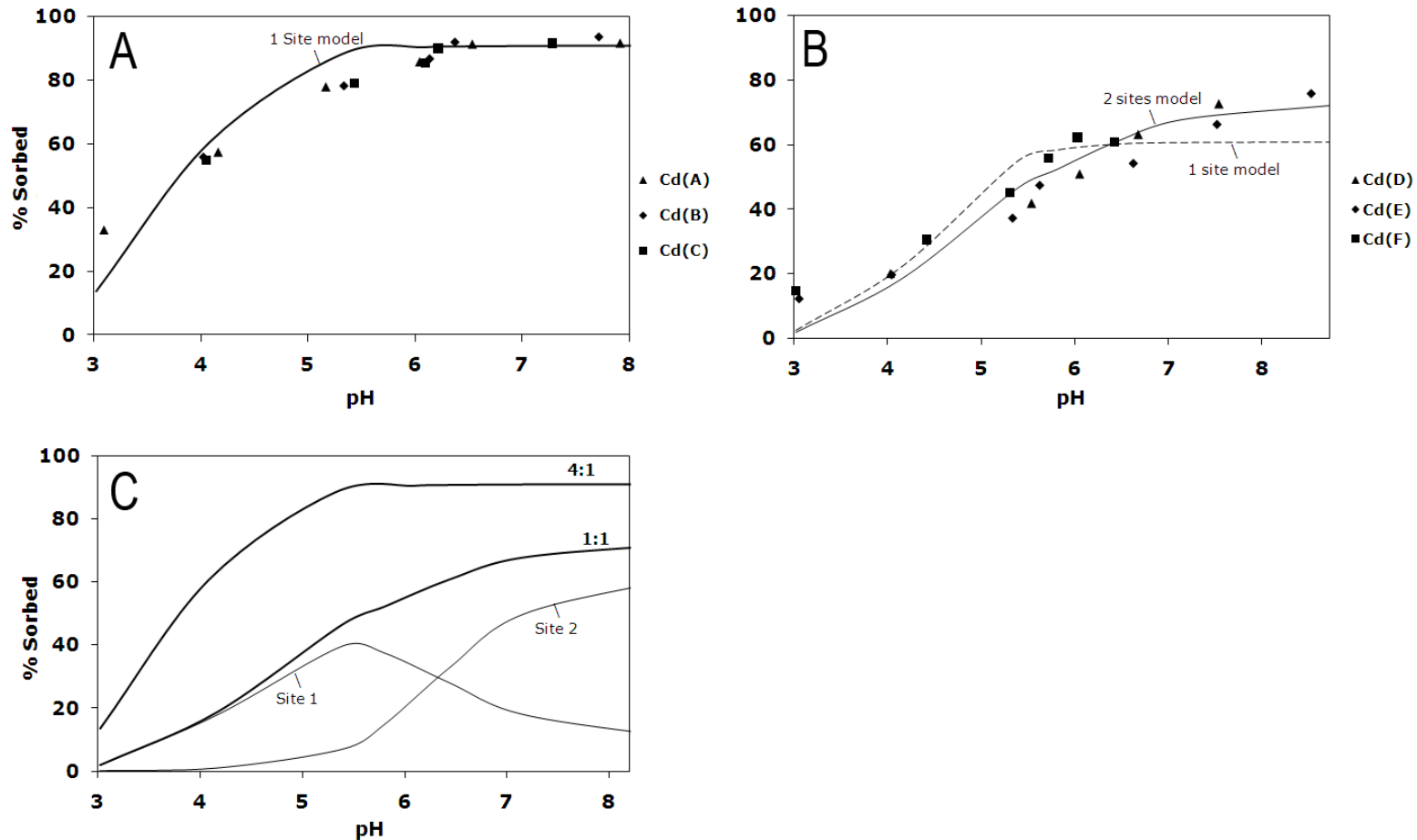


Figure 3-3. Cd sorption in 5 ppm Cd –mucin solutions. A: with 4.17 g/L mucin (Experiments A, B and C). B: with 1.48 g/ L mucin (Experiments D, E and F). C: At high mucin:Cd ratios (4:1), complete adsorption of Cd occurs to one functional group at a pH below 6. In experiments conducted with low Cd to mucin ratio the sorption behaviour can be explained solely by Cd complexation into the reactive site 1. See text for further explanation.

3.5. References

- Aizenberg J, Lambert G, Addadi L, Weiner S. 1996. Stabilization of amorphous calcium carbonate by specialized macromolecules in biological and synthetic precipitates. *Adv. Mater.* 8:222–226.
- Aller RC. 1982. The effects of macrobenthos on chemical properties of marine sediment and overlying water In: Mccall MJS, Tevez PL, editors. *Animal–sediment relations*. Plenum Publishing Company, New York, P. 53-102
- Bansil R, Stanley E, Lamont J. 1995. Mucin biophysics: *Annu. Rev. Physiol.* 57:635–5657.
- Bansil R, Turner BS. 2006. Mucin structure, aggregation, physiological functions and biomedical applications: *Current Opinion in Colloid and Interface Science* 11:164– 170.
- Bavington CD, Lever R, Mulloy B, Grundy MM, Page CP, Richardson NV, Mckenzie, JD. 2004. Anti-adhesive glycoproteins in echinoderm mucus secretions: *Comp. Biochem. Physiol. Bull.* 139:607–617
- Bonar DB. 1972. Feeding and tube construction in *Chone mollis* Bush (polychaeta, Sabellidae): *J. Exp. Mar. Biol. Ecol.* 9:1–18.
- Borrok DM, Fein JB. 2005. Adsorption of protons, Pb, Cd, and Sr onto the surfaces of two gram-negative aerobic bacteria at different ionic strengths: *J. Colloid Interface Sci.* 286:110–126.
- Borrok DM, Fein JB, Kulpa CF. 2004. Proton and cd sorption onto natural bacterial consortia: testing universal adsorption behaviour: *Geochim. Cosmochim. Acta* 68:3231-3238.
- Davis JM, Viney C, 1998, Water-mucin phases: conditions for mucus liquid crystallinity: *Thermochim. Acta* 315:39–49.
- Furukawa Y. Biogeochemical Consequences of Infaunal Activities. *Macroand Microorganisms in Marine Sediments Coastal and Estuarine Studies*; 2005. Available at: <http://www.stormingmedia.us/12/1235/A123564.html>.
- Gotliv BA, Kessler N, Sumerel JL, Morse DE, Tuross N, Addadi L, Weiner S. 2005. Asprich: a novel aspartic acid-rich protein family from the prismatic shell matrix of the bivalve *Atrina rigida*. *Chem, Biochem.* 6:304-314
- Gum JR Jr, Hicks JW, Toribara NW, Rothe EM, Lagace, RE, Kim YS. 1992. The Human Muc2 intestinal mucin has cysteine-rich subdomains located both upstream and downstream of its central repetitive region. *The J. of Biol. Chem.* 267:21375-21383.

- Har-El R and Tanzer ML. 1993. Extracellular matrix 3: evolution of the extracellular matrix in invertebrates: FASEB Journal 7:1115-1123.
- Herbelin AL, Westall JC. 1999. FITEQL 4.0: a computer program for determination of chemical equilibrium constants from experimental data; report 99-01, Department of Chemistry Oregon State University, Corvallis.
- Hong Z, Chasan B, Bansil R, Turner BF, Bhaskar KR. 2005. Atomic force microscopy reveals aggregation of gastric mucin at low pH. *Biomacromolecules* 6: 3458–3466.
- Kristensen E. 1983. Ventilation and oxygen uptake by three species of Nereids (Annelida: Polychaeta). *Effects of hypoxia: Mar. Ecol. Prog. Ser.* 12: 289-297.
- Kristensen E, Kostka JE, 2005. Macrofaunal burrows and irrigation in marine sediment: microbiological and biogeochemical interactions. In: Kristensen E, Haese RR, Kostka JE, editors. *Interactions between macro- and microorganisms in marine sediments: Coastal and Estuarine Studies* 60. American Geophysical Union, Washington, D.C.
- Lalonde SV, Dafoe L, Pemberton SG, Gingras MK, Konhauser KO, 2010. Investigating the geochemical impact of burrowing animals: proton and cadmium adsorption onto the mucus lining of *Terebellid* polychaete worms: *Chem. Geol.* 271:44-51.
- Mastrodonato M, Gherardi M, Todisco G, Sciscioli M, Lepore E. 2006. The epidermis of *Timarete filigera* (Polychaeta, Cirratulidae): histochemical and ultrastructural analysis of the gland cells. *Tissue & cell* 38(5):279-84.
- Marriott C, Gregory NP. 1990. Mucus physiology and pathology, in, v. Lanaerts and R. Gurny, editors. *Bioadhesive Drug Delivery Systems: CRC Press, Florida*, pp. 1–24.
- Mastrodonato M, Gherardi M, Todisco G, Sciscioli M, Lepore E. 2006. The epidermis of *Timarete filigera* (Polychaeta, Cirratulidae): histochemical and ultrastructural analysis of the gland cells. *Tissue & cell* 38:279-84.
- Over DJ. 1988. Lingulid brachiopods and *Lingulichnus* from a Silurian shelf-slope carbonate sequence, Delorme Group, Mackenzie Mountains, Northwest Territories. *Can. J. Earth Sci.* 25: 465–471.
- Stabili L, Schirosi R, Licciano M, Giangrande A. 2009. The mucus of *Sabella spallanzanii* (Annelida, Polychaeta): Its involvement in chemical defence and fertilization success. *Journal of Experimental Marine Biology and Ecology* 374(2):144-149.
- Storch V. 1988. The Ultrastructure of Polychaeta. I Integument. In W. Westheide and C.O. Hermans, editors. *Microfauna Marina* 4:13–36.

Truitt RE, Weber JH. 1981, Determination of complexing capacity of Fulvic acid for copper (II) and cadmium (II) by dialysis titration: *Anal. Chem.* 53:337–342.

Zorn ME, Muehlenbachs K, Gingras MK, Konhauser KO, Pemberton SG, Evoy R. 2007. Stable isotopic analysis reveals evidence for groundwater/sediment/animal interactions in a marginal marine setting: *PALAIOS* 22: 546-553.

Zhu Q, Aller R, Fan Y. 2006. Two-dimensional pH distributions and dynamics in bioturbated marine sediments. *Geochim. Cosmochim. Acta* 70:4933-4949.

CHAPTER IV

Controls on accretion of modern gypsum microbialites

4.1 Introduction

Microbial mats are complex ecosystems of interdependent microbial species typically growing on submerged solid substrata. The cells are embedded within a self-produced matrix of extracellular polymeric substance (EPS) composed largely of uronic acid-rich polysaccharides (Fazio et al., 1982, Sutherland 2001). The EPS matrix provides the community with a number of vital functions, including physical adherence, nutrient sequestration, and protection from adverse environmental factors. In addition, the EPS promotes mineral authigenesis, mostly carbonate, but silica and iron oxides can also occur (see Konhauser, 2007, for details). Biomineralization can occur in two ways. First, the chemical reactivity of the EPS facilitates surface adsorption reactions, and if solutions are sufficiently concentrated, those reactions may lead to mineral nucleation and growth. Second, various microbial metabolisms employed by the mat communities can alter the solution chemistry. For instance, anoxygenic photosynthesis can lead to the precipitation of ferric hydroxide, $\text{Fe}(\text{OH})_3$ (Pierson et al., 1999; Posth et al., 2008) or elemental sulfur (S^0) (van Gemerden, 1993; Stal, 2000), while anaerobic chemoheterotrophy (*e.g.*, sulfate reduction) can

increase solution alkalinity leading to calcite formation (Berner, 1975; Boudreau and Canfield, 1993; Decho et al., 2005; Visscher et al., 2005; Braissant, 2007). Crucially, if enough accommodation space in the subaqueous environment exists then the biomineralization reactions may lead to accretion of the mat to form high-relief structures above the sediment-water interface, also known as microbialites (Burne and Moore, 1987; Decho, 1990; Chafetz and Buczynski, 1992; Riding, 2000; Reid et al., 2000; Dupraz and Visscher, 2005; Decho 2009).

Modern microbialites occur in a range of depositional settings, as long as the ambient conditions preclude extensive grazing by animals (e.g., hypersaline, thermal, or turbulent). Hypersaline lagoons, in particular, are sites where the interaction amongst different microbial species results in optimal growth of microbialites. Interestingly, even within relatively close proximity, microbialites may display distinctive accretionary morphologies (i.e. stromatolitic and/or thrombolitic fabrics) which results from variations in the way different microbes interact within their local environments (Buczynski and Chafetz, 1993). For example, Feldman and McKenzie (1998) invoked changes in environmental conditions to explain the co-occurrence of stromatolites (microbialites with an internal structure of fine, more or less planar laminations) and thrombolites (microbialites characterised by a clotted internal structure) in the subtidal environments of Bahamas. Similarly, Planavsky and Ginsburg (2009) proposed that the co-occurrence of stromatolitic and thrombolitic fabrics in the Bahamian subtidal zones are a function of environmental influence, biologic and ecologic controls, and processes and rates of secondary cementation after metazoans boring. Meanwhile, others (e.g., Kennard and James, 1986; Chafetz and Buczynski, 1992) have suggested that the two microbialites reflect different microbial assemblages, although such a simplified distinction requires caution as thrombolites are not always constructed by coccus-dominated microbes, nor are stromatolites always constructed from filament-dominated benthic microbial communities (Burne and Moore, 1987).

Interest in modern microbialite formation also stems from the close morphological and textural similarities to their ancient analogues which

dominated the Earth's shallow seas for billions of years before the Phanerozoic. Yet, uncertainty exists regarding what microbes composed those ancient microbialites, and the microbial catalytic role during their lithification has since been obscured by post-depositional modifications that have obliterated most of their primary microbially induced, fabrics and their biochemical signatures (see Grotzinger and Knoll, 1999 for details). From the fragmentary and highly altered ancient stratigraphic record we hypothesize that during the Late Archean to Paleoproterozoic the shallow-marine carbonate sedimentation transition occurred largely as stromatolitic facies in evaporitic settings (Schopf et al., 1983; Grotzinger, 1989; Pope and Grotzinger, 2003). The presence of calcite pseudomorphs after gypsum in these ancient carbonate build-ups is rather common (Hofmann 1971; Hofmann et al., 1999; van Kranendonk, 2000; Hardie 2003, 2004), and although aragonite, instead of gypsum, has been proposed as the primary radial phase (Grotzinger 1989; Sumner and Grotzinger 2000, Pope and Grotzinger, 2003), multiple petrographic evidence (see Hardie 2003b for details) does not favour the alternate hypothesis.

Because primary gypsum textures are unlikely to persist through early diagenetic alterations, our best means of identifying the mechanisms by which subaqueous gypsum-dominated microbialites were replaced by carbonates is through the study of modern examples. Moreover, understanding the timing and process of calcification may be relevant to better assess the paleo-environmental conditions of Earth when these features were formed (*e.g.*, Kah et al., 2001,2004; Pope and Grotzinger, 2003). However, as far as we are aware, only a few examples of modern subaqueous gypsum-dominated microbialites have been documented. Accordingly, in this study, we present aqueous geochemistry, fine scale petrography, stable carbon and oxygen isotopes, and trace element analyses of modern, gypsum-rich, domal thrombolites to elucidate the early diagenetic controls on the lithification and growth of these subaqueous biological structures.

4.2 Geological context

4.2.1. Archipiélago Los Roques National Park, Venezuela

Located in the southern Caribbean Sea, ~150 km offshore of Venezuelan mainland, the Archipelago Los Roques (Fig. 4.1) encompasses an area approximately 1,250 km² with maximum and average water depths of 50 m and 5 m, respectively (Amend, 1992). The archipelago is made up of 42 cays distributed in an irregular-oval rimmed shelf. The rimmed shelf overlies an igneous-metamorphic terrain, the Caribbean Large Igneous Province (CLIP), estimated as Cretaceous in age (Ostos and Sisson, 2005). The basement rocks are exposed solely in Gran Roque Island (Fig. 4.1) where the ultramafic to mafic sequence is remarkably deformed and metamorphosed (to amphibolite facies); the igneous metamorphic complex is intruded by undeformed quartz–dioritic to pegmatitic rocks (Giunta *et al.*, 2002; Ostos and Sisson, 2005; Urbani, 2005); locally these rocks are pervasively phosphatised (Urbani, 2005).

The present day carbonate depositional system overlies a Pleistocene carbonate build-up which is exposed in some of the low-laying emerged islands. The inner shelf consists on a composite lagoonal setting partially enclosed by rimmed margins that range from reefal boundstone to grain banks to supratidal islands. These 'barriers' to open circulation are well developed along the eastern to southern margins of the shelf. The shelf interior locally exhibits semi-restricted conditions as the mesotidal region of the reef flat is frequently colonized by mangroves, which may partially confine the water bodies by increasing sedimentation rates. Behind these rimmed margins exist hypersaline lagoons and supratidal sabkhas, some of which are characterized by ephemeral and perennial surface brines (see below).

The climate in Los Roques is warm and humid, with average air temperatures of 28°C (up to 30°C at the time of study); daily humidity is around 80%; rainfall is 150 cm·yr⁻¹; and the prevailing trade winds blow from west to east at an average speed of 6 m/s (INPARQUES 2008). The thermal flux in Los Roques has been estimated (based on a daily average of 300 BTU·h⁻¹·ft⁻²) (Hudec and Sonnenfeld

1974) at $8.4 \text{ kW}\cdot\text{m}^{-2}\cdot\text{day}^{-1}$, thus evaporation rates on the perennial lagoons are high, $226 \text{ cm}\cdot\text{yr}^{-1}$ (as estimated by Sonnenfeld et al. 1977). The salinity on these sub-environments can reach values up to 140‰; meanwhile, salinity of the nearby shallow water shelf, as measured in situ was 39‰.

4.2.2. Laguna Pirata

The restricted lagoon under study, called Laguna Pirata ($\sim 11^{\circ}51'N$, $66^{\circ}45'W$), is an anchialine type basin closed by a permeable carbonate sand bar so the evaporatively concentrated water body is constantly fed by seepage seawater. This restricted lagoon has maximum and average depths of 1.65 and 0.55 m, respectively; the pond is density stratified and its hypolimnion consists of pinkish poorly oxygenated to sulfidic organic-rich slime (Fig. 4.2). In other perennial surface lagoons of Los Roques it has been reported that dense, hot brines are seasonally established at the bottom (Haduc and Sonnenfeld, 1974), this factor, however, has not yet been sufficiently studied in Pirata and it was estimated (February 2008) that the average temperature of the shallow surface hypersaline waters reach up to 3-5°C above the ambient daily air temperature.

Evaporation of the ponded water lowers a few centimetres the level of the lagoon, thereby subaerially exposing its margins to form a sabkha flat perimeter. The sabkha flat is characterized by encrusted white, finely crystalline crusts that are formed by evaporative pumping of the very shallow biofilm material. These crusts, which can be up to 2 cm thick, are polymineralic and contain halite, gypsum and carbonates. The crusts are dry and porous, and maybe easily eroded by ablation or partially dissolved by a summer shower.

Much of the subaqueous sedimentary substrate is colonized by microbial mats, and along the shallow rim of the lagoon, to a depth of approximately 1 m, there are regions containing lithified domal microbialites (Burne and Moore, 1987) of various sizes and densities. The actively growing structures are covered by a complex living microbial mat (up to 2 cm thick) (Figs 4.3, 4.4). The microbialites underlying the gelatinous outermost layer exhibit a clotted internal to crudely laminated fabric, similar to what is typically defined as thrombolites

(Aitken, 1967; Kennard & James, 1986; Shapiro, 2000). The microbialites grow only along the shallow margins of the lagoon (Fig. 4.3A, B). They vary in size from individual domal-shaped structures less than 10 cm in diameter to larger linear structures up to 5 m large, formed by the coalescence of smaller individual microbialites.

Accommodation space is an important boundary condition that defines the maximum potential growth-height of microbialites (cf. Andres and Reid, 2006). In Laguna Pirata the height of the thrombolites vary depending on the water depth in which they grow, as they appear to maintain a static level with the lagoon water level; as the water depth increases towards the centre of the lagoon, the presence of older coalesced thrombolites (some reaching up to 5 m in width x 1 m height) indicate that vertical accretion may be substituted by lateral growth (Fig. 4.3C).

In the deepest part of the lagoon, an organic-rich nodular sediment was retrieved using a long PVC dredging device. The sediment consists of a muddy organic-rich matrix, into which authigenic gypsum nodules (gypsooids) were embedded. The gypsum nodules reached 1 cm diameter, and at depth they form aggregates reminiscent of “chicken wire” anhydrite (Fig. 4.3G), as previously described in modern sabkha settings at the Persian Gulf (Demicco and Hardie, 1994).

4.3 Methods

4.3.1. Collection of microbialites specimens and in situ analysis

A total of 3 small lithified microbialites growing in the shallow part of the lagoon (water column depth between 0.15 to 0.45 m) were collected and picked out of water by hand. Two thrombolite specimens (~10 cm × 15 cm) (Fig. 4.3E) and a smaller, palm-sized specimen were collected and placed within polypropylene bags. In addition, the different layers of the microbial mats coating the specimens were carefully separated and collected. The organic mucilage and accompanying authigenic sediment infilling the deepest part of the lagoon were also sampled. In order to preserve the microorganisms for scanning and

transmission electron microscopy the organic samples were placed in sterile 0.5 ml Eppendorf PCR polypropylene tubes containing filtrated lagoon water and aqueous 2% glutaraldehyde to a final concentration of.

A rough estimation of the non-static vertical structure of the microbial mat associated to one of the thrombolite specimens was obtained through an *in situ* biogeochemical profile of a thrombolite growing with an overlying water deep of ~10 cm, as measured from its top surface (Fig. 4.3E). O₂ and H₂S microsensors (UniSense A/S, Denmark, 50 µm, response time, t₉₀, of ~0.3 s) were connected to a picoammeter via a micromanipulator mounted on a heavy solid stand. The O₂ microsensor was linearly calibrated by using picoampers readings of the microsensor in the air-saturated overlying water and in ascorbic acid (0.1 M, 0% O₂ saturation). Calibration of H₂S microsensor was done in a dilution series for sulfide standards buffered to the pH of the overlying water and with ionic strength of 0.5 M. Measurements were done in steps of 100 µm vertical depth intervals and recorded by using the computer software Profix (UniSense A/S, Denmark). Measurements were performed at temperatures about 30 °C.

4.3.2. Aqueous geochemistry

Water samples were collected by removing partially evaporated seawater directly from the lagoon by using a 60-mL sterile syringe. The syringe was then fitted with a 0.2 µm micropore filter through which water was expelled into metal-free polycarbonate screw cap sample bottles. Overlying water temperatures and pH values were measured immediately upon collection using a Ross (Orion) combination pH electrode. Total alkalinity (carbonate + bicarbonate content) of the samples was measured *in situ* by using acid titration. Filtered samples were collected in duplicate, with one set being treated with analytical grade nitric acid to a final concentration of 10% v/v for cation analysis and the other left untreated for anion analysis.

Quantitative analyses of SO₄²⁻ and Cl⁻ anions were performed on un-acidified samples using a Dionex DX600 Ion Chromatograph (IC); samples were diluted as appropriate before analysis to reduce salinity. For determination of major and

trace metal composition of Los Roques seawater, the samples were digested with HNO₃ (8N) and analyzed using a Perkin-Elmer AS-91. Accuracy and precision of the analytical protocol were verified through duplicate water analysis. The degree of saturation of dissolved mineral species in the lagoon water was determined using the geochemical speciation programs PHREEQC (Parkhurst and Appelo, 1999). The speciation results are presented in terms of the saturation index (SI) for each predicted mineral, where SI is defined by $SI = \log(IAP / K_{sp})$, being IAP and K_{sp} the ion activity product of the dissolved constituents and solubility product for the minerals considered, respectively.

4.3.3 Petrological and geochemical analysis

4.3.3.1 Thin-section petrography and electron microprobe analysis

At the University of Alberta two out of three of the thrombolite specimens collected were studied in detail. The specimens were left to dry at 30°C for about two weeks in a vacuum oven, followed by epoxy impregnation and sectioning. Polished thin and thick sections of the specimens were prepared for standard and fine scale (electron microprobe) microscopy, respectively; in addition the microbial mat coating one of the specimens was freeze-dried, epoxy-impregnated and thick sectioned for electron microprobe analysis. Standard transmitted light petrography and incident-blue-light excitation fluorescence (Dravis and Yurewicz, 1985) were used to determine mineralogical and textural relationships along the structure.

Electron probe analysis facilitates a better assessment of the mineralogy and chemical variations occurring in the constituent mineral phases through their definite elemental (Mg, Ca, S, Si, Fe, Na, Sr) distribution trends. A JEOL 8900 microprobe instrument equipped with five wavelength dispersive spectrometers was used to acquire backscattered electron images and elemental distribution maps of the samples. Natural minerals were employed as standards as described in Jarosewich (2002, and references therein). Instrument operating conditions and analytical procedures were: beam diameter, 40 μm; accelerating voltage, 15 kV

(30 kV for Sr); current, 15 nA; a matrix correction was used to calculate the concentrations. The data are presented 100% carbonate basis.

4.3.3.2 LA-ICP-MS

In situ trace element concentrations were obtained using a Perkin Elmer Elan6000 quadrupole-ICP-MS equipped with a New Wave Research UP-213 laser ablation system at the University of Alberta. Trace elements were determined on basal, middle, and uppermost crusts of one of the thrombolite specimen (94 laser spots) and in the authigenic carbonate mineral phases present in the microbial mat coating the same specimen (40 laser spots). Optimization of ICP-MS instrument parameters (RF power 1200 W, peak hopping acquisition, 50 ms dwell time) was achieved by ablating the NIST 612.

For quantitative trace element determinations, the standard and the microbialite samples were ablated using identical conditions with spot sizes of 40 μm , 5 Hz repetition rate and average fluency of 13 J/cm^2 . Quantitative results were obtained via the calibration of relative element sensitivities against the NIST 612 standard with analyses being normalized to $[\text{Ca}^{2+}]$ previously determined by electron microprobe analysis for the unknowns.

Data reduction and concentration determinations were obtained using the GLITTER[®] (New Wave Research) laser ablation software. Repeated analysis ($n = 6$) of the standard yielded relative standard deviations of between 0.01 and 0.5 % (2σ level) and detection limits between 0.02 ppm (*e.g.*, Zn, Cd, Cu) and 0.06 ppm (*e.g.*, Mg, Sc, Sr) for most elements (except for elements like, B, Yb, Lu).

4.3.3.3 Stable Isotopes analysis

In order to evaluate isotopic shifts within the thrombolite, nine subsamples from different calcified crusts of one of the specimen were subsampled. In addition, 12 mg of authigenic carbonate grains were carefully picked up from the biofilm material. The authigenic nature of these grains was defined through examination of its distinctive morphological and optical features as evidenced both, by reflected light and epifluorescence microscopy.

The subsamples were treated during 48 hours with H₂O₂ (15%) to remove superficial organic matter, then rinsed three times using 18.2 mΩ H₂O and dried overnight in a vacuum oven at 30°C. The isotopic values were determined directly by evacuating samples and releasing (under vacuum) the inorganic carbon as CO₂ by addition of concentrated analytical grade phosphoric acid (McCrea, 1950). The CO₂ was separated cryogenically from the released gases for subsequent analysis on the mass spectrometer.

The isotope ratios of the solid carbonates were determined on a Finnigan Mat 252 Mass Spectrometer equipped with both multi-port and continuous flow inlets at the University of Alberta. The results are given in the conventional δ-notation expressed in per mil, where: $\delta (\text{Sample}) = (R_{\text{sample}}/R_{\text{Standard}}) - 1 \cdot 10^3$, and R is the ¹⁸O/¹⁶O or ¹³C/¹²C ratio. δ-values are reported relative to CO₂ derived from a carbonate working standard and then referred to the V-PDB (Vienna- Pee Dee Belemnite) standard, using αCO₂ in phosphoric acid of 1.045.

4.3.3.4 Scanning and Transmission Electron Microscopy

By using scanning electron microscopy we visualize the microstructure of the two types of organic EPS matrices existing in Laguna Pirata and their relationship with dominant authigenic phases present in (1) the coherent layered mat in the shallow lagoon linked with the growing thrombolitic structures; and (2) the non-layered biofilm associated with gypsooids authigenesis.

SEM analyses of the biofilm samples collected in Laguna Pirata were performed via low-temperature (Cryo-SEM) and critical point drying methods, both using a JEOL 6301F (Field Emission Gun Scanning Electron Microscope). Semi-quantitative elemental analyses were conducted through a liquid nitrogen cooled Li drifted silicon energy dispersive X-ray (EDX) detector with a Norvar X-ray analysis system manufactured by PGT. Semi-quantitative elemental standard-less analyses were conducted with measurement times of 30s each at 20eV. Small pieces broken from one of the thrombolite specimens were mounted on stubs, gold sputter coated, using a Nanotech SEM Prep 2 DC. The same SEM instrument described above was used for petrographic analyses. A Philips / FEI

(Morgani) Transmission Electron Microscope with CCD camera (TEM-CCD) was used for analysis of ultrathin sections of the microbial mat at an operation voltage of 80 kV.

For Cryo-SEM, millimetre size samples were rapidly frozen by immersion in liquid nitrogen (-200°C), then introduced in the cryo-chamber of the microscope (Emitek K1250 cryogenic system) where they were fractured at -180°C, superficially sublimated at -90 °C, gold coated at -180 °C, and then introduced in the refrigerated column of the JEOL 6301F equipment to be observed at -180°C. The sample preparation protocol for critical point drying and TEM is slightly similar. Selected biofilm sub-samples were extracted from the preserving glutaraldehyde solution and placed in 1.5 mL new Eppendorf tubes. The samples were then rinsed four times during 15 minutes in 18 MΩ-cm water. Following this, they were passed to new Eppendorf containers, dehydrated by using a series of ethanol solutions, with increasing concentrations, from 10 to 90% in 20% increments (15 minutes each rinse), with three final rinses in 100% ethanol (15 minutes each, and the final one overnight). Final substitution with liquid CO₂ and the drying run were carried out inside a Bal-Tec CPD030 critical point dryer. After drying, samples were placed on aluminum SEM samples holder with a silver paint, and carbon/gold coated prior to observation.

Samples for TEM analysis were prepared for ultrathin sectioning by embedding in Spurr epoxy resin, with an intermediate propylene oxide bath. The resin blocs were finally left to harden in a 60° C oven for 3 days. Ultrathin sections were made using a diamond knife mounted on a Reichert ultramicrotome and placed on copper TEM grids. To increase contrast, some grids were stained with uranyl acetate (20 min) and lead citrate (7 min). Some grids were also observed unstained to establish evidence of minerals/ microorganisms interactions.

4.4 Results

4.4.1 Lagoon water chemistry

The surface waters in the study site are naturally alkaline, with measured pH values ranging from 8.7 to 9.4. At the time of the field study (February 2008) the water temperature fluctuated between 28 and 35°C and the average salinity was around 90‰, reaching up to 110 ‰ in the adjacent sabkha flat (Fig. 4.3D). Other relevant chemical features of the lagoon water are shown in Table 1.

In terms of major ion chemistry Laguna Pirata waters were relatively enriched in Mg^{2+} as compared to normal seawater. With a measured molar Mg/Ca ratio of 6.1, it is thermodynamically predicted that the lagoon hypersaline waters are oversaturated with respect to dolomite (SI= 3.8); calcite (SI= 1.4), and aragonite (SI= 1.28), whereas, in the surface waters, gypsum, so far the most abundant mineral phase at Laguna Pirata, was found slightly undersaturated (SI= -0.29). The saturation state of the near surface water body with respect to gypsum may be affected by temperature, oxygenation, mixing (Last and Schweyen, 1984) and alkalinity (Thompson and Ferris, 1990).

The enrichment factors for trace metals in the lagoon water (respect the concentration of Los Roques mean seawater) are shown in Figure 4.5. The surface waters from Laguna Pirata are slightly enriched in Co, Fe, Ni, Mn; conservative respect to Cu, Cr, Mo, U and V; and depleted in Zn, Y, Zr, Nb and Sn.

4.4.2 Geobiology of the microbial mats

4.4.2.1 The thrombolite constructing mat

Along the shallow rim of the lagoon, the microbial mats show the typical stratification associated with oxygen diffusion and light penetration (Revsbech et al., 1983; van Gemerden, 1993). These factors generate the development of distinct niches that are efficiently utilized by phototrophic members, which due to their distinctive chlorophyll pigments are visually manifest as multicoloured layers (i.e., Airs and Keely, 2003; Stomp et al., 2007).

The uppermost layer, which extends up to 4 mm in depth, has a yellowish- to greenish colour and consists on microbial community dominated by cyanobacteria (i.e., *Oscillatoria* sp., *Microcoleus* sp.) and algae (mostly diatoms and green filamentous algae) (Fig. 4.6). During daylight, this layer is responsible of an

increase of the partial pressure of oxygen from 0.45 to 1.05 atm, as measured *in situ* with microelectrodes.

A green layer containing abundant purple aggregates occurs from 4 to 10 mm, its layer contains a filamentous fine lamina of white elemental sulfur. Microsensing data shows that this layer coincides with a zone where steep opposing gradients of O₂ and H₂S occur (Fig. 4.4). The elemental sulfur lamina might be indicative of biological HS⁻ oxidation (i.e., van Gemerden 1993) (Fig. 4.4A). Fine scale biological microscopy (Fig. 4.6) reveals that this layer contains a high microbial density and a rich variety of organisms, ranging from filamentous cyanophytes, including a sulfide tolerant *Spirulina*-like cyanobacterium (Fig. 4.6D), clump-forming, non-identified microcolonies of rod-shaped (~3-5 µm diameter) cells enclosed by multi-laminate sheaths; isolated *Beggiatoa*-like cells (Fig. 4.7D, left cell), frequently exhibiting intracellular sulfur mineralization, are also present.

As revealed by a peak in the partial pressure of H₂S, below the photosynthetic zone, at depths >10-12 mm, the biofilm abruptly becomes sulfidic reflecting ongoing sulfate reduction (Fig. 4.4). During daylight the top of the bottommost layer, attached to the surface of the lithified thrombolites, coincides with the lower position of this dynamic sulfidic zone, which during the night shifts to an upper position within the mat. Fine scale microscopy of this layer reveals that it is made up of rod-shaped bacteria. The morphology of some of the cells resembles those which in the overlying layer are ensheathed in thick EPS slimes (cf. Fig. 4.7C,G). Because the microbialites are found only in the shallow margins of the lagoon the availability of light may play an important control on their growth by sustaining the activity of photoautotrophic organisms; however, as illustrated by Fig. 4.7, much of the microbial diversity at the lagoon margins remains to be studied.

4.4.2.2 *The gypsooids-supporting mat*

By contrast, the microbial mat developed in the deepest lagoon (1.0 - 1.6 m depth) is characterized by a less-complex physical structure lacking the distinctive multi-coloured layers typifying its shallower counterpart. It is a soft gelatinous

mat of about 10 cm thick supporting abundant gypsooids (see § 4.4.3.2). A centimetre-scale layer made of nodular gypsum aggregates sets apart a pinkish non cohesive layer at the top, from a pale orange, more coherent, layer at the base (Fig. 4.3G). In the bottom of the mat the organic-supported sediment exhibits a chicken wire texture where gypsooids are more compactly distributed (Fig. 4.3G).

As noticed in other microbial mats systems developed at hypersaline settings (e.g., Guerrero Negro, Des Marais, 2003) the stratification of the lagoon waters affects the composition and diversity of microbial communities (e.g., Gerdes et al., 2000) and the mat developed in the hypolimnion of Laguna Pirata has a low microbial diversity dominated by sulfur dependant cocci bacteria (~2-4 µm diameter) (Fig. 4.7H, I). The clump-forming cells may occur singly or in hemispheroidal cell pairs forming irregularly to ordered mucilage-enclosed colonies (2-8, or more cells), which are supported by the less-cohesive slime that also serve as matrix for the growth of authigenic gypsum (Figs. 4.6F, 4.7H); intracellular mineralization is generally observed. From their ultrastructural features those cells may have affinities with the Chromatiaceae family (probably *Thiocapsa* sp.) (Fig. 4.7H). Bacterial cell exhibiting similar morphologies were also noticed in the suboxic layer of the thrombolite-constructing mat (4.7D), but therein they form less denser blooms than those found in the gypsooids supporting mat (Fig. 4.6 F)

4.4.3 Biofilm mineral relationships

4.4.3.1 Allochemicals

Both trapped and precipitated sediments were analyzed by fine scale microscopy. In the first instance, wind or storm derived particles were found randomly dispersed within the biofilm developed in the shallow rim of the lagoon. The allochemical fraction consists mostly of millimetre-scale angular fragments of the calcareous algae *Halimeda* sp.; other extraclast also present in minor proportions are intertidal ooids and unidentified calcareous particles of biogenic origin; bioclast other than the green algae flakes rarely exceed several hundreds of micrometres in diameter.

Backscattered and X- ray elemental maps (Fig. 4.8) shows that the aeolically-transported particles trapped by the mat are often microbored. These features, having a diameter of 5 to 10 μm (Fig. 4.8), may represent *in situ* biogeochemical dissolution produced by endolithic microbes (e.g., Kobluk and Risk, 1977). Micrite may accumulate internally, between already deposited particles or within intragranular cavities, microbores may be filled by Mg-micrite (Fig. 4.8). The microboring process would result in obliteration of the original grain boundaries to form composite grains exhibiting Mg-rich micritized rims (e.g., Reid and Macintyre, 2000) (Fig.4.8).

4.4.3.2 Authigenics within the mat

The authigenic crystallite size as observed in a random sample from the thrombolite-constructing mat can vary from a hundreds of nanometres to a few hundreds of micrometers. Cryo-scanning electron microscopy coupled with EDAX analyses were used to characterize the textures of authigenic precipitates and their primary relationships with the organic matrix. Accordingly, the precipitates from shallow rim's mat consist of: (1) micrometer scale aragonite needles, usually forming peloidal aggregates up to 400 μm in diameter; (2) fine ellipsoidal aggregates formed by blocky calcite crystals; (3) spheroidal forms of Mg-calcite, with a diameter ranging from 5 μm up to 10 μm , that may or may not be calcified bacterial cells and their sheaths. Such nanospheres form in the initial phase of carbonate precipitation and their subsequent clustering and/or coalescence with further overgrowth forms the carbonate macrostructure of the structure (e.g., Lepot et al., 2008, and references therein); and (4) spherical Ca-phosphate particles up to 20 μm diameter which are found encased by a calcified Mg-rich sheath exhibiting nanometre-scale dwarf forms resembling the so-called nannobacteria (Folk, 1993) (Fig.4.9F).

In the deep-water mat, authigenic precipitation consists of gypsum crystals exhibiting prismatic and equant morphologies which are growth-supported by the organic gelatinous sludge; individual gypsum crystals can be found 'floating' as micrometer scale crystals, with sizes ranging from 50 to 200 μm , or as

polycrystalline aggregates that forms micrometre-scale grains described as gypsooids (Fig. 4.10A,B). In addition, delicate gypsum rosettes were found within the intracrystalline spaces of gypsum (Fig. 4.10E). As these twinned polycrystalline aggregates were observed coated by EPS it is thought that their growth might be favoured by the polysaccharide-rich organic matrix (e.g., Cody and Cody, 1988). SEM analysis also showed that aragonite may locally grow subordinate to gypsum as delicate needlemesh works embedded in cracks parallel to the {010} cleavage of gypsum; these aragonite aggregates exhibit a radiating arrangement (Fig. 4.10C, F).

4.4.4 Mesostructural features of the thrombolites

Internally, the thrombolitic fabric from Laguna Pirata has two framework components. The first consists of isolated discontinuous millimetre-thick convex upward zones, exhibiting a crudely laminar texture consisting in carbonate cements (Fig. 4.11). These are more conspicuous in the bottom of these structures, which frequently consists of continuous densely cemented laminations that represent the surface of initiation of accretion. The laminar densely cemented zones are intergraded with the other framework element consisting of massive intervals consisting on gypsum grains bound together by microcrystalline cements; within the gypsum rich zone there are areas exhibiting a discontinuous crudely laminar fabric.

The continuity of the primary framework within these thrombolites is mostly break up by numerous cavities up to a few centimetres wide that yields together an overall porosity estimated at around 40% (Fig. 4.3). The larger vugs usually lack internal sediment, but their boundaries often show a pervasive cementation, which sustain the structural integrity of the structure (see § 4.4.5). Although difficult to prove, it is plausible that these cavities were formed by entrapment of biomass material followed by its degradation and mineralization to CO₂ or CH₄ (?); it is know that in organic-rich evaporitic settings many methanogens often develop a symbiotic relationship with strains of *Desulfovibrio* (Sonnenfeld, 1984, p. 181). Alternatively, the less labile material may have been grazed upon by

heteropterids and other animals which have developed a physiological ability to withstand elevated sulfide levels (Gingras et al., unpublished).

4.4.5 Microtextural and mineralogical features

Microtexture refers to the nature and patterns in distribution of the microscopic components making up a microbialite (size and composition of carbonate crystals, organic matter, and discrete microfossils) (e.g. Turner et al., 2000); though in this work this term applies also to the microscopic composition, mineral association and mode of aggregation of crystal in the studied thrombolites. In thin-section the specimens consist of gypsum crystals and its pseudomorphs, supported by micrite/microspar cements associated to remnant organic material, both infilling intragranular and local intergranular-dissolution cavities in gypsum (Fig. 4.11).

The basal zones are predominately composed of infra-millimetre laminae of micritic calcite; the density of gypsum crystals increase upwards from isolated crystals in the base to densely interlocking crystals at the top. Porosity can reach up to 35 to 40% in some of the thin sections, decreasing to nearly 2% in the internally laminated zones. Patches of micrite are commonly found towards the densely interlocking gypsum dominated zones (Fig. 4.11A, 4.12), in some of gypsum lattices intracrystalline micrite has been observed (Fig. 4.11A, E). As described above, fenestral and intercrystalline void spaces are occluded by microcrystalline precipitates, which when associated to gypsum alter the depositional features to form a clotted fabric (i.e., Kennard and James, 1986; Turner et al., 2000) that binds together the gypsum crystals (Fig. 4.11B,C).

The amount of carbonate as seen in thin sections ranges from 5% to as much as 35%, of which 5 to 20% is micrite/microspar cements and 15 to 25% is aragonite; while primary gypsum comprises more than 40% of the bulk mineralogy, but it shows often a pervasive replacement by aragonite, occurring in association with elemental sulfur, the last can locally rich up to 5% (as observed through electron probe imagery); halite (as determined by XRD, data not shown)

might also be present within the thrombolites in low proportions. The average size of gypsum crystals is 250-400 μm in length but crystals up to ~ 600 μm long were found; morphologically gypsum may have: (1) tabular and equant forms; (2) lenticular to acicular crystal forms. The crystals are often internally poikilotopic (Figs. 4.10, 4.11).

4.4.5.1 *Gypsum pseudomorphs*

There is evidence for biochemical dissolution of gypsum as suggested by their corroded boundaries. Aragonite occurs as a pervasive replacement phase that often mimics the crystalline pattern of gypsum –i.e., it is a pseudomorph –. Commonly, these mineral aggregates are partially coated by EPS. Microprobe analyses show that these crystals are aragonite. Traces of elemental sulfur (see below) are often associated to pseudomorphic aragonite, in the organic matrix; accumulations of Mg were also observed (Fig. 4.13). Aragonite replacing gypsum often occur along the crystal boundaries and cleavage/fracture planes of the primary sulfate and aragonite might protrude the fibrous gypsum grains (Fig. 4.11F); but in general the interface between gypsum and aragonite occur in nearly orthogonal angle to the dissolution fronts along gypsum crystals (Fig. 4.11F), from this it can be inferred that aragonite formation occurs immediately after dissolution of gypsum (e.g., Peckman et al., 1999).

The Sr content in the primary sulfate crystals (n=23) was 995 ± 153 ppm. No inclusion treatment or corrections for celestite were conducted, but celestite does not account for more than 0.2% of the bulk mineralogy, and only crystals previously identified as gypsum in the microprobe, were analyzed by LA-ICP-MS, so the Sr values obtained corresponded exclusively to the gypsum lattices. As determined by LA-ICP-MS, the strontium content of secondary aragonite (after gypsum) averaged $4,763 \pm 1,460$ ppm (n=11). This indicates that aragonite crystal precipitation accompanying gypsum dissolution have a relatively rich source of Sr other than gypsum; the partition coefficient of Sr (D_{Sr}) on the authigenic carbonates formed in the mat are consistent with a general enrichment in Sr from the evaporated lagoon water (Fig. 4.15).

4.4.5.3 Micrite/ microspar matrix

Backscatter electron images and Mg and Ca distribution maps reveal that the matrix consists of 2 to 5 μm sized aragonite/calcite. The micrite/microspar cement form patches, or clots, of variable density that exhibit a dull luminescence under blue light excitation (epifluorescence). There are scattered sub-millimetre scale laminar cements infilling fenestral spaces, as observed by secondary BS microscopy consisting of dark and clear alternations; X-ray elemental analyses reveal that the alternation is largely defined by a relative abundance of magnesium (Fig. 4.11F, 4.12).

From the textural relationships between gypsum crystals and micritic matrix it seems that in a first stage Mg micrite and aragonite were formed in association with the EPS embedding the primary sulfate mineral (Fig. 4.10), as the EPS undergoes bacterial decomposition, it drive neomorphic inversion of aragonite forming intracrystalline patches of microspar within the micritic matrix. Isolated filamentous and coccoid shapes, of approximately 2 μm diameter (Fig. 4.11B), appear as mineralized bacteria-like fossils remains often in close association with the clotted micrite, previously described

4.4.5.4 Elemental Sulfur

Finally, the previous described mineral phases are frequently associated with the accumulation of elemental sulfur (Fig. 4.13A, B), whose relative abundance with respect to the bulk mineralogy is often less than 1% but can locally reach up to 3%; frequently appearing in association with aragonite replacing gypsum.

4.4.6 Carbon and oxygen stable isotopes composition

Table 4.2 shows the values of carbon and oxygen isotopes (V-PDB), together with the MgCO_3 content (weight %) of authigenic carbonates and cements growing at the microbial mat and within the thrombolites.

4.4.6.1 Carbon Isotopes

In Figure 4.13, the carbon isotopic composition of cements from the thrombolite under examination and that of authigenic carbonates precipitated in the unlithified microbial mat coating the structures is shown. In general, in these thrombolites ^{13}C have an average value of $-5.4 \pm 2.5\text{‰}$ (V-PDB), ranging within the typical values of organogenic carbonates, as described by Compton (1988). A detailed comparison of the average $\delta^{13}\text{C}_{\text{inorg}}$ values of the authigenic carbonates from the mat and the cements stabilizing the thrombolites shows that fractionation occur in the mat/structure interface, with heavier values, $+1.1\text{‰}$, observed in the external crust of the thrombolite (Table 4.2). By contrast, the $\delta^{13}\text{C}_{\text{inorg}}$ values of the subsamples taken in the centre of the specimen under examination are about 2.8‰ lighter than the carbonate cements from the interface (Fig.4.13). The decrease in ^{13}C -content towards the centre may result from incorporation of ^{12}C released by a more active heterotrophy of organic matter within the thrombolite. Conversely, carbon isotopes from cements at the basal part of the specimen are about 2.7‰ heavier than those of the thrombolite interface, suggesting that in the more densely cemented zones the thrombolite isotopic system may incorporate, in a greater extent, heavier inorganic carbon dissolved in the pore waters (e.g. Nissenbaum et al., 1972).

By comparing the average $\delta^{13}\text{C}_{\text{inorg}}$ from the mat ($\delta^{13}\text{C} = -6.1 \pm 1.0\text{‰}$), the average of early diagenetic cements, $\delta^{13}\text{C} = -5.2 \pm 1.0\text{‰}$ and the average $\delta^{13}\text{C}$ obtained for *Halimeda* sp. flakes, $\delta^{13}\text{C} = +2.1 \pm 0.25 \text{‰}$, it is possible to define the Δ -value of about $-6.5 \pm 1.0\text{‰}$ between the allochem and authigenic carbonate phases currently being deposited in Laguna Pirata. The ^{13}C content of calcareous algae usually reflects significant metabolic effects and thus may exhibit a wider range of $\delta^{13}\text{C}$ values (Lee & Carpenter 2001), this variability, however, was not observed in the carbonates phases of the thrombolite, whether allochemical or authigenic (Table 4.2), what suggest that the allochem fraction might isotopically re-equilibrated within the mat. The carbon isotopic composition of the purple layer ($\delta^{13}\text{C}_{\text{org}}$) was studied by CG-ICP-MS; the value obtained, $-15.6 \pm 0.9\text{‰}$ (V-PDB), allow the magnitude of the isotopic shift during organic to inorganic

carbon fixation, $\Delta\delta^{13}\text{C}_{\text{Org-Inorg}}$, to be estimated in about 10‰. This fractionation factor is consistent with preferential removal of ^{12}C by the microbial biomass coating the structure.

There is no relation between the carbon and oxygen isotopes (Fig. 4.13B); from the lack of correlation between the two isotopes it is clear that different processes are involved in carbon and oxygen fractionation. Conversely, a positive correlation between $\delta^{13}\text{C}$ and the MgCO_3 contents in the cements in the specimen under examination (Fig. 4.13C), the relatively good correlation suggests that the mechanism responsible of ^{13}C enrichment in depth within the structure could be related to the process leading to magnesium assimilation.

4.4.6.2 Oxygen isotopes

The mean $\delta^{18}\text{O}_{\text{PDB}}$ value of the thrombolite cements is comparable with the value of the carbonate phases precipitated on the mat (Table 4.2, Fig. 4.13), the values contrast with the $\delta^{18}\text{O}_{\text{PDB}}$ of the aeolically transported *Halimeda* sp. flakes fragments, averaging $2.2 \pm 0.13\text{‰}$. The fractionation factor between calcite and water for O isotopes is known to vary with temperature; according to Kim and O'Neil (1997) in the temperature range between 0 and 40°C the precipitation rate has essentially no effect on the measured calcite-water oxygen fractionation (Chacko et al., 2001). As temperature in excess of 40°C are unlikely to occur subaqueously in Laguna Pirata, except perhaps in the sabkha flat, then the oxygen isotopic composition of the water from which the calcite cements of the subaqueous structures precipitated can be calculated.

The temperature at which authigenic calcite precipitated was probably close to the mean lagoon water temperature. From the temperature range measured in situ, [28, 35] °C, and by using the equation of Friedman and O'Neil (1977), with a fractionation factor calculated as described in Faure (1991, §17.2), then the $\delta^{18}\text{O}_w(\text{SMOW})$ of the lagoon seawater yields values between +1.9‰ and +4.0‰. Owing the relative stability of climate in Los Roques, the range of $\delta^{18}\text{O}_w$ values obtained can be considered a good approximation to the mean O isotopic composition of the shallow body of evaporated seawater in the lagoon. Kinetic

effects during evaporation and exchange of water between liquid and vapour phases, however, limits the extent of heavy isotope enrichment during evaporation (Craig et al., 1963), this limitation is common in humid evaporating settings as Los Roques and has been widely observed elsewhere (e.g., Lloyd, 1966; Major *et al.*, 1992). There is, however, insufficient data to fully characterize shorter term isotopic changes during storm events that would promote instantaneous dissolution-precipitation reactions.

The narrow range of oxygen isotopic values (V-PDB) of the carbonates precipitated in Laguna Pirata ($\delta^{18}\text{O} = -0.4 \pm 0.14\text{‰}$ in cements, and $-0.9 \pm 0.25\text{‰}$ in the mat's authigenics) are indicative of isotopic equilibrium with the lagoon evaporated seawater. The $\delta^{18}\text{O}$ values in allochems, $+2.2 \pm 0.13\text{‰}$, in contrast with their carbon isotopic signatures, are relatively stable and should reflect values usually close to the predicted for equilibrium (see Lee and Carpenter, 2001, for details). This is relevant as the $\delta^{18}\text{O}_{\text{PDB}}$ values of *Halimeda* sp. flakes can be considered as the baseline for the $\delta^{18}\text{O}$ value of a carbonate precipitated in equilibrium with Los Roques's seawater; clearly the evaporation rates of Laguna Pirata exceed its seawater influx most of the year and cementation occurs mostly under hypersaline conditions, thus, dissolution/ precipitation effects related to storm events seems unimportant. Moreover, the isotopic difference observed between *Halimeda* sp. and the cements of the thrombolites from Laguna Pirata suggests that microbially induced precipitation may exceeds trapping and neomorphism of allochemicals as the actual mechanism of stabilization.

4.4.7 Trace elements composition of carbonate cements

Cations, minor elements, and trace elements may substitute for Ca^{2+} in the CaCO_3 lattice in the following manner: (1) by direct substitution of the major element for the foreign element; (2) by interstitial lattice-position substitution; (3) by adsorption on a crystal surface, and; (4) by substitution involving crystal defects (Brand 1994). Table 4.3 shows the enrichment factors of some trace metals in cements from the lithified microbialites as compared with the authigenic carbonates within the associated biofilms. In the thrombolites there are striking

similarities between the trace metal patterns of the carbonate cements and the trends exhibited by the authigenic carbonates within the mat (Fig. 4.15), suggesting that a common mechanism of trace element incorporation operating in both the lithified and unlithified zones of these structures. It is interesting that the cements are slightly enriched (up to 2x) over the biofilm carbonates in Li, Na, V, Cr, Fe, and Pb. The enrichment factors are higher for V, Co, Sb, U (2x to 4x), while Cu and Mo concentrations are 7x and 12x higher in cements. On the other hand, Ni and Zr exhibit a conservative behaviour, and no enrichment seems apparent in the lithified thrombolite.

4.5 Discussion

4.5.1 Microbial involvement (?) in gypsum accumulation

Direct evidence on microbially induced gypsum precipitation has been elusive. However, oxygenic phototrophs that can photolyze either H₂O or H₂S may to some extent contribute to gypsum precipitation as suggested by accumulation of the mineral on the cell wall of the unicellular cyanobacterium *Synechococcus* sp. (Thompson and Ferris, 1990). Gypsum is stable only if SRB are inhibited by the availability of O₂ (Sonnenfeld, 1984, p. 181). From the abundance of gypsum and the deficiency of carbonates in the authigenic phases currently forming in the hypolimnion, it can be inferred that the bottom waters contain sufficiently high sulfide concentrations and oxygen (or nitrate) levels as to inhibit the growth of sulfate reducers, thus, in the deepest part of the lagoon the favoured deposition of gypsum indicates a frequent mixing of the water masses; perhaps by convective currents (Sonnenfeld, 1984) that bring sulfidic bottom waters to the surface and oxygen-rich waters to the bottom. Alternately, seepage influx, as described by Babel (2007), may increase the concentration of oxygen in the bottom waters to levels that actually prevent SRB to become a more stable community in the deepest Laguna Pirata.

In the hypolimnion, oxygen availability might be cyclic as occurred in the perimediterranean Messinian basins (e.g., Rouchy and Monty, 1979; Babel,

2007). In the stage of oxygen limitation, consumption and production rates of oxygen and sulfide probably equalize, then microbial sulfide oxidation yields thiosulfates, polysulfides, and polythionates (van Gernerden, 1993; Jørgensen 1994). Although SRB can flourish locally in the hypolimnion, they are subordinate to microniches in the surface of gypsum crystal growing in the organic matrix material (dominated by sulfide oxidizers), in such microniches they drive a non-pervasive and localized replacement of gypsum by aragonite. When oxygen is replenished, there should be a dramatic decrease in the activity and population of sulfate reducers and then a sulfide limitation, so thiosulfates and polysulfides can be further oxidized to sulfate (van den Ende and van Gernerden, 1993; Visscher and Stolz, 2005), which rapidly reacts with dissolved Ca^{2+} leading to supersaturation with respect to gypsum (Fig. 4.17). In contrast, in the shallow rim the process might be controlled by facultative photo-synthesizers that in deep supply oxygen for conversion of H_2S to SO_4^{2-} , allowing gypsum precipitation, in such microenvironments even if the saturation index is not theoretically reached, as observed by the SI with respect to gypsum of the shallow waters. This because the chemical equilibrium modeling approach here implemented do not correct completely all interactions among Ca^{2+} , Mg^{2+} , SO_4^{2-} , OH^- , HCO_3^- , Cl^- , Na^+ , K^+ and other ions in pore water solution, which are in equilibrium with CO_2 both, from the atmosphere and photosynthetically-produced within the coating mat.

The question of whether microbial degradation of EPS is directly involved in the accumulation of gypsum deserves to be explored in depth and Laguna Pirata is a natural laboratory to evaluate such process. The absence of lithifying microbial mats in the depth lagoon and the low proportion of carbonate minerals therein underscore the stabilization function exerted by synergetic interactions between aerobic and anaerobic communities at the shallow rim of Laguna Pirata, leading to the accretion and lithification of the thrombolitic fabrics herein examined. Further field observations and additional carbon and sulfur isotope data would constrain the nature of the sulfate source in Laguna Pirata in order to identify and quantify the major biological and abiotic processes contributing to sulfur cycling in this understudied lagoonal system.

4.5.2 Microbially-mediated replacement of gypsum

Gypsum dissolution rates are known to proceed slower than calcite precipitation rates, thus, for a pseudomorphic replacement of gypsum to occur the dissolution of the primary crystals must be accompanied by a simultaneous crystallization of the replacing carbonate phase (Fernández Díaz et al., 2009 and references therein). Two different mechanisms have been proposed to explain the pseudomorphic replacement of gypsum by aragonite. The first one is early diagenetic and involves the coupled activity of sulfate reducers and anaerobic sulfide oxidizers thus it is often accompanied by secondary accumulations of elemental sulfur (Visscher and Stolz, 2005; Kah, 2001; Vogel, 2009). The second mechanism is post-depositional, and occurs under the influence of carbonate-rich meteoric waters (Pierre and Rouchy, 1988). In both cases, pseudomorphs of calcite or aragonite after gypsum, as well as gypsum relicts occur. The degree of faithfulness of the pseudomorphs formed after gypsum, is dependant of the carbonate concentration; when the carbonate concentration is high, the nucleation of the replacing carbonate occurs immediately, and would preserve the volumes and shapes of the primary crystals (Fernández Díaz et al., 2009).

It has long been known that precipitation and dissolution of gypsum is largely affected by the concentration, amount and pH, of the proteolytic solutions and the composition of organic macromolecules present (Sonnenfeld 1984, and references therein), which may inhibit or substantially affect the common crystal habits of gypsum to produce substantial deviations (Cody and Cody, 1988, Doğan et al., 2004; Vogel et al., 2008). Thompson and Ferris (1990) have suggested that bacterial alkalisation of their microenvironment and the associated oversaturation with respect to calcite can be linked with a simultaneous drop in the saturation state of gypsum, while Kah et al., 2001 noticed that dissolution of gypsum may results from BSR which through a direct reductive attack on its sulfate moiety induce calcite precipitation.

Ammonium and carboxyl biopolymers, are well know kinetic inhibitors of gypsum. Since ammonium is a by-product generated during degradation of

proteins by SRB then the previous observations can be reconciled by ammonification resulting from protein degradation (Castanier, 1999; Wright and Wacey, 2005), which may enhance gypsum dissolution rates (Sonnenfeld, 1984) while increasing pH thus favouring Ca carbonate precipitation (Fig. 4.17). Conversely, the inhibition effect of carboxylated oligomers in EPS prevent the formation of crystals larger than the critical size (preventing gypsum nucleation) in an EPS matrix that might be saturated in both, SO_4 and Ca ions. Surface modification of those crystals which do form causes them to distort as they grow. This distortion can slow and actually stop the growth of crystals (Amjad, 1996).

4.5.2.1 Native sulfur association

In Laguna Pirata elemental sulfur is often associated to gypsum and aragonite (Fig. 4.13). As previously stated, elemental sulfur species often accompany microbially catalyzed replacement of gypsum aragonite, and S^0 can be interpreted as intermediates of redox sulfur cycling by microbial sulfate reduction coupled to various sulfide oxidation processes (Vogel et al., 2010). In order to obtain S^0 as a product of the bacterially mediated reaction that yields pseudomorphic aragonite, sulfate reduction must be accompanied by sulfide oxidation, and the last should be forced in the direction of sulfur production by high sulfide loads (Stefess et al., 1996), thus H_2S can be oxidized to produce intra and extracellular sulfur deposits (Fig. 4.17). Photosynthetic sulfur bacteria form low molecular weight organic compounds, which are in turn utilized as a carbon source by associated heterotrophs (Burdige and Gardner, 1998; Arnosti and Holmer, 1999), the interplay sustains the continuity of redox reactions producing carbonates from primary gypsum. Significant amounts of S^0 accompanying carbonate precipitation can also be produced by SRB with the involvement of facultative SOB in the absence of oxygen (Fig. 4.17) if a buffer zone consisting in redox sensitive intermediate species is present (e.g., Kaufman et al., 1996) the resulting Me^{2+} sulfate may be reoxidized chemically or biologically within the thrombolites.

4.5.2.2 Mg association

Magnesium X-ray maps reveal that the less labile organic matter trapped during accretion has local Mg^{2+} accumulations (Fig. 4.16), elevated Mg/Ca ratios within the thrombolites may be crucial for the preferential formation of aragonite over calcite (Peckman et al., 1999), and if SRB are partially inhibited, then alkalinity cannot reach values as to promote an steady state nucleation of Mg calcite (i.e., Wright and Wacey, 2005). Bacterial obliteration of gypsum may also lead to low Mg calcite, which is ^{12}C enriched, or magnesite (Sonnenfeld 1984, and references therein). Transformation of gypsum to low magnesium calcite was early described, and experimentally proved by Lattman and Lauffenburger (1974), they altered gypsum to calcite in the presence of suitable organic matter, with the concurrent development of hydrogen sulfide at a pH of 7.5 to 8.5 and a redox potential of -280 to -500mV.

During the day, neutralization of protons from the activity of SOB occurs largely within the pore waters of the structure (Fig.4.17), driving an Oswald ripening process that leads to aragonite neomorphism; while during nighttimes BSR might enhance aragonite replacement. Increasing activity of SRB in depth should be accompanied by increased alkalinities, thus, Mg ions, which might have been forming hydrated complexes with available organic and inorganic ligands, becomes active as to form surface complexes with CO_3^{2-} . The narrow range of the $\delta^{13}\text{C}$ values ($-7.8 \pm 0.3\text{‰}$) in the zone of active gypsum replacement within the thrombolite under examination provide us with further evidence that at least in such system the replacement reactions shown in Figure 4.17 are triggered by bacterial degradation, which by the time of aragonite precipitation supplied lighter carbon isotopes to the local carbon reservoir. The isotopic evidence also suggest that once sulfide oxidation cease, in depth, the activity of sulfate reducers increase the alkalinity of their local microenvironments to values in which increased Mg concentrations become active, in association to an increase of CO_3^{2-} , and additional formation of Mg-rich carbonate infilling the porous spaces take place.

4.5.3. Mg and $\delta^{13}\text{C}$ enrichment in cements

The degree in which authigenic carbonates shows a primary ^{13}C depletion signature is constrained by the specific carbon sources (organic vs. inorganic) that can be incorporated into the growing mineral, the extent in which organic matter degradation occurs in a specific zone of the structure, the rates of carbonate precipitation and the contribution from the ambient water reservoir (Compton 1988; Mazzullo, 2000). In the carbonate cements of the thrombolites, deviation towards normal marine $\delta^{13}\text{C}$ signatures and the Mg distribution can be explained by timing and position of precipitation within the sediment- pore water system. The correlation between $[\text{Mg}^{2+}]$ and $^{13}\delta\text{C}$ within these thrombolites reflect also the interplay between biotic and abiotic processes.

From the examination of Figure 4.14, it can be inferred that once organic matters undergoes the terminal stages of microbial degradation its role driving carbonate precipitation would be surpassed by mineral surface process; in zones where sulfide oxidation have ceased but sulfate reduction prevails, inorganic HCO_3^- dissociates in response to increased alkalinity, thereby producing a shift in the inorganic C equilibrium towards CO_3^{2-} , which dilutes the proportion of isotopically light carbon derived from organic matter degradation (e.g., Wright and Wacey, 2005). Meanwhile, the increase in the ^{13}C content of the local microenvironments is accompanied by an enhanced Mg^{2+} activity because alkaline conditions, by increasing the activity of the carbonate ion, induce a decrease on the hydration state of Mg surface complexes (Wright, 1999). Therefore, the surface reactivity of growing calcite microcrystals together with oversaturation of reactants in the local BSR dominated microenvironment are both factors that promote the incorporation Mg and other divalent cations into the growing crystal lattices.

4.5.4 Distribution of trace metals in cements

Similarities between the partition coefficients (D_{Tr}) of the carbonate cements and the authigenics from mat (Fig. 4.15) indicate that a strong control on accretion

is exerted by the degradation of EPS material trapped during accretion. The enrichment in carbonate cements of some elements such as U might be favoured by its similar ionic radii with calcium (Curti, 1999); the enrichment of biologically active elements (i.e. Cu, Zn, Mo, Sn, Sb), however, may be related to the oxidation of residual organic matter, which in turn may result in locally increased sulfidic conditions (via sulfate reduction) that favour the near-quantitative precipitation and incorporation of these redox sensitive trace metal elements into growing carbonate cements within the thrombolites. As shown by a high resolution chemostratigraphic analysis (Fig. 4.16), this process promotes strong correlations in these elements with depth.

In the thrombolite under examination, it can be hypothesized that the chemistry of the pore waters and the trace element content in carbonate phases precipitating in equilibrium with them is influenced to some degree by the metal affinities of acidic EPS polysaccharides trapped during accretion (e.g., Bergamaschi et al., 1999). The essential element of this working hypothesis is that most primary compounds of EPS have, as a common attribute, the presence of uronic acid moieties (Fazio et al., 1982; Flemming 1995; Sutherland, 2001). Uronic acids would provide abundant deprotonated sites for metal adsorption in the biofilm, acting as an additional mechanism sequestering solutes from lagoon water to the sediments. Not only are bioactive metals preferentially complexed by ionisable sites of EPS in the mat, but the EPS also acts as an efficient diffusion barrier, forming a kind of ion sieve between the overlying water body and the pore-water reservoirs (Flemming and Wingender, 2001).

Within the thrombolites, the mobility of metal species should be controlled by: (1) the cation sequestering properties of the EPS compounds; (2) the redox gradients within the porous structure; (3) the specific affinity of organic functional groups comprising the EPS, and; (4) the various degradation states of the residual EPS, trapped during accretion. Uronic acids have complexation affinities that roughly follow the sequence $Pb^{2+} > Cu^{2+} > Ba^{2+} > Sr^{2+} > Ca^{2+} > Co^{2+} > Mg^{2+}$ (Lee et al. 1996; Davies et al., 2003). As heteropolymeric polysaccharide chains of EPS are selectively degraded by heterotrophs (Decho et al., 2005), the availability

of such metals at depth within these thrombolites may increase with the loss of carboxyl-metal complexes and in a release of trace metals to the pore waters.

The cation flux within the thrombolites should also be governed by alkalinity and redox potential gradients; the redox sensitive trace elements forming hydrated surface complexes in solution may form surface complexes with microcrystalline cements, growing in the more alkaline and coincidentally electronegative active carbonate precipitation zones. Carbonate oversaturation in such zones then favours their incorporation into growing crystal lattices (Rimstidt et al., 1998; Curti, 1999; Schott et al., 2009), resulting in the specific enrichment trends that more likely reflect the availability of organic matter, or the rate of carbonate drawdown in upper layers dominated by autotrophy (Fig. 4.16).

4.5.5 The role of polysaccharides in stabilization (cementation)

As demonstrated by electron microprobe analysis, microcrystalline cements growing in association with residual biomass are Mg enriched. During cementation a variety of cations can be complexed by growing carbonate surfaces. Such cations are sourced directly from ambient water with diffusion pathways limited only by the complexity of the multilayered microbial mat coating the microbialites (e.g., Kamber et al., 2004). Hence, apart from metals that might be concentrated as a result of specific microbial metabolic pathways, minor cations and trace elements in microbialites may be partitioned into carbonates in relation to their abundances in the pore waters; subsequent internal reactive transport partially is controlled by the degradation of microbial biomass trapped during accretion (Kamber et al., 2004, and references therein). Diffusion of metals within the thrombolites may occur through complex migration pathways determined by pH and redox gradients, with available cations being sequestered to some extent by reactive carbonate nuclei growing under alkaline conditions. This mechanism likely contributes to the development of the primary framework for accretion and stabilization of Pirata's thrombolites (i.e., Trichet and Defarge, 1995; Riding, 2000; Decho et al., 2005)

4.5.6 Gypsum pseudomorphs in modern microbialites: A key for the Precambrian?

The time when verifiable pseudomorphs after gypsum appear in shallow marine sediments has assumed importance in the interpretation of the Archean seawater and atmospheric composition (Perry and Lefticariu, 2003; Kasting and Ono, 2006). They may reflect temporal changes in the chemistry of the bulk ocean resulting from pulses of O₂ to the atmosphere and coeval variations on the global sulfur cycle (i.e. Schröder et al. 2008). However, it is thought that before about 1.8 Ga, SO₄ was not delivered to the oceans in sufficient amounts as to generate pervasive sedimentary evaporites (Grotzinger and Kasting, 1993, Canfield 1998). The Archean to Early Proterozoic stromatolitic record, however, contains crystal pseudomorphs that have been consistently interpreted as replacement of calcium (or barium?) sulfates (*e.g.*, Hofmann, 1971; Martin et al., 1980; Walter, 1983; Stanworth and Badham 1984; Holland 1984; Abell et al 1985; Hofmann et al., 1985; Wilks 1986; Simonson et al., 1983; El Tabakh et al., 1999; Hardie, 2003; Pope and Grotzinger 2003; Schröder et al. 2008). Must, but not all, of these evaporites were seemingly formed in marginal marine settings influenced by continental factors producing localized SO₄-rich environments, propitious for local deposition of evaporite in association with stromatolitic successions (Walker et al., 1977; Cameron and Hattori, 1987; Grotzinger, 1994; Canfield et al., 2000; Pope and Grotzinger, 2003).

However, because of the high degree of post-depositional alteration often exhibited by such dispersed and fragmented transitional sequences (Grotzinger 1989), it is difficult to verify most of the reports of pseudomorphs after gypsum in rocks older than ~1.8 Ga (Grotzinger and Kasting, 1993), thus, some of the Late Archean to Paleoproterozoic crystal fans, originally described as primary gypsum crystals, has been reinterpreted as calcite and dolomite pseudomorphs after aragonite (Sumner and Grotzinger 2000). Yet, this reinterpretation is based on measures of interfacial angles (Sumner and Grotzinger, 2000) and on 'elevated' strontium concentrations exhibited by several of the pseudomorphs (averaging

900 ± 400 ppm, with an outlier exhibiting 1800 to 3700 ppm) (Sumner and Grotzinger 2000). Such reinterpretation implies a likely deficiency of gypsum in the pre-Paleoproterozoic rock record. Because interfacial angles may be ambiguous (Hardie, 2004), the sole evidence supporting aragonite instead of gypsum as the more likely primary fibrous mineral in ancient microbialites is elevated $[Sr^{2+}]$ of the pseudomorphs reported by Sumner and Grotzinger (2000). However, from the Sr content in both gypsum and replacing aragonite pseudomorphs from the thrombolites in Laguna Pirata, this piece of evidence seems also highly arguable.

In the gypsum-rich microbialites of Pirata, aragonite occurs as a transient Sr-rich phase after gypsum and it is likely to be neomorphically replaced by calcite in the early diagenetic reactions driven by sulfate reducers within thrombolites. As early noticed by Lattman and Lauffenberg (1974), if BSR is the more active process degrading organic matter the solubilisation of Ca^{2+} from gypsum can lead to calcite. In ancient microbialites the aragonite-to-calcite transition would have masked the Sr partitioning of the preceding gypsum-to-aragonite transition; if the Sr content of calcite polymorphs are interpreted without considering a transient aragonite stage then the primary phase would be mistakenly interpreted as aragonite instead of gypsum. Indeed, in the Permian Zechstein carbonates, both carbonate pseudomorphs after gypsum and the primary Ca sulfates exhibit high Sr concentrations, ranging from 820 to 2,800 ppm in the Zechstein aragonite (Peckman et al., 1999), while the average Sr content of the basal anhydrite is 2,147 ppm (Hryniv and Peryt, 2010). Clearly, the diagenetic process that took place within the Zechstein sequence led to the formation of pseudomorphs after gypsum that retained high Sr concentrations (see Peckman et al., 1999, for details).

Our understanding of the microbiology and constructional processes of fossil stromatolites is based in large part on observations of modern analogs (Awramik and Sprinkle, 1999). Laguna Pirata is an ideal natural system for studying the intricate biogeochemistry of microbe interactions in lithifying microbial mats, and their catalytic effect on mineral dissolution and precipitation processes that result in an early replacement of gypsum by aragonite. Understanding the controls on the early diagenetic processes that occur within these modern microbialites may

provide new insights into analogue processes that occurred in ancient (ca. 2.5-1.8 Ga) shallow marine to evaporitic sequences. Overall, the unusual organosedimentary structures from Laguna Pirata hold great promise as a Precambrian analogue, and while the data presented in this current study has strong bearing on the interpretation of the Precambrian evaporite record, it is by itself not sufficient to ultimately solve the problem of recognizing primary gypsum (monoclinic) from aragonite (orthorhombic) pseudomorphs in the ancient rock record. Future work drawing direct comparisons between ancient (candidate) and modern (confirmed) gypsum microbialites will certainly aid the interpretation of major ion chemistry and geomicrobiology characterizing shallow marine and evaporative sequences in deep time.

4.6 Conclusions

In Laguna Pirata the production of EPS by the photoautotrophic community and its subsequent degradation by the heterotrophic community promotes the development of localized alkaline sites within the organosedimentary structures under examination. These sites become zone active of gypsum dissolution carbonate precipitation, where the metabolic activity of sulfate-reducing bacteria, by attacking the sulfate moieties of primary gypsum favours further cementation.

Mg-calcite can occur as dissolution enhanced cement (micrite/ microspar) infilling organic-rich intergranular spaces to form zones which exhibit fine micrometre-scale lamination, largely defined by the relative abundance of magnesium. In the specimen analyzed two types of carbonates occur: (1) an isotopically lighter ($\delta^{13}\text{C} = -7.4$ to -5.3‰ ; $\delta^{18}\text{O} = -0.1$ to $+1.1\text{‰}$) replacing gypsum and, (2) a Mg-enriched and isotopically heavier dissolution-enhanced cement ($\delta^{13}\text{C} = -2.7$ to -3.2‰ ; $\delta^{18}\text{O} = -0.2$ to -0.1‰). The Mg- and trace metal-content seems to follow a likely correlation with the degradation states of microbial biomass trapped during accretion.

The lithification model herein discussed assumes that dissolution-precipitation cycles occur in a system that can be at least temporarily closed, this because EPS organic matrix coating the structure acts as a diffusion barrier for

biologically important ions in solution in the pore waters. The carbon signatures as well as the Mg content are spatially controlled and time dependant. Regarding the carbon isotopic compositions, the observed trends are most likely related to mixing of carbon sources within the structure. Enrichment of cements relative to replaced aragonite (^{13}C depleted) can be explained by higher contribution of inorganic carbon to the interplay between $\delta^3\text{C}_{\text{org}}$ and $\delta^3\text{C}_{\text{inorg}}$ in the reservoir. Relatively later cements incorporate ^{13}C -enriched carbon sources (e.g. dissolved inorganic carbon) and in a minor extent isotopically lighter carbon from the heterotrophic activities of sulfate-reducing bacteria. Meanwhile, the organic source $\delta^3\text{C}_{\text{org}} \approx -14.7\text{‰}$, has a leading role in the isotopic equilibrium of carbonate during aragonite precipitation.

Provided that enough polyssacharidic material, amenable to be oxidized, is present, in zone where light can penetrate the translucent structure then sulfate reduction can develop in close spatial and temporal relation with sulfide oxidation.

The combined action of this microbial consortium results in the accumulation of elemental sulfur in association to gypsum and aragonite. The cementation mechanism is thought to proceed as follows. First, extra-cellular polysaccharides (EPS) concentrate Mg ions by preferential adsorption of Ca from the hypersaline waters into the mat as an organic matrix. Second, carbonate phases nucleated within the biofilm may partially dissolve, due to photosynthetic activity; the remaining stable fraction may later serve as nuclei for the precipitation of microcrystalline cements, a process that occurs in the available nucleation sites of the more refractory organic matrix. Third, calcium ions from bacterially-induced gypsum dissolution, under circumneutral pH conditions, promote aragonite as replacement phase, it exhibit both, a lighter carbon isotopic signal and a relatively high Sr content. Fourth, the remaining marine-derived carbonate species, because of the high alkalinity resulting from BSR, are shifted towards a CO_3^{2-} equilibrium, thus facilitating the growth of a second generation of early diagenetic cements that may potentially incorporate Mg^{+2} .

As described above, the microbial involvement on precipitation of primary gypsum is still elusive, and it might precipitate abiotically within the EPS matrix saturated in both, SO_4 and Ca ions and with oxygen availability. However, Thus, degradation of the protein fraction of EPS by sulfate reducers may (1) increase the solubility of gypsum; (2) led to oversaturation of sulfate in the organic-rich substrate that diffuse and becomes a readily available electron acceptor for SRB, which also utilize organic carbon to generate additional sources of carbonate ions

The distribution of trace element in the thrombolites framework suggests that dissolution and precipitation reaction leading to lithification of the structure are in turn largely regulated by decaying biofilm material trapped during accretion. The development of dynamic geochemical gradients within the within the sediments, due to the combined action of functional microbes involved in the degradation of microbial biomass, result in specific geochemical signatures in the growing microcrystalline cements. Metal desorption associated to the degradation of the trapped biomass supply the surrounding pore waters with trace metals that form hydrated complexes with the reactive calcite surfaces, due to oversaturation of reactants these metals are incorporated into growing early diagenetic carbonate cements growing under anoxic and localized more alkaline conditions, leading to enrichment trends in depth.

Currently, renewed efforts to model early ocean chemistry are spurred by the results from Poulton et al. (2010). However, much work integrating geochemical and stratigraphic data sets remains ahead before we can have a true sense of the three-dimensional redox structure of Precambrian oceans, and how this has varied through this critical time (Fike, 2010). The Late Archean to Proterozoic shallow-marine microbialites are worth to be included in the stratigraphic data to be evaluated, in that sense Los Roques gypsum-rich microbialites may provide us with an analogue to refine our knowledge of Precambrian shallow marine depositional setting and would also help us to better understand what geological factors controlled such environments to become suitable habitats for early life to cause the build-up of atmospheric oxygen.

Sample	Ca²⁺ (mmol)	Mg²⁺ (mmol)	Sr²⁺ (μmol)	Salinity (‰)	SO₄²⁻ (mmol)	Total Alkalinity (mM/L)
Laguna Pirata						
Evaporated	17.5	108.9	97.12	90	66.8	169
seawater						
Seawater at						
Los Roques	10.1	52.2	96.1	40	31.6	134

Table 4-1. Chemical features of surface Pirata's water. The mean chemical composition of Los Roques seawater (sampled in two different sites in the unrestricted lagoon) is also shown for comparison.

Subsample	Location	MgO	$\delta^{13}\text{C}$	$\delta^{18}\text{O}$
1a	Base	21.51	-2.70	-0.10
1b	Base	20.40	-1.93	-0.55
2	Base	7.82	-3.20	-0.20
3a	Middle	4.35	-7.40	-0.10
3b	Middle	6.00	-8.36	-0.10
3c	Middle	5.36	-7.70	-0.55
4	Interface	1.94	-5.30	-1.1
5a	Mat auth	4.81	-5.05	-0.60
5b	Mat auth	6.55	-7.17	-1.14
6a	<i>Halimeda</i> sp. Open lagoon	N/D	1.75	-3.05
7a	<i>Allochem.</i> (<i>Halimeda</i> sp.)	N/D	2.44	-1.51
7b	<i>Allochem.</i> (<i>Halimeda</i> sp.)	N/D	2.42	-1.54
7c	<i>Allochem.</i> (<i>Halimeda</i> sp.)	N/D	1.70	-1.92

Table 4-2. Stable C and O isotopes values from Los Roques microbialites (V-PDB), together with its Mg oxide content (weight %). *Halimeda* sp. values are shown for comparison. See Fig.4.13 for approximate location of the subsamples within the thrombolite.

Element	Average Concentration (ppm) in Thrombolite Cements	Average Concentration (ppm) in Mat Authigenic Samples	Degree of enrichment	Degree of depletion
Li	4.1	2.4	1.7	
Na	6,603.4	5,584.2	1.2	
Ti	171.9	177.2	---	---
V	3.0	1.6	1.9	
Cr	12.8	10.7	1.2	
Mn	7.7	9.0		0.9
Fe	124.4	79.1	1.6	
Co	0.9	0.2	3.6	
Ni	1.7	1.7	1.0	
Cu	0.008	0.001	7.6	
Zn	10.9	4.9	2.2	
Sr	5,389.3	4,585.3	1.2	
Y	0.3	0.4		0.6
Zr	0.4	0.4	---	---
Nb	0.1	0.1		0.6
Mo	3.6	0.3	12.2	
Cd	0.3	0.4		0.9
Sn	0.8	1.1		0.7
Sb	0.4	0.1	2.6	
Pb	1.0	0.6	1.6	
U	5.2	2.1	2.5	

Table 4-3. Comparison of trace concentrations of cements in the microbialites and mat's authigenic carbonates

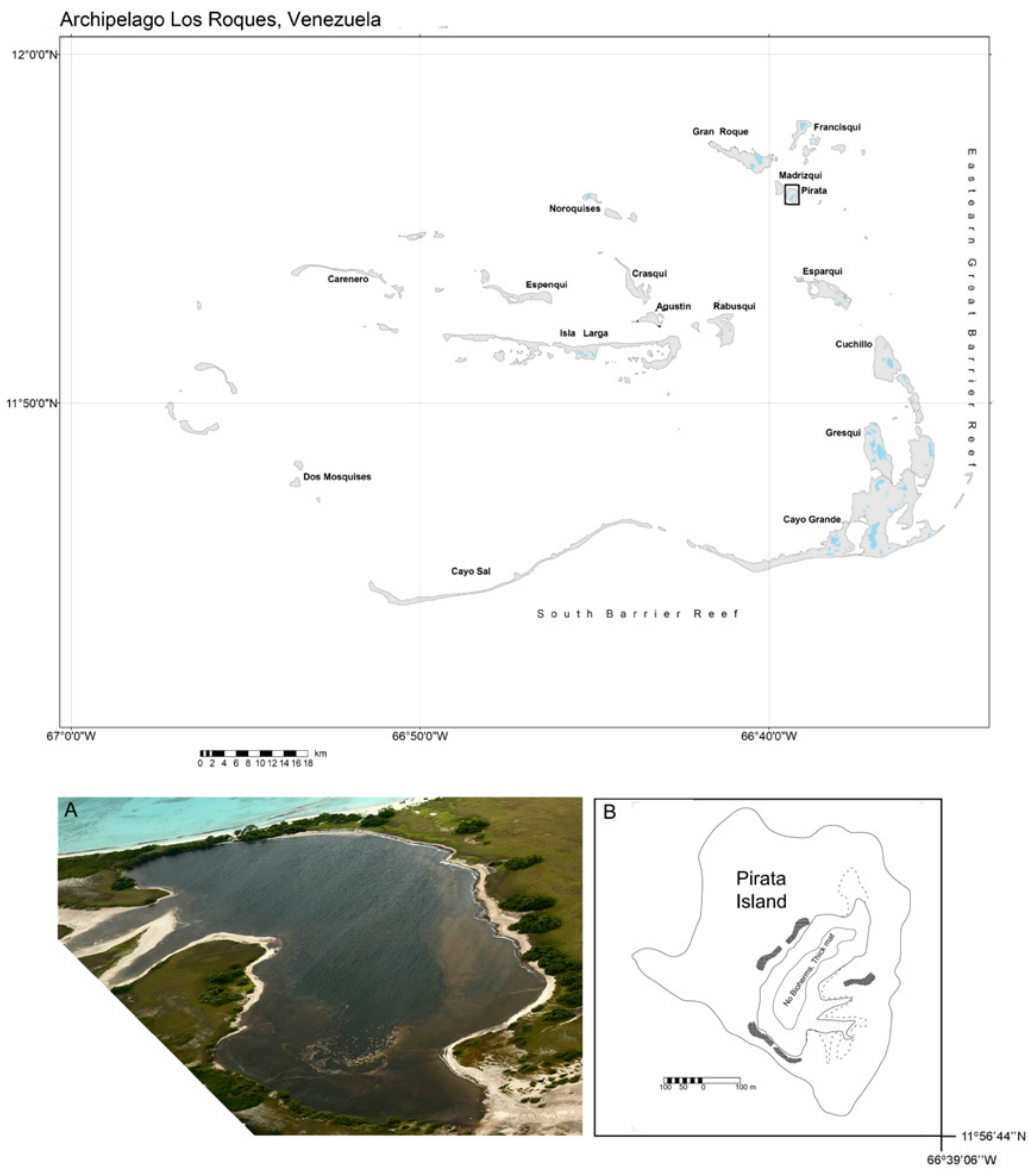


Figure 4-1. Location of the study area. Inset A: Oblique aerial view of Laguna Pirata. Inset B: Map of Pirata island.

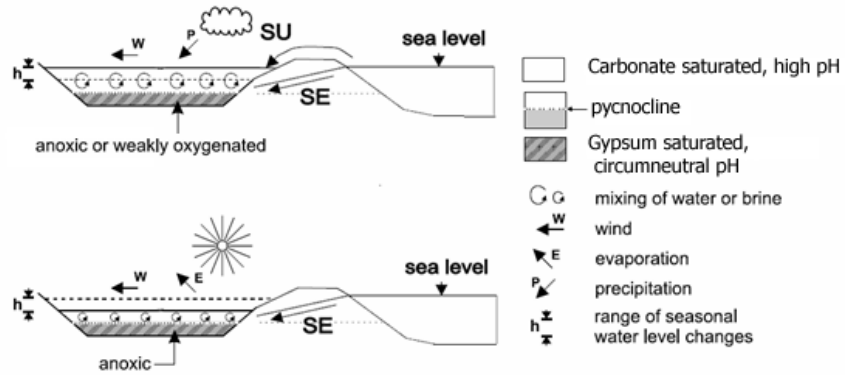


Figure 4-2. Schematic hydrological model of Laguna Pirata. SE: seepage seawater influx, SU sporadically, during storm events, surface seawater influx may occur.

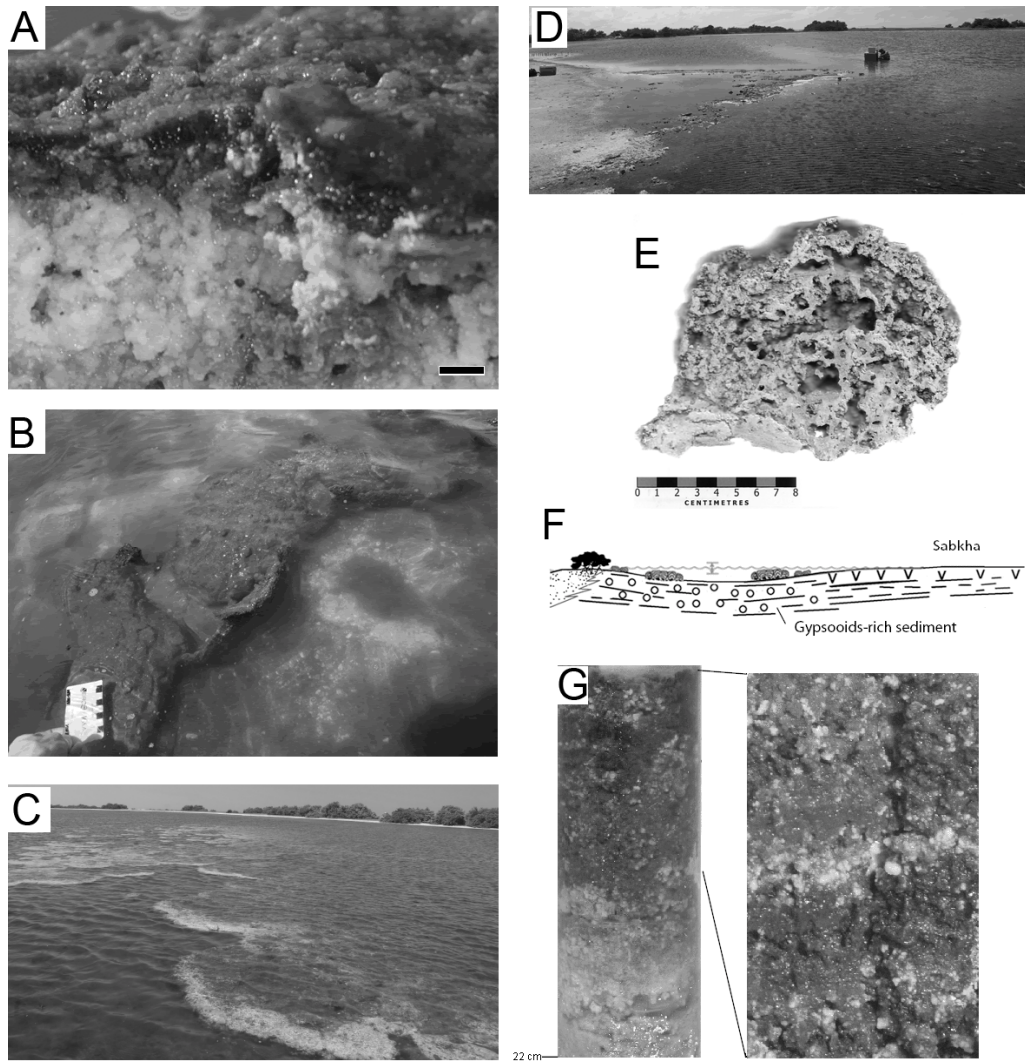


Figure 4-3. General macroscopic features of the microbially-influenced sedimentation in Laguna Pirata. (A) Microbial mat coating a thrombolite, the mat exhibit distinctive layering related to vertical array of bacterial communities. Note the masses of microcrystalline gypsum Scale bar is 10 mm. (B) Close-up of coalesced thrombolites, the bacterial mat coating the thrombolite is noticeable, water depth 10 cm. (C) Dense coalescent growth of thrombolites, water column may vary from 15 cm to 45 cm. (D) *in situ* microsensing of the bacterial mat; view from the sabkha (E) One of the collected thrombolites. Note that the thrombolitic fabric (clotted) is dominant over the stromatolitic fabric (laminated zone) more evident in the base of the structure. (F) Distribution of carbonate-evaporite subspecies in Laguna Pirata. (G) The organic- gypsum rich sediment in the deepest part of the lagoon.

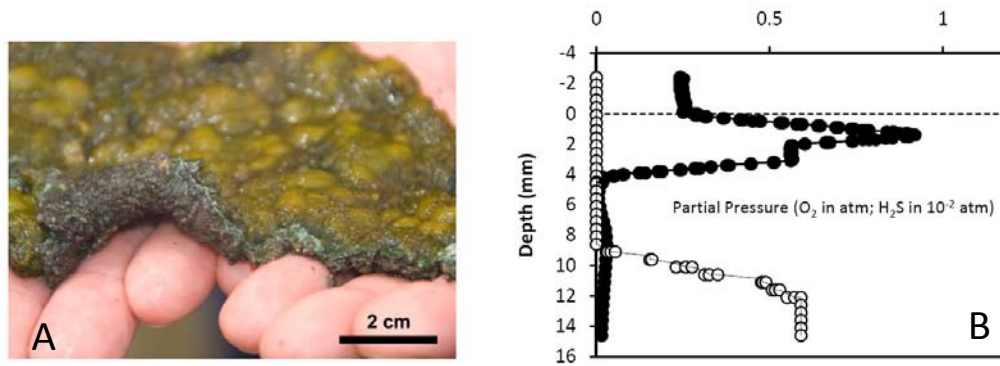


Figure 4-4. Macroscopic and microelectrode data from the bacterial mat associated with the accreting thrombolitic structures A: Bacterial mat that was coating the thrombolite specimen shown in 4-3(E). The upper layer is dominated by cyanobacteria, with algae and diatoms also present; underneath the upper layer, between 4 and 10 mm depth, a purple to green layer can be distinguished, the layer has a white fibrous lamina of elemental sulfur. B: Daylight microelectrode profile of the bacterial mat shown in (A). The partial pressure of oxygen in the mat/water interface rises dramatically near the surface, from 0.25 to 0.95 atm. From 4 to 10 mm there is a zone of steep opposing gradients of oxygen (from above) and sulfide produced by sulfate reducing bacteria (from below).

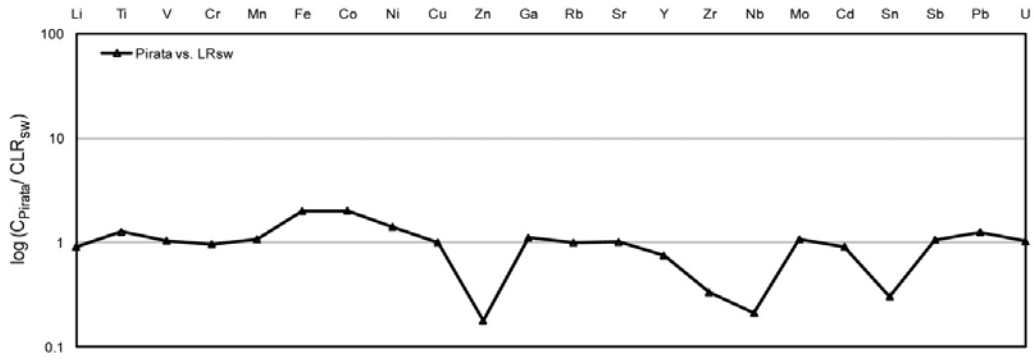


Figure 4-5. Logarithmic plot showing the enrichment/ depletion factors of certain trace elements in the surface waters Laguna Pirata, normalized respect Los Roques seawater (LR_{sw}).

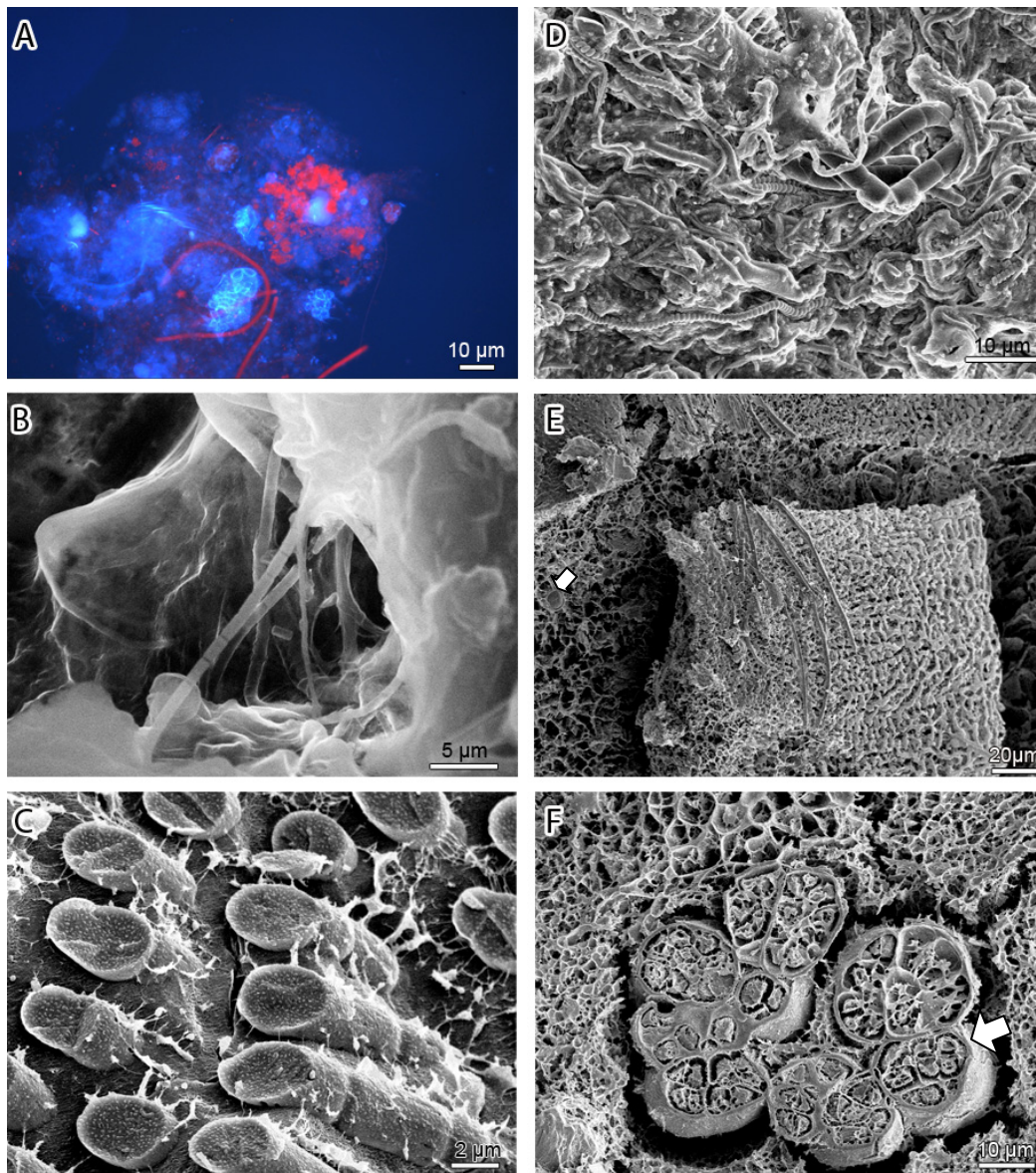


Figure 4-6. Delicate microbial features from the biofilm associated to Laguna Pirata's microbialites. A: Autofluorescence at the upper layer of the microbial mat shown in Figure 4.4(A). Photosynthetic bacteria (red autofluorescence excitation) are within their EPS matrix (blue autofluorescence). B, C: Filamentous bacteria (in their amorphous exopolymeric sheath). D: The high microbial diversity from the middle layer of the thrombolite-constructing mat, spirochetes and other unidentified filamentous bacteria, presumably sulfate tolerant, are evident. E: Shows abundant coccoid bacteria in a staphylococci arrangement containing an associated filamentous community. The arrow shows a micrometre-scale mineralized spheroid shown in detail in Figure 4.9F; bottom layer at the shallow lagoon's mat. (F) Bacterial community from the deepest thick-mat, these rod-shaped bacteria usually form aggregates within a continuous sheath (arrow).

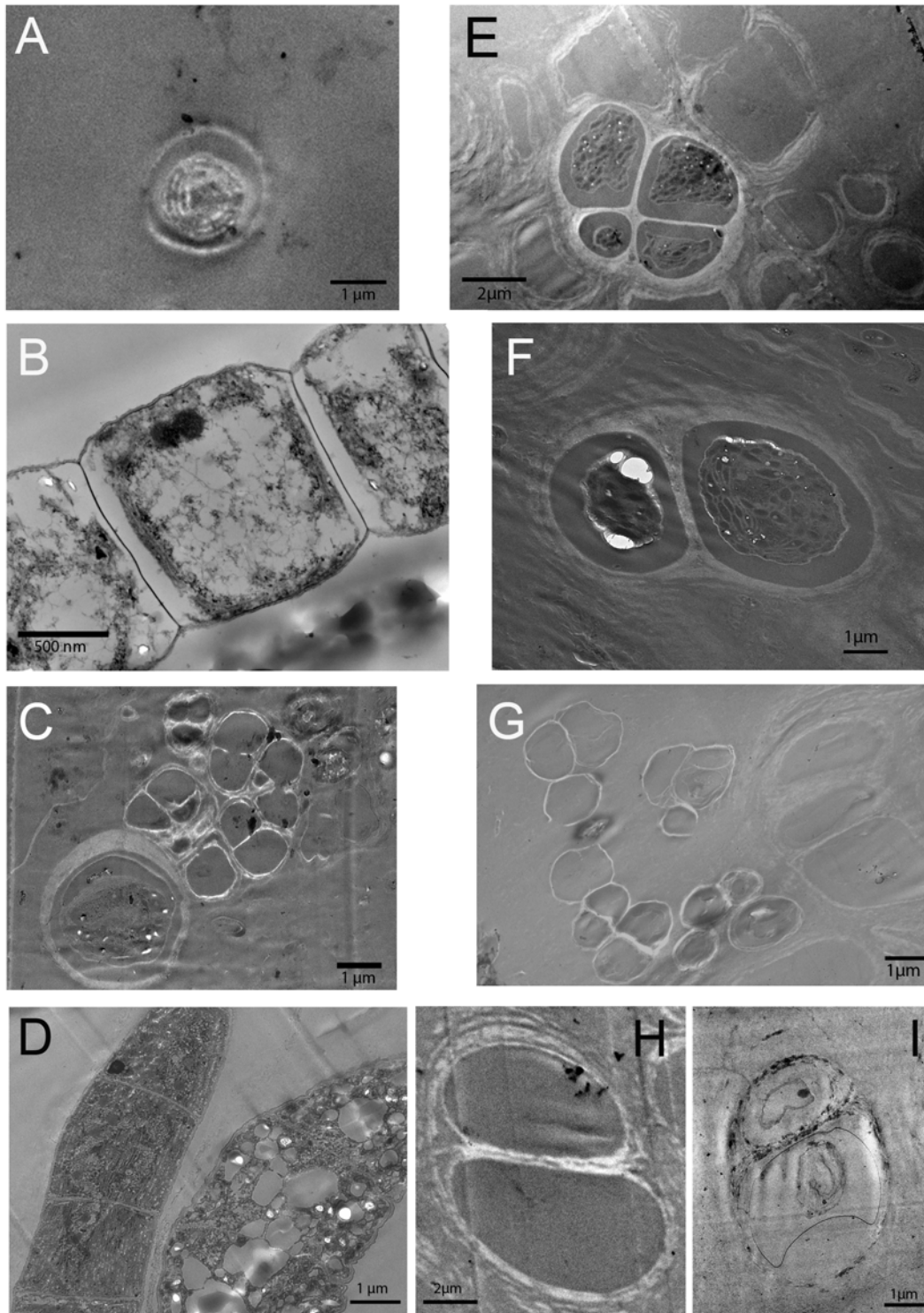


Figure 4-7. Transmission electron micrographs (TEM) showing the ultrastructure of microbes observed in Laguna Pirata's mat. A: *Syenocochus*-like bacteria in the upper layer. B: Unidentified distinctive segmented filamentous microorganism; upper layer. C: coccoid purple photosynthetic bacteria showing intracellular mineralization; middle layer at the thrombolite-constructing mat.

Note their association with other diplococci bacterial clumps similar to the ones shown in G (deepest lagoon). D: A couple of different unidentified anaerobic photosynthetic bacteria from the middle layer. Note distinctive thylakoids-like structures in the left side cell and the abundance of lipids in the right side cell; holes that remain after intracellular deposits fall out. E, F: purple cocci sulfur bacteria with probable affinities to *Thiocapsa* (Buchanan and Gibbons, 1974); bottom layer at the shallow lagoon's mat. G: Presence of a distinct membrane bounded electron-dense region and the absence of 'thylakoids' suggests these rod shaped cells are heterotrophs. H-I: Unidentified microbes from the mat developed at the 'deep lagoon' (H: unstained, I: stained).

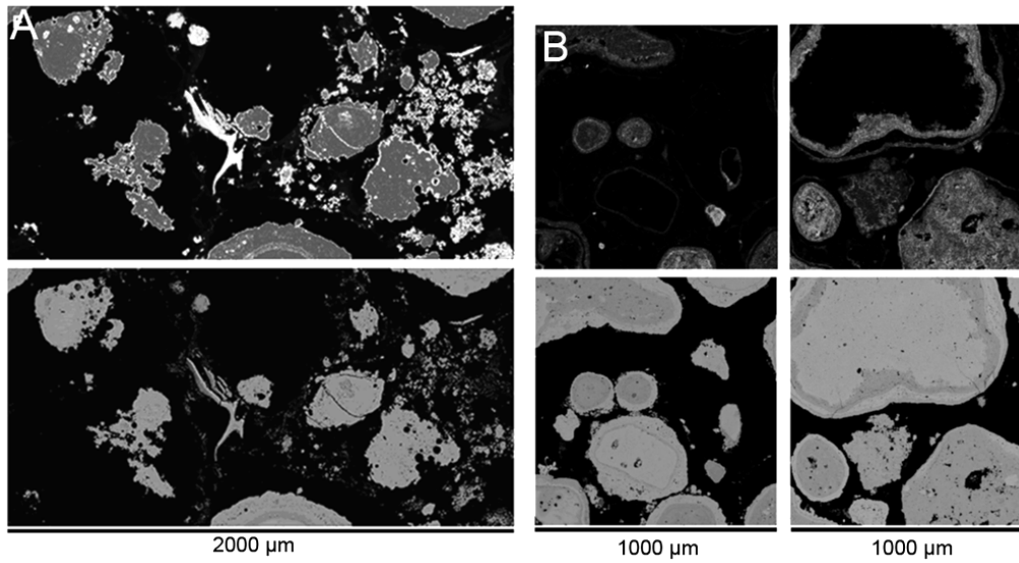


Figure 4-8. Microtextural features in sediments from the thrombolite-constructing mat. CaO (A) and MgO (B) X-ray maps (above), BSE images (below), A: unfilled microbores and micritization/obliteration of authigenic/ trapped sediments within the microbial mat. B: advancing of the micritization process would fuse grains together, the X-ray maps (above) show rims enriched in Mg^{2+} (light gray).

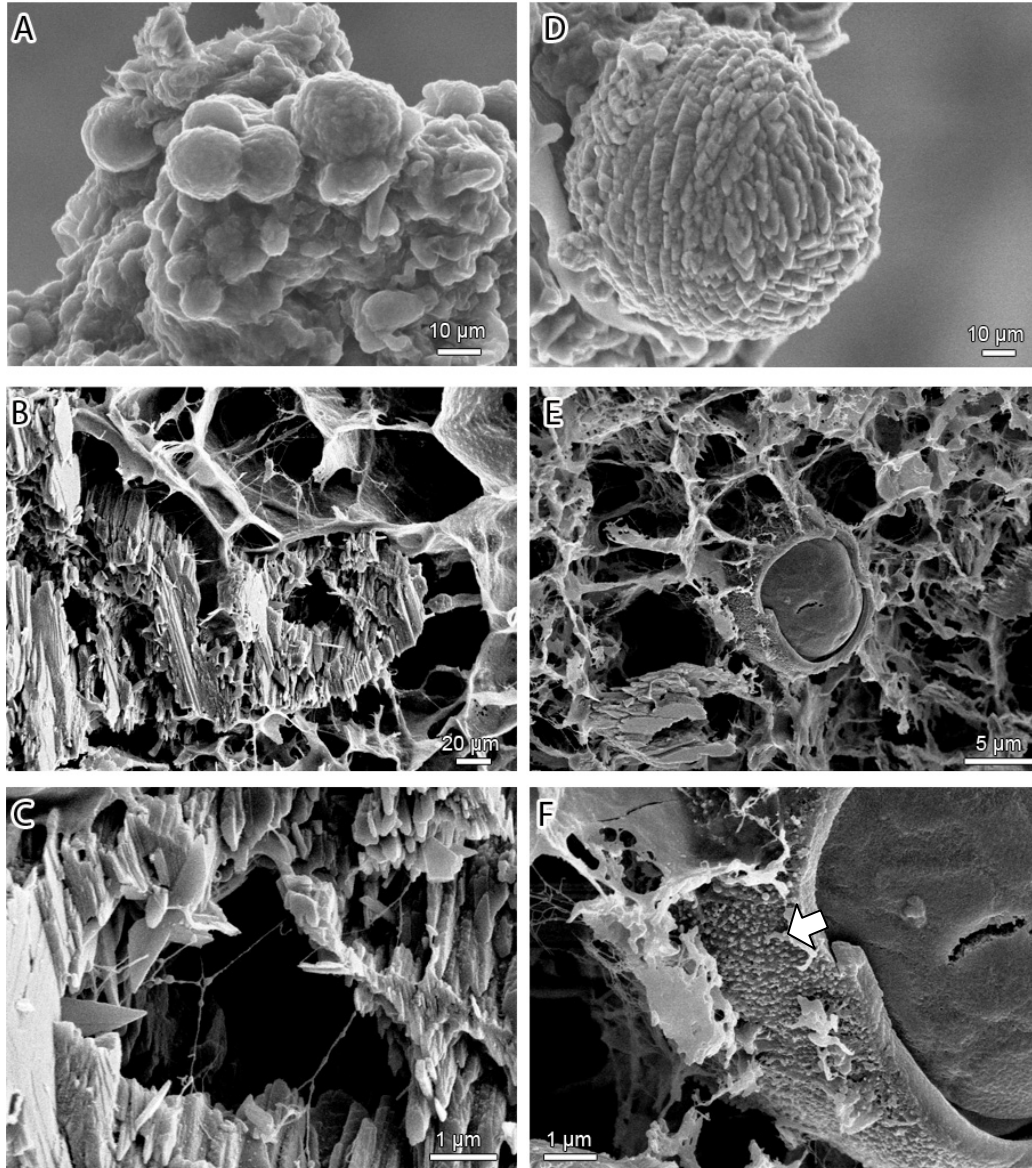


Figure 4-9. Cryo-SEM showing authigenic carbonate held by the mat coating the thrombolites. A: calcite spheroidal aggregates. Scale bar 10 μm . B: aragonite aggregates are held in the gelatinous EPS matrix. Scale bar 20 μm . C: Detailed view of “B”, the tightly packed micrite peloids shows EPS strands crossing the porous spaces of the mineral aggregate. Scale bar 1 μm . D: Detail of a dumbbells. Observe the blocky calcite crystallites that compose the spheroid. Scale bar 10 μm . E: A spheroid surrounded by an EPS sheath. The density of these textural features within the purple mat is lower than micrite/ microspar microfabric. EDX analysis revealed that the sheaths are Mg-enriched; while the spherical particle is not. Scale bar 1 μm . F: Detailed view of “E”, note the presence of nanobacteria-like textures (Folk and Lynch, 1993) within the sheath surface (Arrow).

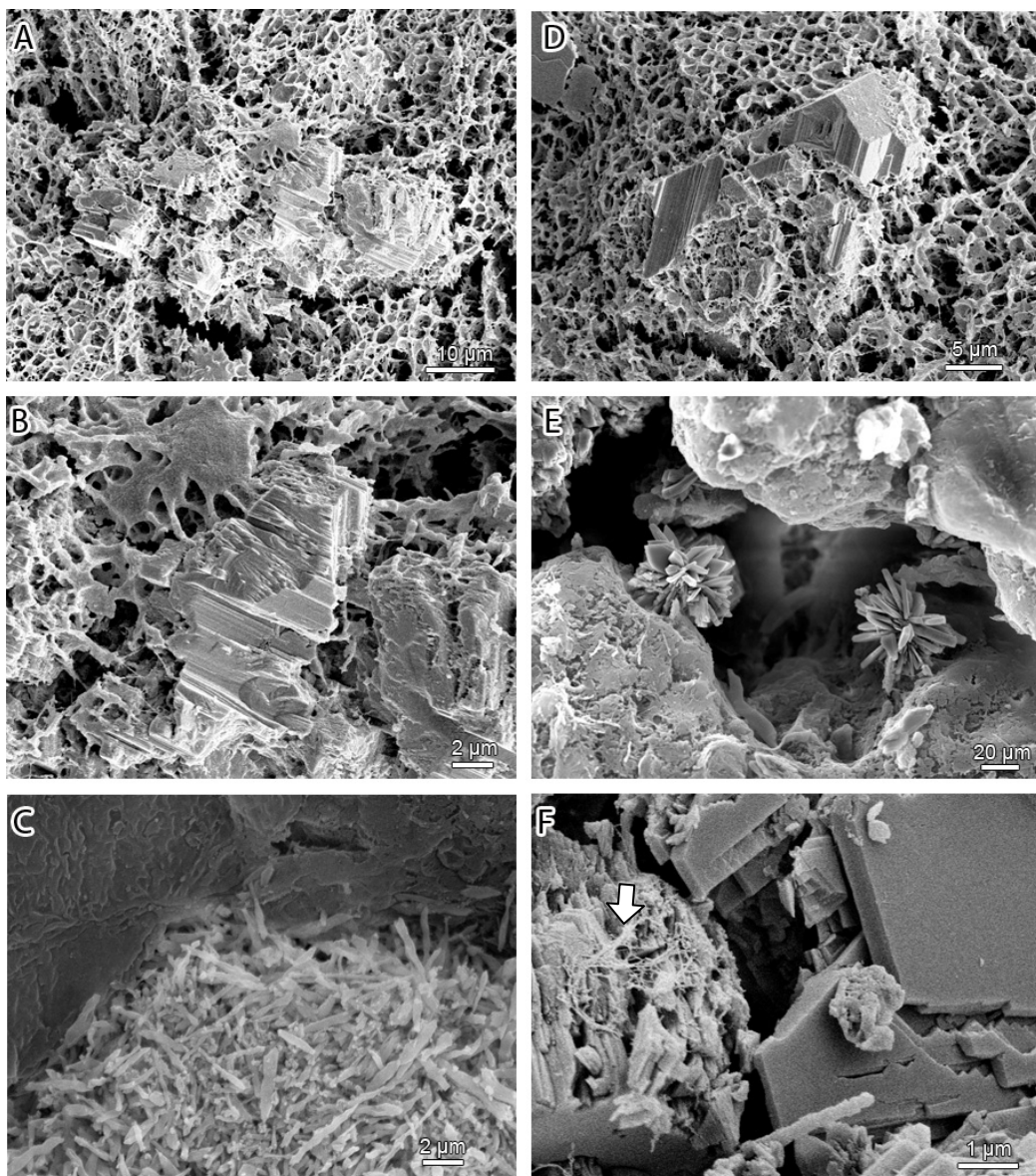


Figure 4-10. Biological SEM of the mat supporting gypsum crystals. Cryo-SEM (A, B, D) and critical point dried (C, E, F) samples showing morphologies of gypsum crystals embedded by the organic slime at the deepest Pirata Lagoon. A: General view of the EPS network, note subhedral gypsum crystals held in the mucous matrix. B: Loosely packed subhedral gypsum within the EPS network, note EPS strands crossing the porous space. Scale bar 1 μm . C: Gypsum crystal surface exhibiting a replacement feature composed of randomly oriented, bladed aragonite (arrow). D: A subhedral lenticular gypsum, the prisms faces $\{110\}$, $\{010\}$ and $\{111\}$ are present. E: Gypsum rosettes crystallized at the fibrous spaces of the crystal aggregates shown in “D”. The individual “petals” of these rosettes are lenticular crystals with minor twin. F: A rosette-like aggregate with

minor twin formation. These crystal aggregate, are arranged sub-parallel to {103} face; {111} also present. The arrow shows fibrous interstitial aragonite.

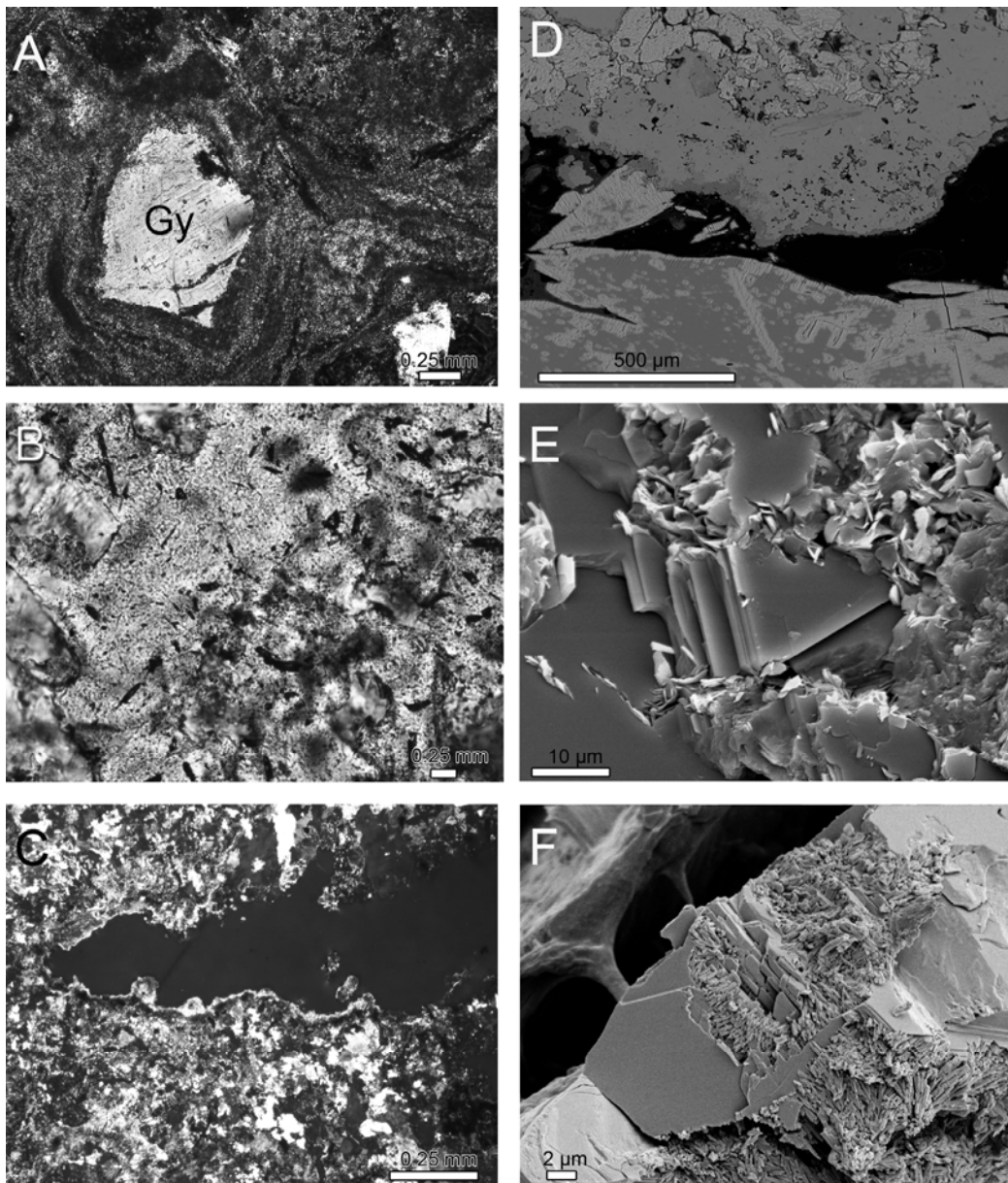


Figure 4-11. Replacement of gypsum by carbonates. Micritic cements can be found infilling inter- and intragranular spaces. Standard (A-C), backscattered electron (D) and SEM (E,F) petrography. A: Base of the thrombolite, the image shows a subhedral, corroded, gypsum crystal (Gy) draped over by concentric micrite/microspar laminae. B: Micrite/ microsparite aggregates around corroded and partially dissolved gypsum crystals. Dark areas dominantly represent accumulation of organic material. Scale bar 10 μm . C: irregular fenestral void enclosed by clotted-laminated micrite/ microspar cements. D: Calcification of gypsum leads to the formation of pseudomorphs. In the pseudomorphs, calcite replacement mimics the $\{001\}$ crystallographic planes of gypsum although calcification appears to preferentially occur perpendicular to $\{010\}$ cleavage of

gypsum, preserving the (010) cleavage surface. E: Poikilotopic gypsum enclosed Mg-enriched cement. F: Solution fronts on gypsum crystals often show aragonite crystals sub-perpendicularly orientated to these surfaces.

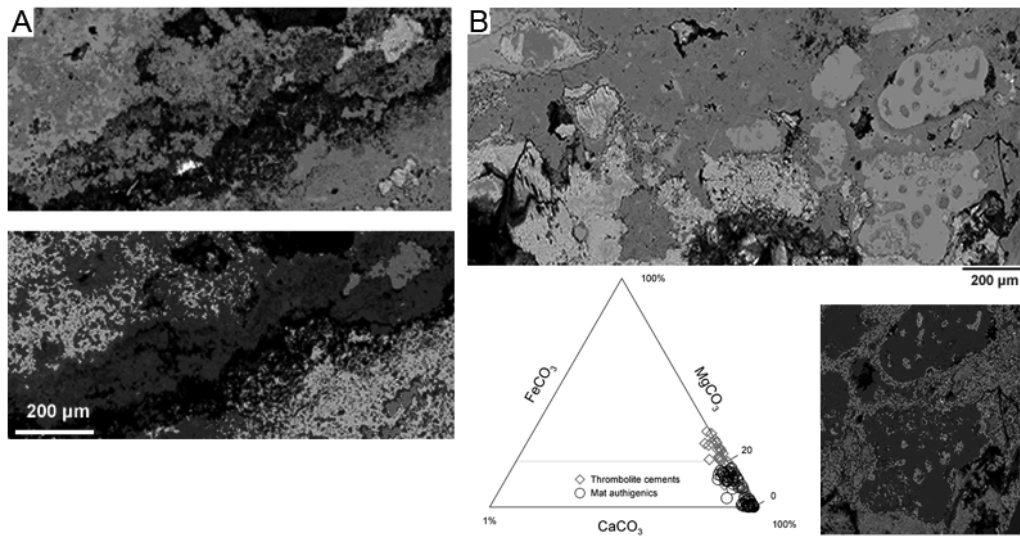


Figure 4-12. BSE and X-ray map of the basal part of the thrombolite specimen. A: fine scale lamination, largely defined by the relative abundance of magnesium (darker areas in the bottom image). B: BSE and X-ray map show Mg-enriched zones and its textural relationship with aragonite (darker areas in the bottom image). The arrow shows infilled microborings-like as observed in the lower lithified carbonate crusts. C: Quantitative compositional data (mol%) for calcite cements and mat authigenics. The cements are Mg-enriched relative to the mat's authigenics.

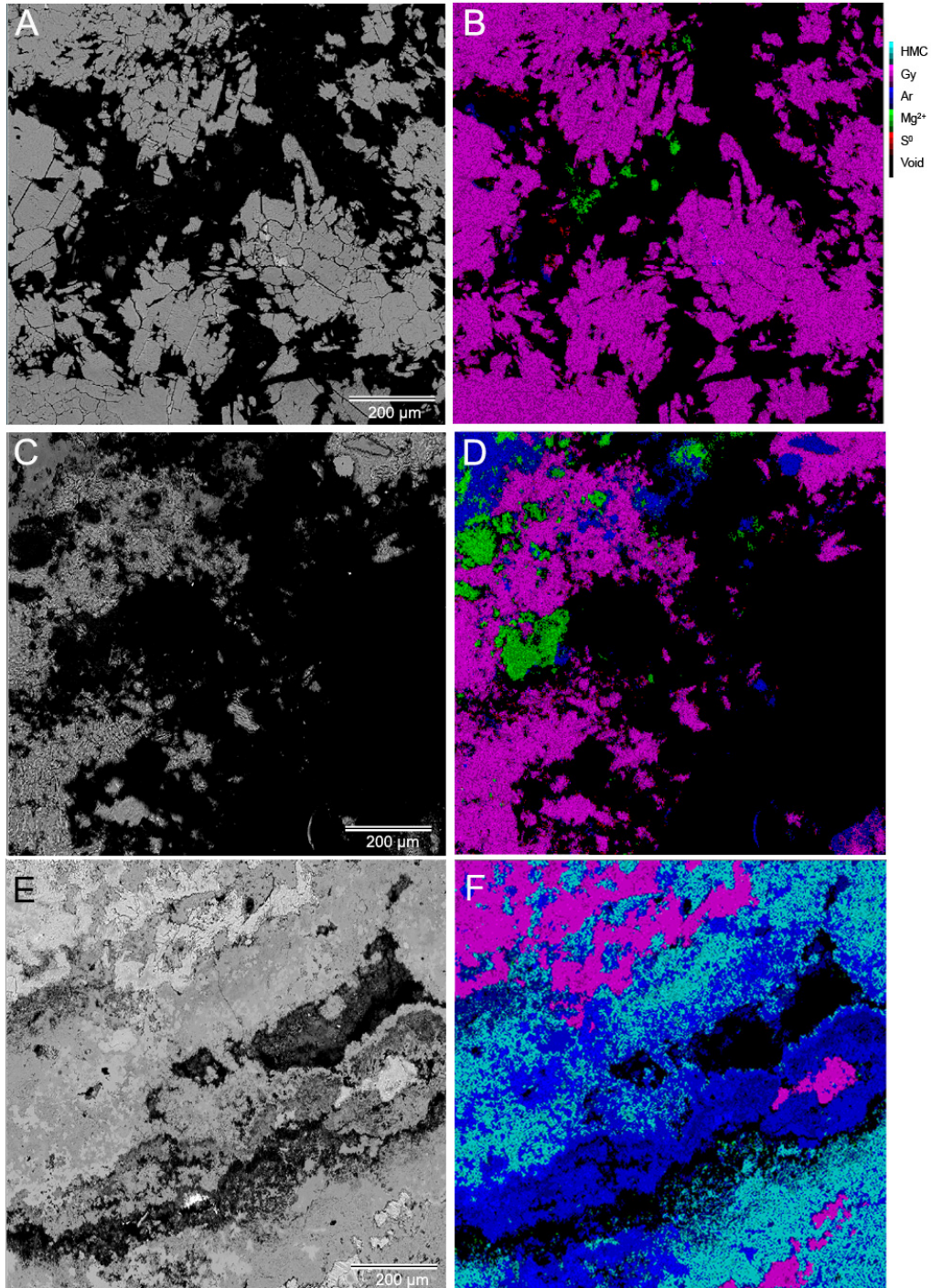


Figure 4-13. BSE and composite X-ray maps (S, Mg and Ca) of different zones of the thrombolite specimen examined. A-B: approximately 2 cm from the top of the structure; C-D: approximately 7 cm from the top of the structure. E-F: at the laminar basal part (~12 cm from the top) of the structure. Note S^0 and Mg^{2+} accumulations in B and D and the relative abundance of Mg*rich calcites towards the base (F).

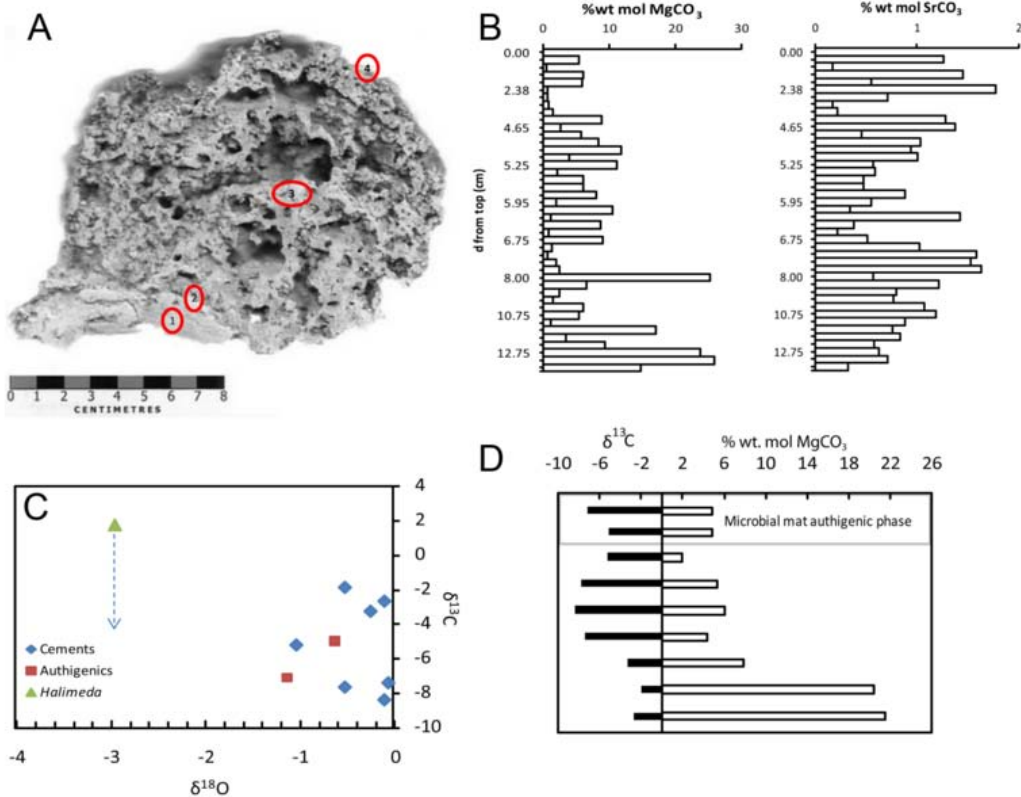


Figure 4-14. Carbon and oxygen stable isotopes and major element distribution in one of the specimens collected. **A:** Sub-sampled zones for isotopic analysis within the specimen. **B:** Down-depth molar variation of MgCO_3 and SrCO_3 as obtained by LA-ICP-MS. **C:** The $\delta^{13}\text{C}$ versus $\delta^{18}\text{O}$ plot differentiates microbial carbonate from aeolian transported *Halimeda* sp. fragments. **D:** Carbon isotopic data with depth in the specimen; a strong positive correlation was found to exist between the average $\delta^{13}\text{C}$ values and the MgCO_3 content of both microbial mat carbonates and the thrombolite cements.

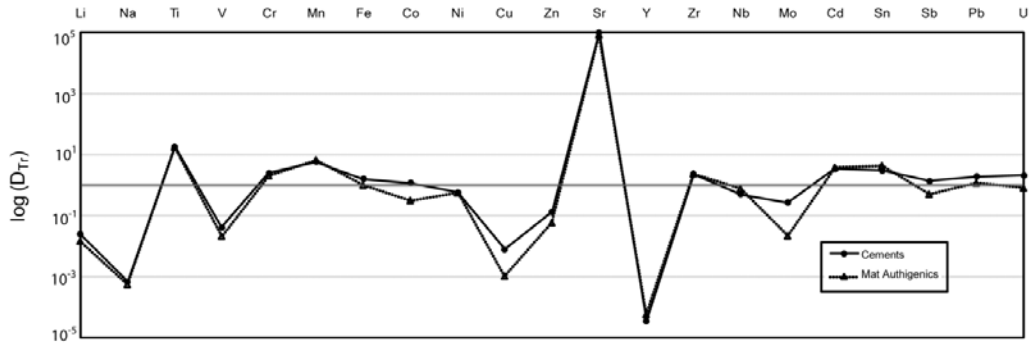


Figure 4-15. Logarithmic plot showing relevant metal-enrichment/depletion trends between carbonates phases under examination. See details in the text.

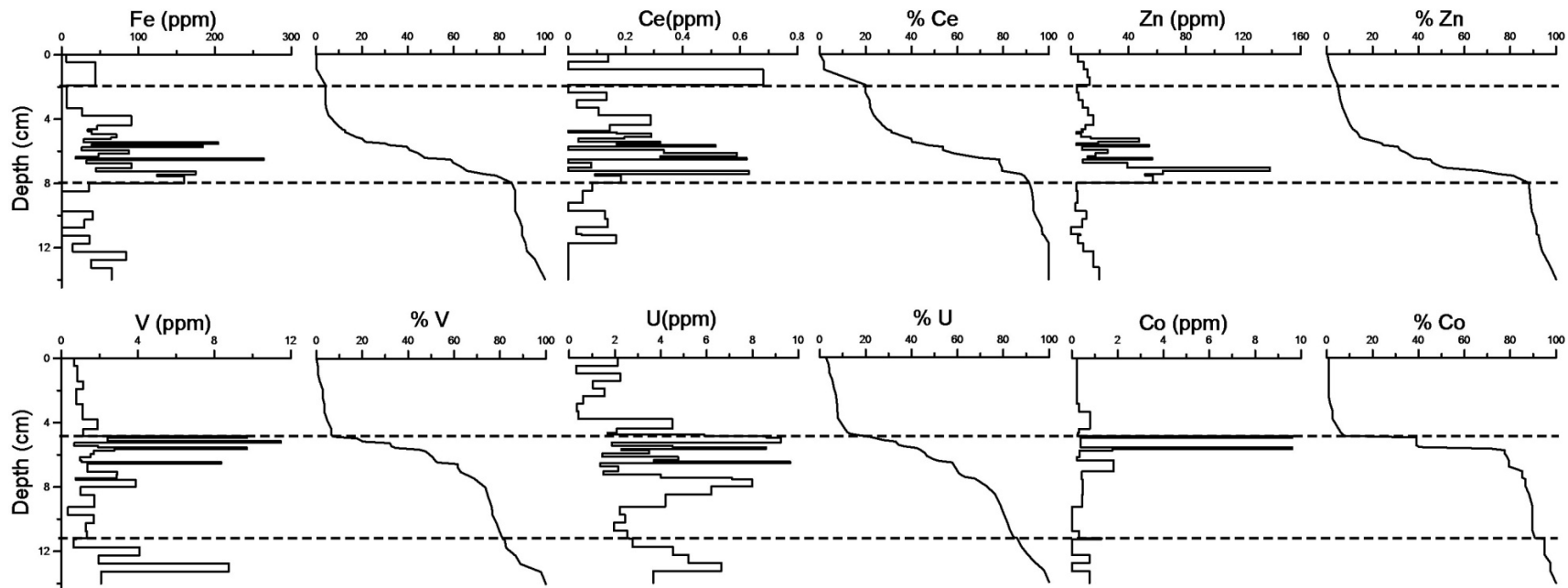


Figure 4-16. Summary of relevant vertical enrichment trends within the specimen under examination. The covariance of certain metals within the vertical profile can be interpreted in terms of the microbial process involved in local metal enrichments. To the right of each elemental contour there is an accumulative % vertical profile showing a striking enrichment towards the centre of the specimen. See text for details.

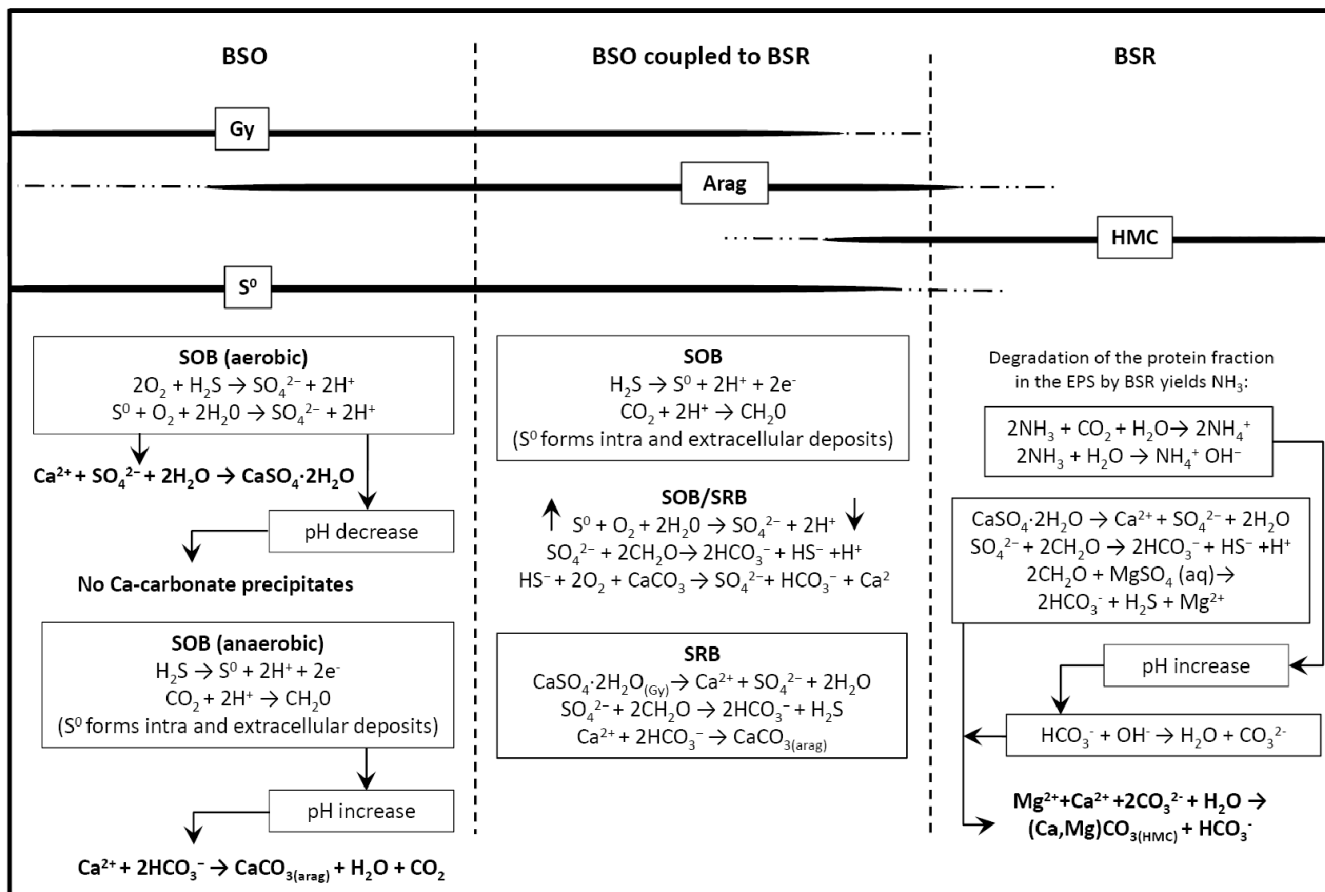


Figure 4-17. Paragenetic diagram and relevant metabolic pathways determining mineral associations within thrombolites

4.7 References

- Abell PI, McClory J, Martin A, Nisbet, EG, Kyser TK. 1985. Petrography and stable isotope ratios from Archaean stromatolites, Mushandike Formation, Zimbabwe. *Precambrian Res.* 27:385–398.
- Airs R, Kelly BJ. 2003. A high resolution study of the chlorophyll and bacteriochlorophyll pigment distributions in a calcite/gypsum microbial mat. *Organic Geochemistry* 34:539-551.
- Aitken JD. 1967. Classification and environmental significance of crypt- algal limestones and dolomites, with illustrations from the Cambrian and Ordovician of southwestern Alberta. *Jour. Sed. Petrol.* 37:1163-1178.
- Amend. T., 1992, Los habitantes del archipiélago en el pasado y el presente. In . Amend T. (ed.) Parque Nacional Archipiélago Los Roques. Parques Nacionales y Conservación Ambiental No. 3, (Caracas, Editorial Torino) 1-42 pp.
- Amjad, Z. 1996. Scale inhibition in desalination applications: an overview. *Corrosion, NACE-96-230.*
- Andres M, Reid RP. 2006. Growth morphologies of modern marine stromatolites: A case study from Highborne Cay, Bahamas. *Sedimentary Geology* 185:319-328.
- Arnosti C, Holmer M, 1999. Carbohydrate dynamics and contributions to the carbon budget of an organic-rich coastal sediment. *Geochimica et Cosmochimica Acta* 63: 393–403.
- Awramik S, Sprinkle J. 1999 Proterozoic stromatolites: the first marine evolutionary biota. *Historical Biology* 13: 241-253.
- Babel M. 2007. Depositional environments of a salina-type evaporite basin recorded in the Badenian gypsum facies in the northern Carpathian Foredeep. *Geological Society, London, Special Publications* 285:107-142.
- Bergamaschi BA, Walters JS, Hedges J. 1999. Distributions of uronic acids and O-methyl sugars in sinking and sedimentary particles in two coastal marine environments. *Geochim. Cosmochim. Acta* 63, 413–425.
- Berner RA. 1975. The role of magnesium in the crystal growth of calcite and aragonite from seawater. *Geochim. Cosmochim. Acta* 39:489-604.
- Brand U. 1994. Morphochemical and replacement diagenesis of carbonates. In: Wolf KH, Chilingarian GV, Eds. *Diagenesis IV Developments Sedimentology* 51. Elsevier Amsterdam, pp. 287-282

- Braissant O, Decho AW, Dupraz C, Glunk C, Przekop KM, Visscher PT. 2007. Exopolymeric substances of sulfate-reducing bacteria, interactions with calcium at alkaline pH and implication for formation of carbonate minerals, *Geobiology* 5, 401–411.
- Boudreau, BP, Canfield. DE. 1993 A comparison of closed- and open-system models for porewater pH and calcite-saturation. *Geochim. Cosmochim. Acta* 57:317-314.
- Buczynski C, Chafetz, HS. 1993. Habit of Bacterially Induced Precipitates of Calcium Carbonate: Examples from Laboratory Experiments and Recent Sediments. In: Rezak R, Lavoie DL., Eds., *Carbonate Microfacies*. Springer-Verlag, New York, pp. 105-116.
- Burdige DJ, Gardner KG. 1998. Molecular weight distribution of dissolved organic carbon in marine sediment pore waters. *Marine Chemistry* 62:45–64.
- Burne RV, Moore LS. 1987, Microbialites: Organosedimentary deposits of benthic microbial communities. *PALAIOS* 2, 241–254.
- Cameron EM, Hattori K. 1987. Archean sulphur cycle: Evidence from sulphate minerals and isotopically fractionated sulphides in Superior Province, Canada. In: Clauer N, Chaudhuri S. (eds.), *Isotopes in the Sedimentary Cycle*. Chem. Geol. (Isot. Geosci. Sect.) 65:341-358.
- Canfield DE. 1998. A new model for Proterozoic ocean chemistry. *Nature* 396:450-453.
- Castanier S. 1999. Ca-carbonates precipitation and limestone genesis — the microbiogeologist point of view. *Sedimentary Geology* 126: 9-23.
- Canfield DE, Habicht KS, and Thamdrup B. 2000. The Archean sulfur cycle and the early history of atmospheric oxygen. *Science* 288: 658–661.
- Chacko T, Cole DR. and Horita J. 2001. Equilibrium oxygen, hydrogen and carbon isotope fractionation factors applicable to geologic systems. *In: Valley W, Cole DJ, Eds. Stable Isotope Geochemistry*. *Rev. Mineral. Geochem.* 43, 1–81.
- Chafetz HS, Buczynski C. 1992. Bacterially induced lithification of microbial mats. *PALAIOS* 7:277–93.
- Cody RD, Cody AM. 1988. Gypsum Nucleation and Crystal Morphology in Analog Saline Terrestrial Environments. *Journal of Sedimentary Research* 58:247-255.
- Compton JS. 1988. Degree of supersaturation and precipitation of organogenic dolomite. *Geology* 16: 318-321.

- Craig H, Gordon LI, Horibe Y. 1963. Isotopic exchange effects in the evaporation of sea water. *Jour. Geoph. Res.* 68:5079-5087.
- Curti E. 1999. Coprecipitation of radionuclides with calcite: estimation of partition coefficients based on review of laboratory investigations and geochemical data. *Appl. Geochem.* 14: 433–445.
- Des Marais DJ. 2003. Biogeochemistry of hypersaline microbial mats illustrates the dynamics of modern microbial ecosystems and the early evolution of the biosphere. *Biol. Bull.* 204, 160–167.
- Decho AW. 1990. Microbial exopolymer secretions in ocean environments : their role(s) in food webs and marine processes. *Oceanography and Marine Biology: an Annual Review* 28: 73:153.
- Decho AW, Visscher PT, Reid RP. 2005. Production and cycling of natural microbial exopolymers (EPS) within a marine stromatolite. *Palaeogeog. Palaeoclim.y, Palaeoecol.* 219: 71– 86.
- Decho A.W. 2009. Overview of biopolymer-induced mineralization: What goes on in biofilms? *Ecological Engineering.* doi:10.1016/j.ecoleng.2009.01.003.
- Demicco RV, Hardie LA. 1994. Sedimentary Structures and Early Diagenetic Features of Shallow Marine Carbonate Deposits. *SEPM Atlas Series* 1, 265 pp.
- Des Marais DJ. 2003. Biogeochemistry of hypersaline microbial mats illustrates the dynamics of modern microbial ecosystems and the early evolution of the biosphere. *The Biological Bulletin.*204:160-167.
- Doğan Ö, Akyol E, Öner M. 2004. Polyelectrolytes inhibition effect on crystallization of gypsum *Cryst. Res. Technol.* 39: 1108 – 1114.
- Dravis J, Yurewicz D. 1985. Enhanced carbonate petrography using fluorescence microscopy. *Jour. Sed. Petrol.* 55:795–804.
- Dupraz C, Visscher P.T. 2005 Microbial lithification in marine stromatolites and hypersaline mats. *Trends in Microbiology* 13:429-438.
- El Tabakh M, Grey K, Pirajno F, Schreiber BC. 1999. Pseudomorphs after evaporitic minerals interbedded with 2.2 Ga stromatolites of the Yerrida basin, Western Australia: origin and significance. *Geology* 27:871–874.
- Faure G. 1991. Principles and Applications of Inorganic Geochemistry. *Mcxmillan Publishing Company*, 626 pp.
- Fazio SA, Uhlinger DJ, Parker JH, White DC. 1982. Estimations of uronic acids as quantitative measures of extracellular and cell wall polysaccharide polymers from environmental samples. *Appl. Environ. Microbiol.* 43:1151–1159.

- Feldmann M, McKenzie JA. 1998. Stromatolite-Thrombolite Associations in a Modern Environment, Lee Stocking Island, Bahamas. *PALAIOS* 13: 201-212.
- Fernández-Díaz L, Pina CM, Astilleros JM, Sánchez-Pastor N. 2009. The carbonatation of gypsum: Pathways and pseudomorph formation. *American Mineralogist* 94:1223-1234.
- Fike D. 2010. Earth's redox evolution. *Nature Geosciences* 3: 453-454.
- Flemming H C. 1995. Sorption sites in biofilms. *Wat. Sci. Technol.* 32, 27–33.
- Flemming HC and Wingender J. 2001 Relevance of microbial extracellular polymeric substances (EPS's): Part I. Structural and ecological aspects. *Water Sci. Technol.* 43:1–8.
- Folk RL. 1993. SEM imaging of bacteria and nannobacteria in carbonate sediments and rocks. *Jour. Sed. Petrol.* 63:990–999.
- Friedman I, O'Neil JR. 1977. Compilation of stable isotope fractionation factors of geochemical interest. In Fleisher M. (Ed.), *Data of Geochemistry*, 6th ed., USGS Prof. Paper 440.
- Gerdes G, Krumbein WE, Noffke N. 2000. Evaporite microbial sediments. In Riding RE, Awramik SM. (eds.) *Microbial Sediments*. Springer-Verlag, Berlin 196- 208 pp.
- Giunta G., Beccaluva L., Coltorti M., Siena F., Vaccaro C. 2002. The southern margin of the Caribbean Plate in Venezuela: tectono-magmatic setting of the ophiolitic units and kinematic evolution. *Lithos* 63: 19– 40.
- Grotzinger JP. 1989. Facies and evolution of Precambrian carbonate depositional systems: Emergence of the modern platform archetype, in Crevello, P. D., et al., eds., *Controls on carbonate platform and basin development: Society of Economic Paleontologists and Mineralogists Special Publication 44:79–106.*
- Grotzinger JP. 1994. Trends in Precambrian carbonate sediments and their implication for understanding evolution. In Bengtson S. (ed.), *Early Life on Earth*. Nobel Symposium 84: 245–258. Columbia University Press, New York.
- Grotzinger JP, Kasting JF. 1993. New constraints on Precambrian ocean composition. *The Journal of Geology* 101:235-43.
- Grotzinger JP, Rothman DR. 1996. An abiotic model for stromatolite morphogenesis. *Nature* 383: 423–425.
- Grotzinger JP, Knoll AH. 1999. Stromatolites in Precambrian carbonates, Evolutionary mileposts or environmental dipsticks? *Annual Review of Earth and Planetary Sciences* 27:313-358.

- Hardie LA. 2003. Secular variations in Precambrian seawater chemistry and the timing of Precambrian aragonite seas and calcite seas. *Geology* 31:785-788.
- Hardie LA. 2004. Secular variations in Precambrian seawater chemistry and the timing of Precambrian aragonite seas and calcite seas. Reply to Dr. Dawn Sumner Comment. *Geology* 32:e1-e2.
- Hofmann HJ. 1971. Precambrian fossils, pseudofossils, and problematica in Canada: Geological Survey of Canada Bulletin 189, 146 pp.
- Hofmann HJ, Thurston PC, Wallace H. 1985. Archean stromatolites from Uchi greenstone belt Northwestern Ontario *in* Ayres LD Thurston PC, Card KD, Weber W (eds.) *Evolution of Archean Supracrustal Sequences* Geological Association of Canada Special Paper 28:1125-1132.
- Hofmann HJ, Grey K, Hickman AH, Thorpe RI. 1999. Origin of 3.45 Ga coniform stromatolites in Warrawoona Group, Western Australia. *Geol Soc Am Bull* 111:1256–1262.
- Holland HD. 1984. *The Chemical Evolution of the Atmosphere and Oceans*: Princeton, N.J., Princeton University Press, 582 p.
- Hryniv S, Pery TM. 2010. Strontium distribution and celestite occurrence in Zechstein (Upper Permian) anhydrites of West Poland. *Chemie der Erde - Geochemistry* 70: 137-147.
- Hudec PP, Sonnenfeld P. 1974. Hot Brines on Los Roques, Venezuela. *Science* 185:440-442.
- INPARQUES 2008 [Internet]. Parque Nacional Archipiélago Los Roques, Información General, [cited 2009, Dec 11], Available from: <http://www.inparques.gob.ve/>
- Jarosewich E. 2002. Smithsonian microbeam standards. *J. Res. Natl. Inst. Stand. Technol.* 107:681–685.
- Jørgensen BB. 1994. Sulfate reduction and thiosulfate transformations in a cyanobacterial mat during a diel oxygen cycle, *FEMS Microbiol. Ecol.* 13: 303–312.
- Kah LC, Lyons TW, Chesley JT. 2001. Geochemistry of a 1.2 Ga carbonate–evaporite succession, northern Baffin and Bylot Islands: implications for Mesoproterozoic marine evolution. *Precambrian Res.* 111:203–234.
- Kah, LC, Lyons TW, Frank TD. 2004. Low marine sulphate and protracted oxygenation of the Proterozoic biosphere. *Nature* 431:834–838.

- Kamber B, Bolhar R, Webb G. 2004. Geochemistry of late Archaean stromatolites from Zimbabwe: evidence for microbial life in restricted epicontinental seas. *Precambrian Research* 132:379-399.
- Kasting JF, Ono S. 2006. Palaeoclimates: the first two billion years. *Philosophical transactions of the Royal Society of London. Series B, Biological sciences.* 361:917-929.
- Kaufman E. N., Little M.H. & Selvaraj P. T. 1996. Recycling of FGD Gypsum to Calcium Carbonate and Elemental Sulfur Using; Mixed Sulfate-Reducing Bacteria with Sewage Digest as a Carbon Source. *J. Chem. Tech. Biotechnol.* 66: 365-374
- Kennard JM, James NP. 1986. Thrombolites and Stromatolites, Two Distinct Types of Microbial Structures *PALAIOS* 1: 492-503.
- Kim ST, O'Neil JR. 1997 Equilibrium and nonequilibrium oxygen isotope effects in synthetic carbonates. *Geochim. Cosmochim. Acta* 61:3461–3475.
- Kobluk DR, Risk MJ. 1977. Calcification of exposed filaments of endolithic algae, micrite envelope formation and sediment production: *Jour. Sed. Petrol.* 47: 517- 528.
- Konhauser K. 2007. Introduction to Geomicrobiology. Blackwell Science. 425 pp.
- Last WM, Schweyen TH. 1983. Sedimentology and geochemistry of saline lakes of the Great Plains. *Hydrobiologia* 105:245-263.
- Lattman LH, Lauffenburger SK. 1974. Proposed role of gypsum in the formation of caliche *Zeitschrift für Geomorphologie, Supplementbänd* 20:140-149.
- Lee D, Carpenter SJ. 2001. Isotopic disequilibrium in marine calcareous algae. *Chemical Geology* 172, 307-329.
- Lloyd RM. 1966. Oxygen isotope enrichment in sea water by evaporation. *Geochim. Cosmochim. Acta* 30: 801-814.
- Major R, Lloyd R, Lucia F. 1992. Oxygen isotope composition of Holocene dolomite formed in a humid hypersaline setting. *Geology* 20:586-588.
- Martin A, Nisbet E, Bickle M. 1980. Archaean stromatolites of the Belingwe greenstone belt, Zimbabwe (Rhodesia). *Precambrian Research* 13:337-362.
- Mazzullo SJ. 2000. Organogenic dolomitization in peritidal to deep-sea sediments. *J. Sed. Res.* 70: 10–23.
- Nissenbaum A, Baedeker M, Kaplan I, 1972. Organic geochemistry of Dead Sea sediments. *Geochem. Cosmoquim. Acta.* 36:709-727.

- Ostos M, Sisson VB, 2005. Geochemistry and tectonic setting of igneous and metaigneous rocks of northern Venezuela. In Ave Lallemand HG, Sisson VB; Eds. Caribbean-South American plate interactions, Venezuela. Special Paper - Geological Society of America: 119-156.
- Parkhurst DL, Appelo CAJ. 1999. User's guide to PHREEQC (version 2) — a computer program for speciation, batch reaction, one-dimensional transport, and inverse geochemical calculations. Water-Resources Investigations Report 99-4259 US Geological Survey, Denver, CO.
- Peckman J, Paul J, Thiel V. 1999. Bacterially mediated formation of diagenetic aragonite and native sulphur in Zechstein carbonates (Upper Permian, Central Germany). *Sedimentary Geology* 126: 205–222.
- Perry EC, Lefticariu L. 2003. Formation and geochemistry of Precambrian chert. In Holland H, Turekian K, editors. *Treatise on Geochemistry*. vol.7, Sediments, diagenesis, and sedimentary rocks. Elsevier (ISBN: 0-08-044342-7): 369–407.
- Perry T, Klepac-Ceraj V, Zhang XV, McNamara CJ, Polz MF, Martin ST, Berke N, Mitchell R. 2005 Binding of Harvested Bacterial Exopolymers to the Surface of Calcite. *Environmental Science and Technology* 39:8770-8775.
- Pierson BK, Parenteau MN, Griffin BM, 1999. Phototrophs in high-iron concentration microbial mats: physiological ecology of phototrophs in an iron deposit in hot spring. *Appl. Environ. Microbiol.* 65:5474-5483.
- Pierre C and Rouchy JM. 1988 Carbonate replacements after sulphate evaporates in the Middle Miocene of Egypt. *Jour.of Sed. Petrol.* 58: 446–456.
- Planavsky N, Ginsburg RN. 2009 Taphonomy of modern marine bahamian microbialites. *PALAIOS* 24:5-17.
- Pope MC, Grotzinger JP. 2003. Paleoproterozoic Stark Formation, Athapuscow Basin, Northwest Canada: record of cratonic-scale salinity crisis. *Jour. Sed. Res.*73:280–295.
- Posth NR, Huelin S, Konhauser KO, Kappler A. 2010. Size, density and composition of cell–mineral aggregates formed during anoxygenic phototrophic Fe(II) oxidation: Impact on modern and ancient environments *Geochim. Cosmochim. Acta* 74:3476-3493.
- Poulton SW, Fralick PW, Canfield DE. 2010. Spatial variability in oceanic redox structure 1.8 billion years ago. *Nature Geoscience* 3:486 - 490
- Reid RP, Macintyre IG. 2000. Microboring versus recrystallization: further insight into the micritization process. *Jour. Sed. Res.* 70:24-28.

- Revsbech NP, Jørgensen BB, Blackburn TH, Cohen Y. 1983. Microelectrode studies of photosynthesis and O₂, H₂S and pH profiles of microbial mats. *Limnol. Oceanogr.* 28:1062–1074.
- Riding R. 2000. Microbial carbonates: the geological record of calcified bacterial-algal mats and biofilms. *Sedimentology* 47: 179-214.
- Rimstidt J, Balog A, Webb J. 1998. Distribution of trace elements between carbonate minerals and aqueous solutions. *Geochim. Cosmochim. Acta* 62:1851–1863.
- Schopf JW, Hayes JM, and Walter MR. 1983. Evolution of Earth's earliest ecosystems: Recent progress and unsolved problems in Schopf JW (ed.), *Earth's earliest biosphere*: Princeton, New Jersey, Princeton University Press, 361–384 pp.
- Schröder S, Bekker A, Beukes NJ, Strauss H, van Niekerk HS. 2008. Rise in seawater sulphate concentration associated with the Paleoproterozoic positive carbon isotope excursion: evidence from sulphate evaporites in the ~2.2–2.1 Gyr shallow-marine Lucknow Formation, South Africa. *Terra Nova* 20:108-117.
- Shapiro RS. 2000. A Comment on the Systematic Confusion of Thrombolites. *PALAIOS* 15:166–169.
- Simonson BM, Schubel KA, Hassler SW. 1993. Carbonate sedimentology of the early Precambrian Hamersley Group of Western Australia: *Precambrian Research* 60: 287–335.
- Sonnenfeld P. 1984. *Brines and Evaporite*. Academic Press Inc. 613 pp.
- Sonnenfeld P, Hudec PP, Turek A, Boon JA. 1977. Base-Metal Concentration in a Density Stratified Evaporite Pan. In Fischer JH., ed., *Reefs and Evaporites-Concepts and depositional models*. AAPG Studies in Geology: 181-187.
- Stal LJ. 2000. Cyanobacterial mats and stromatolites. In: B. A. Whitton and M. Potts (eds.) *The Ecology of Cyanobacteria: Their Diversity in Time and Space*. Kluwer Academic Publishers, Dordrecht., 61-120 pp.
- Stanworth CW, Badham JPN. 1984. Lower Proterozoic red beds, evaporites and secondary sedimentary uranium deposits from the East Arm, Great Slave Lake, Canada: *J. Geol Soc London* 141: 235–242
- Stefess GC, Torremans RAM, De Schrijver R, Robertson LA, Kuenen JG. 1996. Quantitative measurement of sulphur formation by steady-state and transient-

- state continuous cultures of autotrophic *Thiobacillus* species. *Appl. Microbiol. Biotechnol.* 45: 169–175
- Stomp M, Huisman J, Stal LJ, Matthijs HC. 2007. Colorful niches of phototrophic microorganisms shaped by vibrations of the water molecule. *The ISME Journal* 1:271-282.
- Sumner D, Grotzinger J. 2000. Late Archean aragonite precipitation: petrography facies associations and environmental significance. In: Altermann W, Corcoran PL, editors. *Carbonate sedimentation and diagenesis in the evolving Precambrian world: SEPM (Society for Sedimentary Geology) Special Publication 67: 123–144.*
- Sutherland IW. 2001. Exopolysaccharides in biofilms, flocs and related structures. *Water Science and Technology* 43:77-86.
- Thompson JB, Ferris FG. 1990. Cyanobacterial precipitation of gypsum, calcite, and magnesite from natural alkaline lake water. *Geology* 18: 995-998
- Trichet J, Défarge C. 1995. Non-biologically supported organo-mineralization. *Bull. Inst. Oceanogr. Monaco* 14: 203–236.
- Turner EC, James NP, Narbonne GM. 2000. Taphonomic Control on Microstructure in Early Neoproterozoic Reefal Stromatolites and Thrombolites. *PALAIOS* 15:87-111
- Urbani F. 2005. Geología de la Isla del Gran Roque, Parque Nacional Los Roques, Venezuela: Guía de Excursión. [cited 2009, Dec 14], Available from: http://www.pdvs.com/lexico/excursio/2005_granroque_urbani.pdf
- van Gemerden H. 1993. Microbial mats: a joint venture. *Marine Geology.* 113:3–25.
- van Kranendonk M, Webb G, Kamber B. 2003. Geological and trace element evidence for a marine sedimentary environment of deposition and biogenicity of 3.45 Ga stromatolitic carbonates in the Pilbara Craton, and support for a reducing Archaean ocean. *Geobiology* 1:91-108.
- Visscher PT and Stolz JF. 2005. Microbial mats as bioreactors, populations, processes, and products, *Paleogeogr. Paleoclimatol. Paleoecol.* 219: 87–100.
- Vogel, MB, Des Marais, DJ, Turk KA, Parentau MN, Jahnke LL, Kubo MDY 2009. The role of biofilms in the sedimentology of actively forming gypsum deposits at Guerrero Negro, Mexico. *Astrobiology* 9:875-893.
- Vogel M, Des Marais D, Parenteau MN, et al. 2010. Biological influences on modern sulfates: Textures and composition of gypsum deposits from Guerrero Negro, Baja California Sur, Mexico. *Sedimentary Geology.* 223:265-280.

- Walker RN, Muir MD, Diver WL, Williams N, Wilkins N. 1977. Evidence of major sulfate evaporite deposits in the Proterozoic McArthur Group, Northern Territory, Australia. *Nature* 265:526–529.
- Walter, MR. 1983. Archean stromatolites: evidence of earth's earliest benthos, in Schopf, JW; editor. *Earth's Earliest Biosphere; Its Origin and Evolution*: Princeton, N.J., Princeton University Press, 187–213 pp.
- Wang Y, Wang Y, Merino E. 1995. Dynamic weathering model: Constraints required by coupled dissolution and pseudomorphic replacement. *Geochim. Cosmochim. Acta*, 59: 1559–1570.
- Wang D, Wallace AF, De Yoreo JJ, Dove PM. 2009. Carboxylated molecules regulate magnesium content of amorphous calcium carbonates during calcification. *Proceedings of the National Academy of Sciences* 106:21511-21516.
- Wilks ME. 1986. The geology of the Steep Rock Group, N.W. Ontario: A major Archean unconformity and Archean stromatolites [M.Sc. thesis]. Saskatoon, University of Saskatchewan, Canada, 212pp
- Wright DT. 1999. The role of sulphate-reducing bacteria and cyanobacteria in dolomite formation in distal ephemeral lakes of the Coorong region, South Australia. *Sed. Geol.* 126:147–157.
- Wright DT, Wacey D. 2005. Precipitation of dolomite using sulphate-reducing bacteria from the Coorong Region, South Australia: significance and implications. *Sedimentology* 52:987–1008.

CHAPTER V

Summary and Conclusions

Microbial biomass might be ubiquitous in a variety of coastal environments from shallow marine to hypersaline sabkha flats, where it is comprised by an important fraction of carboxylated macromolecules. The ionization of their carboxyl functional groups provides an electrical charge which facilitates chemical reactions with dissolved ions, and ultimately, the sorption of metal cations. The success of some microbial communities inhabiting often hostile microscale ecosystems, as hypersaline lagoons, has been attributed to their capability to secrete and/ or modify carboxylated macromolecules, which bind bioactive metals increasing their concentration on the local microenvironment or keep away toxic metals from the immediate vicinity of the cells.

By comparing the adsorption behaviour of uronic acid heteropolymers (alginate) and glycoproteins (mucin) with the overall reactivity of microbial EPS and organic linings, respectively, this research investigate their specific role in adsorption metal in marine environments. This study hypothesize on the likely effects that such primary biogeochemical feature may have in the incorporation of Mg and bioactive trace metals into early diagenetic carbonate cements formed

during BSR. This chapter contains a summary and conclusions of the experimental and the field components of this research.

5.1 To the experimental component

The experimental aims of this research were reached by testing the metal adsorption capacity of the purified alginate, extracted from brown algae (as surrogate for uronic-rich EPS compounds) and that of the partially purified Type III Porcine Gastric Mucin (an analogue for mucin glycoproteins secreted by marine organisms). These commercially-available products were selected owing to their compositional similarities to carboxylated biomacromolecules of interest, whose specific metal adsorptive properties are still poorly understood.

Results from Chapter II demonstrate that carboxyl functional groups in alginate are significantly deprotonated at circumneutral pH; the competition of proton and cations for available sites in a given uronic-rich macromolecule is therefore responsible for its metal binding behaviour with increasing pH. The experimental data and a comprehensive literature review revealed that alginate affinity for metal has the potential to influence the residual concentration of cations in pore waters of microbial sediments.

In Chapter III, Type III PGM was shown to be composed by a mucin-type glycoprotein exhibiting striking compositional similarities with mucus secreted under experimental conditions by marine polychaete worms. Accordingly, the commercially-available mucin material has the potential for being used as experimental surrogate in studies designed to investigate the role of glycoproteins as control on the precipitation/ dissolution of biominerals, occurring in burrow walls, which particularly reactive microenvironments in marine sediments. In his regards, the Cd adsorption behaviour of PGM is comparable to that exhibited by mucus from Terebellid worms, thus the biomineralization processes occurring in burrow walls can be modelled by using PGM.

5.2 To the field component

The field component of this research was intended to extrapolate the experimental observations to conditions occurring in natural environments,

bridging the gap existing between laboratory conditions and the constraints required for amorphous carbonate to precipitate and become stable in organic-rich marine hypersaline settings. Large gypsum-dominated microbialites coated by well developed and stratified microbial mats were found growing in the shallow waters of a restricted hypersaline lagoon on the Archipelago Los Roques, Venezuela. The studied site is characterized by the following environmental/ sedimentological features:

1. The overlying hypersaline waters are characterized by temperatures in excess of 30°C, and high total alkalinity and Mg/Ca ratio.
2. In the organic mud- and gypsum-dominated basin, the environmental conditions promote bacterial growth and abundant production of EPS that serves a reactive organic matrix for precipitation of authigenic carbonates.
3. The microbialites from Laguna Pirata have a crudely laminated to clotted internal fabric and thus can be morphologically regarded as thrombolites.
4. Gypsum crystals comprise the largest part of the microbialites and are partially replaced by aragonite, to form aragonite pseudomorphs after gypsum. These crystals are cemented by microcrystalline calcium carbonate containing up to 25 mol % Mg, the carbonate cements occurred within an organic matrix, these cements also exhibited specific enrichment trends with depth.

Results from various analytical approaches, including standard and fine-scale petrography, C and O stable isotope analysis, and laser-ablation ICP-MS, suggest that the calcification of these thrombolites is an early diagenetic process, catalyzed by the breakdown of gypsum by SRB accompanied by SOB. The carbon and oxygen isotopic composition of the carbonate phases studied reflect the precipitation and the interplay of organic and inorganic carbon reservoirs. Early-diagenetic carbonate cements are closer to equilibrium with respect to inorganic carbon, while aragonite -replacing gypsum are relatively enriched in ^{12}C , most likely due to incorporation of carbon released by SRB heterotrophy of organic matter. The oxygen isotopic composition of carbonates in Laguna Pirata results from equilibrium mineral precipitation from evaporated seawater. The uniformity

of the $\delta^{18}\text{O}$ values, as compared with allochemical grains in the basin (mostly aeolian-transported *Halimeda* flakes) suggests that authigenic precipitation exceeds trapping and neomorphism within the microbial mat, and carbonate precipitation occurs mostly under hypersaline conditions. The content of Mg, and redox sensitive trace metals, of carbonate cements indicate that a mechanism of lithification is controlled by the decaying process of biofilm material trapped during accretion, so the release of metals from EPS ongoing degradation, and serving as template for the growth of amorphous carbonate phases, favour the stabilization of impure calcites (calcite containing divalent metals other than Ca).

Early attempts to distinguishing between pseudomorphs after gypsum and pseudomorphs after aragonite in the Archean to Proterozoic rock record do not considered the extent in which microbially mediated early diagenetic processes obliterated the primary gypsum textures, influencing the chemical signatures of the resulting carbonate replacement and cementing phases. In this regard, by examining the textural and chemical signatures of early diagenetic calcite pseudomorphs after gypsum it is demonstrated how the complex interplay between bacterial activity and environmental conditions promotes the early calcification of gypsum. Overall, evidence for gypsum precipitation in the Archean to Proterozoic transition is still needed to better constrain models of Precambrian ocean chemistry, in this regard Los Roques thrombolites provide us with a unique study site to better understand the likely geomicrobiological process occurred in Precambrian marine carbonates to evaporites environments that obscured their recognition in the geological record.